

Magnus Jenssen

Model Predictive Control of a Variable Speed Back-up Diesel Generator Interfaced to an AC Ship Power System as a Virtual Synchronous Machine

Master's thesis in Industrial Cybernetics

Supervisor: Jon Are Suul

June 2021

Magnus Jenssen

Model Predictive Control of a Variable Speed Back-up Diesel Generator Interfaced to an AC Ship Power System as a Virtual Synchronous Machine

Master's thesis in Industrial Cybernetics
Supervisor: Jon Are Suul
June 2021

Norwegian University of Science and Technology
Faculty of Information Technology and Electrical Engineering
Department of Engineering Cybernetics



Norwegian University of
Science and Technology

Preface

This thesis finalizes a two-year-long master's programme within Industrial Cybernetics at the Department of Engineering Cybernetics at NTNU. I started the study in the autumn of 2019 after completing a bachelors degree within electrical engineering. The last two years have been an incredible experience both personally and professionally, with a steep but highly rewarding learning curve.

The master's project documented in this thesis is a continuation of the work started in a specialization project autumn 2020, where a virtual synchronous machine model was subjected to functional verification in Simulink. This project goes one step further and is focused on a variable-speed diesel generator interfaced as a virtual synchronous machine in an AC ship power system. The Marine Power Conversion Systems specialization course, along with courses within optimized control, linear systems theory and power electronics, have provided me with much of the theoretical background and skills needed to carry out the work in this project.

I would like to express my sincere gratitude and appreciation to my supervisor Jon Are Suul. In regular discussions throughout the project he has enthusiastically shared of his knowledge and experience, and has gone out of his way in helping me to surpass technical challenges in order to move the project forward step-by-step.

Abstract

A diesel-electric ship power system may be subjected to large load variations, spanning from full propulsion load to hotel loads, or anywhere in between. The fuel efficiency in a power system without battery storage capabilities may be poor during low-load situations because the main generators are typically dimensioned for larger loads. A small variable-speed diesel generator implementation is proposed as a solution for improving fuel efficiency during low-load situations. Such a solution may take the role as an alternative in case a battery system is not available or has too low capacity for long term operation.

The work presented in this thesis is done in connection with a Simulink simulation consisting of a variable-speed diesel generator (VSDG) and a DC/DC converter interfaced to an AC ship power system as a virtual synchronous machine (VSM). The VSM can operate both islanded and connected to the main generators. The transition from grid-connected to islanded operation is seamless, like in a physical generator, without any switching between operational modes. The VSDG and DC/DC converter control system is the main topic of this thesis. A functional verification of the VSM model was performed earlier, in the specialization project. The VSM is therefore not in the centre of this work but is implemented as a separate control system to form a full AC-DC-AC converter.

During very low load situations there may be a potential for fuel savings by minimizing the generator speed in line with the load power. However, such a minimized speed operation will entail challenges during a sudden load increase due to the large diesel generator inertia. A large load increase during low speed operation would cause a significant voltage drop, or even worse, cause the diesel engine to stall. To keep the system stable during load surges at reduced generator speed, an adaptive linear model predictive controller is implemented to control the VSDG speed and excitation along with the DC/DC converter current.

A model is made for the purpose of MPC prediction and is also used to perform small-signal tuning of a conventional control system made using multiple SISO PI controllers. The model is made using well known techniques for synchronous machine and power electronics modelling.

The MPC performance is compared to that of the conventional SISO control design. Both control designs are verified in a full AC-DC-AC system simulation subjected to load changes and a transition from grid-connected to islanded operation. The MPC system is shown to handle load surges during reduced speed operation better than the SISO system, given that a momentarily output voltage reduction is allowed.

Sammendrag

Dieselelektriske marine kraftsystemer kan bli utsatt for store belastningsvariasjoner. Belastningen kan for eksempel variere mellom full fremdrifts-belastning og veldig lav hotel-belastning. Drivstoff-effektiviteten i et kraftsystem uten batteri-lagring kan være dårlig i situasjoner med lav belastning fordi hoved-generatorene vanligvis er dimensjonert for større belastninger. Implementasjon av en mindre variabel-hastighet diesel-generator foreslås som en løsning for å forbedre drivstoff-effektiviteten under situasjoner med lite belastning. En slik løsning kan være aktuell som et alternativ til et batterisystem, dersom dette ikke er tilgjengelig eller har for lav kapasitet til langvarig drift.

Arbeidet presentert i denne oppgaven er sentrert rundt en Simulink-modell bestående av en variabel-hastighet diesel-generator (VSDG) og en DC/DC-omformer, som et grensesnitt mot en nett-tilkoblet virtuell synkronmaskin (VSM). VSMen kan både driftes i tilkobling hoved-generatorene og i øy-drift. Overgangen fra nett-tilkoblet til øy-drift er sømløs, som i en fysisk generator, uten noen endringer in driftsmodus. Styresystemet for generatoren og DC/DC-omformeren er hovedtemaet i denne oppgaven. En funksjonell verifisering av VSM-modellen ble gjennomført tidligere, i spesialiseringsprosjektet. Den virtuelle synkronmaskinen er derfor ikke i sentrum av denne oppgaven, men er implementert som et separat kontrollsystem for å danne en full AC-DC-AC-omformer.

I situasjoner med svært lav belastning kan det være et potensiale for drivstoff-besparelser ved å redusere generatorhastigheten i tråd med belastningen. Drift ved redusert hastighet vil imidlertid medføre utfordringer i et tilfelle med en plutselig økning i belastning på grunn av tregheten i svingmassen til diesel-generatoren. En stor økning i belastning ved lav generatorhastighet kan medføre et betydelig spenningsfall, eller i verste fall, kvele dieselmotoren. For å holde systemet stabilt ved lastøkninger under redusert generatorhastighet, har en adaptiv lineær modellprediktiv regulator blitt implementert for å kontrollere generatorens hastighet og magnetisering samt DC-link strøm.

En modell av systemet er laget som prediksjonsmodell til MPC og blir også brukt til små-signal tuning av et konvensjonelt kontrollerdesign som er sammensatt av SISO PI-regulatorer. Modellen er laget med kjente teknikker for synkronmaskin- og kraftelektronikk -modellering.

MPCen er sammenlignet med det konvensjonelle kontrollsystemet. Begge disse kontrollsystemene er funksjonstestet i en AC-DC-AC full-system-simulasjon med sprang i belastning og omkobling fra nett-tilkoblet til øy-drift. Den adaptive MPCen er bevist å kunne håndtere økninger i belastning, ved redusert generatorhastighet, bedre enn det konvensjonelle kontrollsystemet, gitt at den nødvendige spenningsreduksjon tillates.

Contents

1	Introduction	1
1.1	Ship Power Systems	1
1.2	AC vs DC	1
1.3	Reducing Fuel Consumption	3
1.4	Virtual Synchronous Machine	4
1.5	Project Idea	5
1.6	Contributions	6
1.7	Method	6
1.8	Thesis Outline	7
2	Modelling	8
2.1	State Space Modelling	8
2.1.1	Small-Signal Modelling	9
2.1.2	State Space to Transfer Function	10
2.2	Small-Signal Stability	10
2.3	Synchronous Machine	11
2.3.1	Field and Armature Reaction	12
2.3.2	Park Transformation	13
2.3.3	Equivalent Circuits	15
2.3.4	Swing Equation	16
2.3.5	Synchronous Machine Parameters	17
2.3.6	Excitation Controller	18
2.3.7	Speed Controller and Diesel Engine	18
2.4	Per unit system	19
2.5	Rectifier	21
2.6	Boost Converter	22
2.6.1	Per unit conversion	23
2.6.2	Linearization	25
2.6.3	Linear system State Feedback	25
2.6.4	Simplified Boost Converter Model	27

CONTENTS

2.6.5	Model Matching	28
2.7	Combining system Models	29
2.8	Model Verification	34
2.9	Virtual Synchronous Machine	37
2.9.1	Current controller	38
2.9.2	Inertia Model	39
2.9.3	Phase Locked Loop	40
2.9.4	Voltage and Reactive Power Controller	41
2.9.5	Electrical Model	42
3	Control	43
3.1	Classical SISO control	43
3.1.1	Speed look-up	44
3.1.2	Eigenvalues	44
3.1.3	Frequency Response	49
3.1.4	Cascaded Control	51
3.1.5	SISO control limitation	56
3.2	Model Predictive Controller	57
3.2.1	Control Hierarchy	58
3.2.2	Prediction Horizon and Sample Time	59
3.2.3	Objective Function	59
3.2.4	Tuning	61
3.2.5	Terminal Step Weights	62
3.2.6	Integral Action	64
3.2.7	Move Blocking	66
3.2.8	Bounds	67
3.2.9	Linear Prediction	68
3.2.10	Adaptive MPC	70
3.2.11	Connecting VSM	72
4	Control Method Comparison	74
4.1	Project Model Simulation	74
4.1.1	SISO Control	75
4.1.2	Linear MPC	75
4.1.3	Adaptive MPC	76
4.2	AC-DC-AC Detailed Model Simulation	77
5	Conclusion and Further Work	87
5.1	Conclusion	87
5.2	Further Work	88
	Appendix	90

A	Appendix	90
A.1	MPC Prediction Model nonlinear form	90
A.2	Title and Abstract for Synopsis	92
A.3	Park transform	93
A.4	Synchronous Machine Parameter Conversion	93
A.5	Luenberger Observer	94
A.6	Tuning-Variable Pole-Sweeps	95
A.7	Participation Matrix	100
A.8	Model constants and parameters	101
A.9	Expanded Basic Control layer	102
	References	104

List of Figures

1.1	Conceptual sketch of a diesel-electric power system with AC distribution.	2
1.2	Conceptual sketch of a diesel-electric power system with DC distribution.	3
1.3	Diesel-electric AC power system with a battery storage system implemented as a virtual synchronous machine.	4
1.4	Diesel-electric AC power system with a variable-speed backup diesel-generator implemented through a AC-DC-AC voltage source inverter.	5
1.5	Principal sketch of the AC-DC-AC converter.	6
2.1	Salient pole machine mmf phasors. Figure is inspired by [15].	12
2.2	D-axis synchronous machine equivalent circuit.	15
2.3	Q-axis synchronous machine equivalent circuit.	15
2.4	The exciter PI controller.	18
2.5	Speed control and diesel engine model.	19
2.6	Terminal voltage and current showing displacement due to commutation.	21
2.7	Boost converter circuit diagram.	23
2.8	Block diagram of the boost converter.	25
2.9	Boost converter circuit diagram.	27
2.10	Comparison of average model and simplified model against switching model.	29
2.11	Overview over nonlinear model of the generator fed boost converter.	30
2.12	Current and voltage in phase due to diode rectifier unity power factor.	33
2.13	Detailed model vs project model. DC voltage — low-voltage (v_s) and high-voltage (v_o) side.	35
2.14	Detailed model vs project model. Field voltage.	36
2.15	Detailed model vs project model. Boost inductor current.	36
2.16	Detailed model vs project model. Generator speed.	36
2.17	An overview of the VSM control system, inspired by [19].	37
2.18	Simplified overview of inverter, VSM control system and filter inductance. Inspired by [1].	38
2.19	PLL block diagram. Inspired by [9].	40
2.20	VSM phasor diagram [9].	41

LIST OF FIGURES

2.21	Equivalent armature winding circuit. Inspired by [24].	42
3.1	The classical SISO control system hierarchy.	43
3.2	Speed reference look-up table.	44
3.3	Zoomed pole plot with $k_{i,o} = 10$	45
3.4	Time response v_o with $k_{i,o} = 10$	46
3.5	Zoomed pole plot with outer loop voltage controller integral gain $k_{i,o}$ sweep.	46
3.6	Zoomed pole plot with $k_{i,o} = 30$	47
3.7	Time response v_o with $k_{i,o} = 30$	47
3.8	Bode plot form output voltage reference v_o^* to output voltage v_o	49
3.9	Bode plot form load z_o to output voltage v_o	50
3.10	Bode plot form load v_t^* to output voltage v_o	50
3.11	Inner and outer loop closed loop frequency response for boost converter, case 1.	51
3.12	Inner and outer loop closed loop frequency response for boost converter, case 2.	52
3.13	Simulation of non-linear system inner and outer loop response to load step, case 2.	53
3.14	Simulation of non-linear system inner and outer loop response to load step, case 1.	54
3.15	Outer (closed) loop boost converter frequency response.	56
3.16	The MPC control hierarchy used in the project.	58
3.17	DC current control in a case with low control input rate penalty.	61
3.18	Indication of investigated time period.	62
3.19	Predicted state trajectory with small terminal step weights.	63
3.20	Predicted state trajectory with large terminal step weights.	63
3.21	Adaptive MPC without integral action, response to load step.	65
3.22	Adaptive MPC with integral action, response to load step.	66
3.23	Calculated optimal control input trajectory using increasing blocking intervals.	67
3.24	Adaptive linear MPC principal.	70
3.25	Plot of the filtered duty cycle d and the discretized (resampled) duty cycle D	71
4.1	SISO control response during load step.	75
4.2	Linear MPC response during load step away from operating point.	76
4.3	Adaptive MPC response during load step.	77
4.4	Simulation setup principle diagram when using MPC.	78
4.5	AC-DC-AC model simulation using SISO control system. Islanding event and 0.2pu load variation.	79

LIST OF FIGURES

4.6	AC-DC-AC model simulation using adaptive MPC. Islanding event and 0.2pu load variation.	80
4.7	AC-DC-AC model simulation using SISO control system. Islanding event and 0.28pu load variation.	82
4.8	AC-DC-AC model using SISO control system, control inputs. Islanding event and 0.28pu load variation.	83
4.9	AC-DC-AC model simulation using adaptive MPC. Islanding event and 0.28pu load variation.	84
4.10	AC-DC-AC model using adaptive MPC, control inputs. Islanding event and 0.28pu load variation.	85
4.11	MPC cost function value for the 0.2pu load increase case.	86
A.1	A Luenberger observer in a closed loop plant.	95
A.2	Zoomed pole plot with speed controller proportional gain $k_{p,\omega}$ sweep.	96
A.3	Zoomed pole plot with speed controller integral gain $k_{i,\omega}$ sweep.	96
A.4	Zoomed pole plot with excitation controller proportional gain $k_{p,ex}$ sweep.	97
A.5	Zoomed pole plot with excitation controller integral gain $k_{i,ex}$ sweep.	97
A.6	Zoomed pole plot with outer loop voltage controller proportional gain $k_{p,o}$ sweep.	98
A.7	Zoomed pole plot with outer loop voltage controller integral gain $k_{i,o}$ sweep.	98
A.8	Zoomed pole plot with inner loop current controller proportional gain $k_{p,i}$ sweep.	99
A.9	Zoomed pole plot with inner loop current controller integral gain $k_{i,i}$ sweep.	99
A.10	Control hierarchy with expanded basic control layer. Not used in the project.	103

List of Tables

2.1	Synchronous generator standard parameters	17
2.2	Synchronous generator fundamental parameters	18
2.3	Power system base values.	20
2.4	Diode bridge rectifier setup	22
3.1	Tuning Parameter Setup	48
3.2	Generator and boost converter closed loop system modes.	49
3.3	Zeros in the outer loop boost converter transfer function.	55
3.4	MPC soft bounds	68
3.5	MPC hard bounds	68
4.1	Power system rated values for VSDG, CSDG and VSM	78
4.2	Active power references used in the simulation.	78
A.1	Standard Parameter Expressions from [13].	93
A.2	Tuning Parameter Setup	96
A.3	Generator and boost converter closed loop system modes.	100
A.4	Model constants	101
A.5	Synchronous generator fundamental parameters	101
A.6	Diode bridge rectifier setup	101
A.8	VSM filter constants	101
A.7	VSM control system parameters	102
A.9	Simulation settings	102

Chapter 1

Introduction

1.1 Ship Power Systems

The field of marine power systems is subject to a high degree of diversity. Design philosophies often change from one vessel to the next in order to meet a specific set of needs. Going back in history, a typical vessel propulsion system would involve a direct mechanical coupling from the prime movers to the propellers. Such a direct mechanical drive places a strict limitation on a vessels design when considering the placement of mechanical equipment, whereas electric power transfer allows for more flexibility in the design. The first generation of electrically powered ships dates back to the 1920s. The propulsion systems was such that the propeller speed was directly dependent on the generator speed [11]. The astounding technological development during the 20th century lead up to the development of power electronics during the 70's and 80's [11], which enabled variable-speed drive of AC motors. A fully controllable propulsion engine speed allows for the prime movers to be operated at a constant speed, optimized for fuel efficiency. Over the following decades, from the 80's to the beginning of the 21st century, diesel-electric propulsion gained popularity in the commercial market. For example passenger and cruise vessels, but also platform supply vessels and other offshore industry vessels, converted to diesel-electric [23].

1.2 AC vs DC

Up until today, AC distribution has been the main solution for diesel-electric marine power systems. Figure 1.1 shows the basic principle of a diesel-electric AC power system.

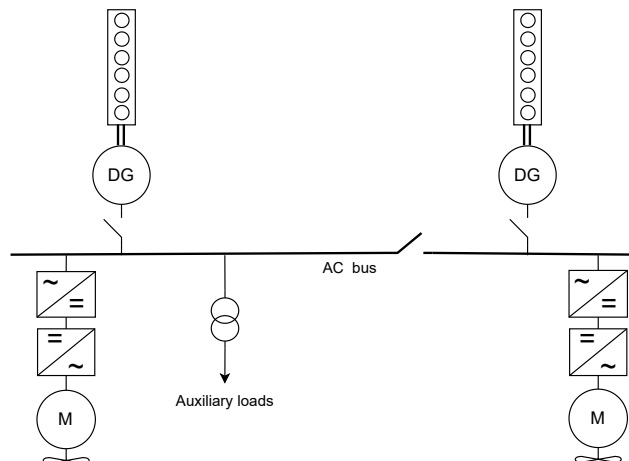


Figure 1.1: Conceptual sketch of a diesel-electric power system with AC distribution.

In an AC distribution system, the main generators are connected directly to the AC bus. Before a generator goes online, the diesel engine speed is controlled to synchronize the generator frequency to the grid¹. There are multiple reasons for choosing a system with AC distribution instead of DC. The AC distribution technology is more mature and is often regarded as the safest design. The currents in an AC power system always has the benefit of zero crossings, making for simpler design of power switches and electrical protection equipment. Furthermore, reliable AC power production for auxiliary loads is an important design requirement for most vessels. In an AC system, auxiliary loads can simply be powered from the main busbar. AC systems have for these reasons dominated the market.

DC distribution imposes higher design requirements on electrical protection equipment due to the risk of arcing and overheating, which contributes to an increased system costs. However, the push towards low emission solutions, such as battery storage and fuel cell systems, has intensified research and delivery of DC distribution over the last decade. Figure 1.2 shows the basic principle of a DC distribution system.

¹A phase locked loop (PLL) is commonly used to measure the grid frequency.

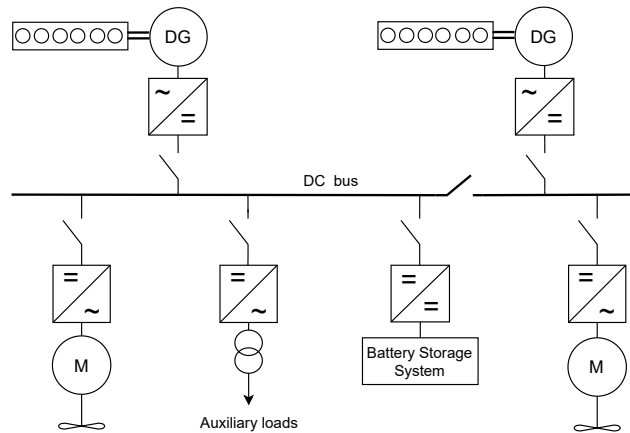


Figure 1.2: Conceptual sketch of a diesel-electric power system with DC distribution.

Comparing figures 1.2, 1.1 one can see that the number of conversion stages between generators and propulsion is actually the same in both AC and DC systems. The rectification step in DC systems is simply relocated from propulsion to generators. An obvious advantage of the DC distribution is that speed synchronization of the main generators is avoided. Fuel optimization through variable-speed is therefore a possibility.

1.3 Reducing Fuel Consumption

In general, electric power systems needs an instantly available energy reserve to account for load disturbances and sudden load surges. This fast-acting reserve exists inherently in the generator spinning inertia. However, if speed is to be limited, so is the energy reserve. Battery storage, being a relatively fast acting energy reserve, can work in companion with the main generators to decrease voltage drop during load surges. It is sensible to assume that a reduction of the spinning reserve can be achieved using such a method, and that fuel efficiency can be improved through a limited speed operation. Another solution based on using super-capacitors as the fast-acting reserve is investigated in [14] and [7]. The instant access to energy in a super-capacitor can suppress very fast load disturbances.

Any type of diesel-electric vessel must cope with a variety of operating conditions. The load situation can vary from full propulsion load, to mechanical equipment operating on deck, to hotel loads such as lightening and electronic equipment on the bridge and in the cabin. Therefore, the span from minimal to maximal load is large. Avoiding operation of the main generators in low-load situations can drastically decrease overall fuel consumption. Battery storage can be implemented for this

purpose also in AC systems. A DC/AC voltage source inverter with grid forming capabilities is in that case needed if the battery system is to operate as an islanded power source. In [12] a virtual synchronous machine is shown to be a suitable option for battery storage system implementation in an AC power grid, like shown in figure 1.3.

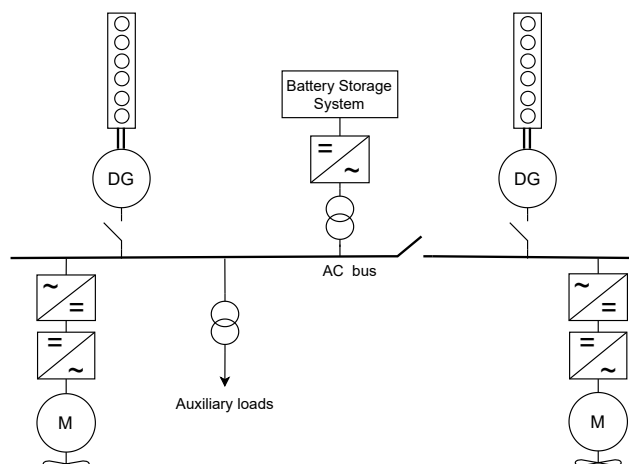


Figure 1.3: Diesel-electric AC power system with a battery storage system implemented as a virtual synchronous machine.

1.4 Virtual Synchronous Machine

The VSM-type control of AC voltage source inverters has gained popularity after it was first introduced by (Beck and Hesse, [5]) in 2007. The concept is to control an AC inverter such that it resembles the behavior of a synchronous machine. In a VSM control system, a synchronous machine emulation is running in real time — taking circuit measurements as inputs and providing emulated quantities, to be imposed on the power electronics, as outputs. For example, in a current controlled VSM case, the reference for an inner loop current controller is provided by the machine emulation. Such a topology will be shown in section 2.9.

Much of the popularity of the VSM comes from the fact that it can be thought of as a physical generator when implemented in a power system. The speed governor and exciter, used in a physical generator system, can be resembled by the outer control loops in a VSM. A VSM is considered to be a highly flexible component as it can both be synchronized to a grid frequency, but also operate as an islanded power generation unit fully controlling the grid frequency and voltage, using local references.

1.5 Project Idea

In vessels without a battery system, or in case it is not operational, fuel spending may be reduced through variable-speed operation of a smaller diesel generator or one of the main generators. Such a solution is especially relevant when a vessel is anchored, docked, or in any other situations where a vessel uses an insignificant amount of energy for propulsion for a long period of time while not being connected to an onshore power supply. This situation is the main motivation for the work presented in this thesis. In fact, the work is based on the idea of implementing a variable-speed diesel-generator (VSDG) in an AC power system as a VSM, like it is shown in figure 1.4.

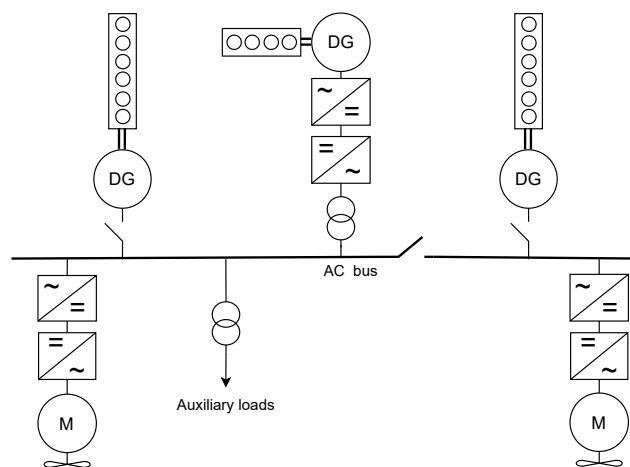


Figure 1.4: Diesel-electric AC power system with a variable-speed backup diesel-generator implemented through a AC-DC-AC voltage source inverter.

A Simulink model VSM was tested in the specialization project, and it was demonstrated to have both islanded and grid connected capabilities. Section 2.9 in this thesis is based on work done in the specialization project. Meanwhile, the rest of the work presented in this thesis is mostly dedicated to a control system for a VSDG with a diode rectifier and a boost converter as an interface to the grid-side VSM. Together, these components forms a full AC-DC-AC converter system, like shown in figure 1.5.

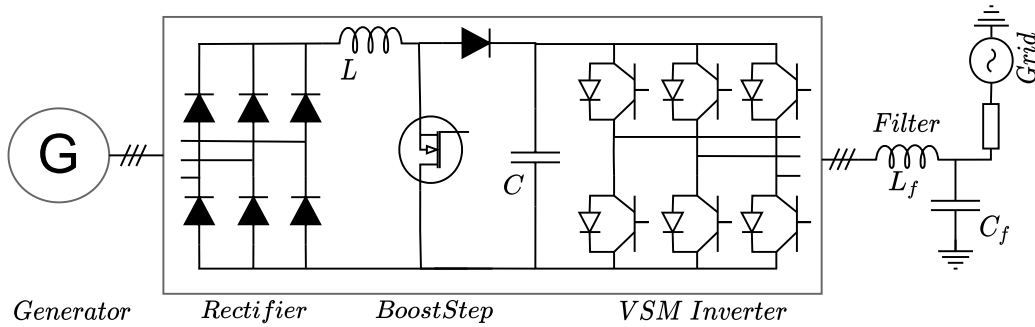


Figure 1.5: Principal sketch of the AC-DC-AC converter.

1.6 Contributions

A classical diesel-generator system usually controls fuel injection and excitation separately, using single-input-single-output (SISO) type controllers. The SISO control approach makes sense when speed is to be held at a constant level and a spinning reserve is present in case of load surges. Such a classical control system has also been implemented in this project for initial testing and comparison. Even though the SISO control approach is functional in many cases, it is not able to ensure a stable speed trajectory if a large load surge occurs during low speed operation — because the control loops are acting as separate systems. An adaptive linear model predictive control (MPC) approach is therefore implemented in chapter 3. A simplified system model, presented in chapter 2, is used as the MPC prediction model. The linear MPC is implemented in companion with an adaptive method so that the linearization-point is updated every controller time step. By using this method, the MPC is able to operate over the full range of the non-linear system.

Both control approaches are, in chapter 4, connected to the VSM model to form a full AC-DC-AC converter simulation for verification and comparison. The system is demonstrated to handle load disturbances during grid synchronized and islanded operation.

1.7 Method

Throughout the project, numerous simulation models with varying level of detail has been made. The work has mostly been done in a top-down fashion. Simulink library models with a high level of detail has been used as a reference for less detailed models. To simplify troubleshooting, model components were first tested individually before they were interconnected to form larger models.

While the main goal was to optimize fuel efficiency, this project has in practice

focused on minimizing generator speed. A system able to cope with low speed operation could potentially also be used for fuel optimization. In order to optimize for fuel consumption specifically, a more detailed model of the diesel engine may be needed, and thus increasing the complexity of the project. Such a detailed engine model was for contextual reasons not prioritized.

Initially, the work was focused on a Simulink model consisting of a synchronous machine feeding an uncontrolled diode bridge rectifier. This model was successfully connected to the Simulink VSM model. Later, a boost converter was included in the DC-link. A boost converter adds to the flexibility in voltage regulation, and avoids the need for overexcitation of the generator.

The modelling is also made simpler when including a DC/DC converter. By fully controlling the DC current, one degree of freedom is removed from the system, and thus simplifying the connection between the DC-link and the synchronous machine model.

Moving on now to consider the work within MPC implementation. The first optimal control experiments included a single horizon optimization. The quadratic optimization problem was built using custom scripts and solved using the Matlab optimization algorithm "quadprog". It was later realized that implementing the MPC using this custom method would be somewhat cumbersome, and the Matlab MPC toolbox was used instead as a safer way forward. A linear MPC, running on a linear model, was then implemented as a starting point for functional verification. Further, the linear MPC was tested for its ability to control the simplified non-linear model. The linear MPC was only functional in a small area around the linearization point and was therefore augmented with the adaptive functionality.

1.8 Thesis Outline

The introduction given in the above chapter has until now presented some background on ship power systems and explained the motivation and the idea behind the project. The second chapter will first provide some general theory used in the modelling, before presenting all models included in this work part-by-part. Chapter three deals with the control aspect by first presenting the conventional control system and then the MPC implementation. Chapter four presents the simulation results using various setups and models. The thesis is finalized in chapter five, where some closing remarks and thoughts around future work is given.

Chapter 2

Modelling

This chapter deals with the modelling of all system components. Starting of with general state space modelling theory, then moving on to consider the synchronous machine modelling, rectifier and boost converter. A combined model of these three components will be made and verified against a Simulink library model. Lastly, the virtual synchronous machine model, also described in the specialisation project, is presented.

2.1 State Space Modelling

The state vector \mathbf{x} in a state space model fully describes the state of the system. The state space is the space spanned by the state vector [4]. Thus, the state space includes all possible states the system can have. The standard time invariant state space model (2.1) is described by two functions. The system function $\mathbf{f}(\mathbf{x},\mathbf{u})$ describing the system itself, and the output function (or measurement function) $\mathbf{h}(\mathbf{x},\mathbf{u})$ which has the sole purpose of providing the output vector \mathbf{y} related to the state vector \mathbf{x} and input vector \mathbf{u} .

$$\frac{d\mathbf{x}}{dt} = \mathbf{f}(\mathbf{x},\mathbf{u}) \quad (2.1a)$$

$$\mathbf{y} = \mathbf{h}(\mathbf{x},\mathbf{u}) \quad (2.1b)$$

A linear time invariant state space system is on the form (2.2). With the system matrix \mathbf{A} , input matrix \mathbf{B} , output matrix from states \mathbf{C} and output matrix from inputs \mathbf{D} .

$$\frac{d\mathbf{x}}{dt} = \mathbf{Ax} + \mathbf{Bu} \quad (2.2a)$$

$$\mathbf{y} = \mathbf{Cx} + \mathbf{Du} \quad (2.2b)$$

Any non-zero elements in the \mathbf{D} matrix causes the system inputs \mathbf{u} to directly affect the system outputs \mathbf{y} , i.e. "direct feedthrough". Such a system cannot be strictly proper, as an (infinitely) high frequency component at the input would propagate through to the output.

2.1.1 Small-Signal Modelling

In many cases, the physical system is nonlinear. However, in a small range around a steady state point of operation, the system can be approximated by a linear system using the first order Taylor series expansion of the nonlinear system. This is known as small-signal modelling. Having the system on a linear form allows for simpler analysis to be used.

First an operating point must be established. The input vector is chosen based on known information about the operating point. Since the operating point per definition is an equilibrium, the state vector is found by solving the system function $\mathbf{f}(\mathbf{x}, \mathbf{u})$ with the derivative states set to zero.

The operating point $\bar{\mathbf{x}}$, $\bar{\mathbf{u}}$ and the small perturbation away from the operating point $\Delta\mathbf{x}$, $\Delta\mathbf{u}$ is defined as (2.3) .

$$\mathbf{x} = \bar{\mathbf{x}} + \Delta\mathbf{x} \quad (2.3a)$$

$$\mathbf{u} = \bar{\mathbf{u}} + \Delta\mathbf{u} \quad (2.3b)$$

The first order Taylor series expansion (2.4),

$$\frac{d\bar{\mathbf{x}}}{dt} + \frac{d\Delta\mathbf{x}}{dt} \approx \mathbf{f}(\bar{\mathbf{x}}, \bar{\mathbf{u}}) + \frac{\partial\mathbf{f}(\bar{\mathbf{x}}, \bar{\mathbf{u}})}{\partial\mathbf{x}}\Delta\mathbf{x} + \frac{\partial\mathbf{f}(\bar{\mathbf{x}}, \bar{\mathbf{u}})}{\partial\mathbf{u}}\Delta\mathbf{u} \quad (2.4)$$

simplifies to (2.5).

$$\frac{d\Delta\mathbf{x}}{dt} \approx \frac{\partial\mathbf{f}(\bar{\mathbf{x}}, \bar{\mathbf{u}})}{\partial\mathbf{x}}\Delta\mathbf{x} + \frac{\partial\mathbf{f}(\bar{\mathbf{x}}, \bar{\mathbf{u}})}{\partial\mathbf{u}}\Delta\mathbf{u} \quad (2.5)$$

The output function can be treated similarly (2.6).

$$\Delta\mathbf{y} \approx \frac{\partial\mathbf{h}(\bar{\mathbf{x}}, \bar{\mathbf{u}})}{\partial\mathbf{x}}\Delta\mathbf{x} + \frac{\partial\mathbf{h}(\bar{\mathbf{x}}, \bar{\mathbf{u}})}{\partial\mathbf{u}}\Delta\mathbf{u} \quad (2.6)$$

In summary, the \mathbf{A} , \mathbf{B} , \mathbf{C} and \mathbf{D} matrices describing the linearized small signal system are found by taking the jacobian matrices of the nonlinear system like shown in (2.7), (2.8), (2.9) and (2.10).

$$\mathbf{A} = \frac{\partial\mathbf{f}(\bar{\mathbf{x}}, \bar{\mathbf{u}})}{\partial\mathbf{x}} = \left(\begin{array}{cccc} \frac{\partial f_1}{\partial x_1} & \frac{\partial f_1}{\partial x_2} & \dots & \frac{\partial f_1}{\partial x_n} \\ \frac{\partial f_2}{\partial x_1} & \frac{\partial f_2}{\partial x_2} & \dots & \frac{\partial f_2}{\partial x_n} \\ \vdots & \vdots & \ddots & \vdots \\ \frac{\partial f_n}{\partial x_1} & \frac{\partial f_n}{\partial x_2} & \dots & \frac{\partial f_n}{\partial x_n} \end{array} \right)_{\mathbf{x}=\bar{\mathbf{x}}, \mathbf{u}=\bar{\mathbf{u}}} \quad (2.7)$$

$$\mathbf{B} = \frac{\partial \mathbf{f}(\bar{\mathbf{x}}, \bar{\mathbf{u}})}{\partial \mathbf{u}} = \begin{pmatrix} \frac{\partial f_1}{\partial u_1} & \frac{\partial f_1}{\partial u_2} & \cdots & \frac{\partial f_1}{\partial u_n} \\ \frac{\partial f_2}{\partial u_1} & \frac{\partial f_2}{\partial u_2} & \cdots & \frac{\partial f_2}{\partial u_n} \\ \vdots & \vdots & \ddots & \vdots \\ \frac{\partial f_n}{\partial u_1} & \frac{\partial f_n}{\partial u_2} & \cdots & \frac{\partial f_n}{\partial u_n} \end{pmatrix}_{\mathbf{x}=\bar{\mathbf{x}}, \mathbf{u}=\bar{\mathbf{u}}} \quad (2.8)$$

$$\mathbf{C} = \frac{\partial \mathbf{h}(\bar{\mathbf{x}}, \bar{\mathbf{u}})}{\partial \mathbf{x}} = \begin{pmatrix} \frac{\partial h_1}{\partial x_1} & \frac{\partial h_1}{\partial x_2} & \cdots & \frac{\partial h_1}{\partial x_n} \\ \frac{\partial h_2}{\partial x_1} & \frac{\partial h_2}{\partial x_2} & \cdots & \frac{\partial h_2}{\partial x_n} \\ \vdots & \vdots & \ddots & \vdots \\ \frac{\partial h_n}{\partial x_1} & \frac{\partial h_n}{\partial x_2} & \cdots & \frac{\partial h_n}{\partial x_n} \end{pmatrix}_{\mathbf{x}=\bar{\mathbf{x}}, \mathbf{u}=\bar{\mathbf{u}}} \quad (2.9)$$

$$\mathbf{D} = \frac{\partial \mathbf{h}(\bar{\mathbf{x}}, \bar{\mathbf{u}})}{\partial \mathbf{u}} = \begin{pmatrix} \frac{\partial h_1}{\partial u_1} & \frac{\partial h_1}{\partial u_2} & \cdots & \frac{\partial h_1}{\partial u_n} \\ \frac{\partial h_2}{\partial u_1} & \frac{\partial h_2}{\partial u_2} & \cdots & \frac{\partial h_2}{\partial u_n} \\ \vdots & \vdots & \ddots & \vdots \\ \frac{\partial h_n}{\partial u_1} & \frac{\partial h_n}{\partial u_2} & \cdots & \frac{\partial h_n}{\partial u_n} \end{pmatrix}_{\mathbf{x}=\bar{\mathbf{x}}, \mathbf{u}=\bar{\mathbf{u}}} \quad (2.10)$$

2.1.2 State Space to Transfer Function

A linearized state space system can be converted into transfer function form using 2.11.

$$\mathbf{G}(s) = \mathbf{C}(s\mathbf{I} - \mathbf{A})^{-1}\mathbf{B} + \mathbf{D} \quad (2.11)$$

The resulting transfer matrix $\mathbf{G}(s)$ contains the transfer functions for every input to every output.

2.2 Small-Signal Stability

Having the system on a linear state space form allows for the use of small signal stability analysis. The common tools for linear stability studies evolves around the definition of eigenvectors and their corresponding eigenvalues¹. The right \mathbf{v}_i and left \mathbf{u}_i eigenvectors are defined as (2.12a) and (2.12b), respectively.

$$\mathbf{A}\mathbf{v}_i = \lambda_i \mathbf{v}_i \quad (2.12a)$$

$$\mathbf{u}_i \mathbf{A} = \lambda_i \mathbf{u}_i \quad (2.12b)$$

The vector of n eigenvalues λ for a $n \times n$ system \mathbf{A} is found by solving equation 2.13.

$$\det(\mathbf{A} - \lambda \mathbf{I}) = 0 \quad (2.13)$$

¹The theory provided in this section can be found in chapter 12 in [13]

The right and left eigen matrices consists of all right and left eigenvectors (2.14).

$$\mathbf{V} = [\mathbf{v}_1 \quad \mathbf{v}_2 \quad \cdots \quad \mathbf{v}_n] \quad (2.14a)$$

$$\mathbf{U} = \mathbf{V}^{-1} \quad (2.14b)$$

In models attained through physics-based modelling, the state derivatives are often functions of multiple states. For analytical purposes, it makes sense to restate the model such that fewer states participate in each state derivative [13]. The model (2.2) can in some cases be diagonalized using equation (2.15).

$$\mathbf{\Lambda} = \mathbf{V}^{-1}\mathbf{A}\mathbf{V} \quad (2.15a)$$

$$\mathbf{x} = \mathbf{V}\mathbf{z} \quad (2.15b)$$

$$\dot{\mathbf{z}} = \mathbf{\Lambda}\mathbf{z} \quad (2.15c)$$

Here, $\mathbf{\Lambda}$ is assumed to be a diagonal matrix with the systems eigen values along its diagonal. Since the equations in the diagonalized system are decoupled, the solution in time domain is simply (2.16).

$$z(t) = \sum_{i=1}^n z_i(0)e^{\lambda_i t} \quad (2.16)$$

In case the system matrix \mathbf{A} is not diagonalizable, the system can be rewritten to Jordan canonical form. On Jordan form, the system matrix is triangular with the eigen values on the diagonal and ones or zeros above the diagonal.

Having now considered some of the methods used in general when dealing with state space modelling, the rest of this chapter concerns more specific system modelling.

2.3 Synchronous Machine

A synchronous machine is the most commonly used electric power generator. As the name implies, the rotor rotates synchronously with the magnetic field applied to the stator. The rotor is magnetized through a separate power supply, which is used to control the machines terminal voltage, i.e exciter. The generator speed is typically controlled by a speed controller or governor acting on the machinery driving the generator. In this case, the speed controller acts on the fuel injection to the diesel engine.

The first part of this section 2.3 is concerned with the modelling of the synchronous machine itself, meaning the electrical model and the swing equation. The parameterization of the electrical model is thereafter considered, before a short discussion on the typical control methods will be given in the end.

The electrical model presented here is based on equivalent winding representation in a rotating reference frame, where the model order increases with the number of windings. A fifth order model, consisting of equivalent windings for armature, field and damping, is presented in this section. The modelling and theory provided here is based on chapter 3 and 11 in [15] and chapter 3 in [13].

2.3.1 Field and Armature Reaction

A DC voltage is applied to the rotor field winding. The resulting DC current produces the field magnetomotive force (mmf) rotating synchronously with the rotor. The field mmf \vec{F}_f drives the excitation flux through the magnetic path of the airgap and stator. The rotor position, as well as the magnetic reluctance of the path, determines the time varying flux linkage between the field winding and each of the armature windings. In a salient pole machine the reluctance varies sinusoidally (in stationary reference frame) as the rotor rotates, because the air-gap varies around the rotor.

An armature reaction mmf \vec{F}_a , produced by the currents in the armature windings, also rotates with synchronous speed but is shifted in phase relative to the field mmf. The armature mmf acts against the field mmf, to demagnetize the machine. The two mmfs in combination drives the resultant airgap flux seen by the windings [15]. Figure 2.1 shows the armature reaction mmf \vec{F}_a , the field mmf \vec{F}_f and the resultant mmf \vec{F}_r in a salient pole machine with two poles.

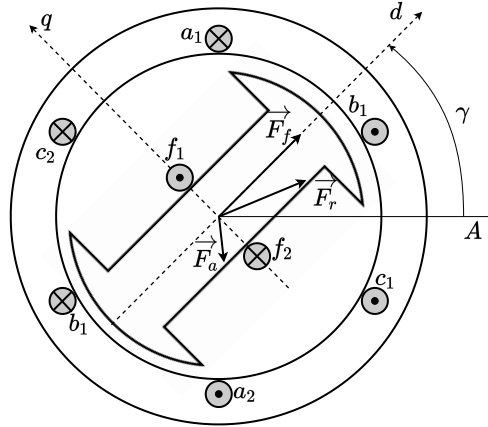


Figure 2.1: Salient pole machine mmf phasors. Figure is inspired by [15].

γ is the synchronous machine d-axis rotor position referred to phase winding axis A.

Damper windings

The purpose of the damper windings is to dampen rotor oscillations. Because the airgap flux rotates with synchronous speed, any asynchronous speed of the rotor causes the airgap flux to induce a current in the damper windings. As a result, a torque acting against any deviation from synchronous speed is produced [15].

Mixed Frame of Reference

The expression for flux linkages are given as (2.17) where the armature windings are in the stator frame of reference and the rotor windings are in the rotor reference frame. The stator self and mutual inductances \mathbf{L}_S and the mutual inductances between rotor and stator \mathbf{L}_{SR} , \mathbf{L}_{SR}^T all varies with the rotor position, as opposed to the mutual inductances between the rotor windings \mathbf{L}_R , which are constants. The synchronous machine model equations in the stator reference frame becomes somewhat complicated. The detailed expressions are left out for the sake of brevity.

$$\begin{bmatrix} \Psi_{ABC} \\ \Psi_{fDQ} \end{bmatrix} = \begin{bmatrix} \mathbf{L}_S & \mathbf{L}_{SR} \\ \mathbf{L}_{SR}^T & \mathbf{L}_R \end{bmatrix} \begin{bmatrix} \mathbf{i}_{ABC} \\ \mathbf{i}_{fDQ} \end{bmatrix} \quad (2.17)$$

In the mixed reference frame, the voltage equations are (2.18),

$$\begin{bmatrix} \mathbf{v}_{ABC} \\ \mathbf{v}_{fDQ} \end{bmatrix} = \begin{bmatrix} \mathbf{R}_{ABC} & \mathbf{0} \\ \mathbf{0} & \mathbf{R}_{fDQ} \end{bmatrix} \begin{bmatrix} \mathbf{i}_{ABC} \\ \mathbf{i}_{fDQ} \end{bmatrix} - \frac{d}{dt} \begin{bmatrix} \Psi_{ABC} \\ \Psi_{fDQ} \end{bmatrix} \quad (2.18)$$

where \mathbf{R}_{ABC} and \mathbf{R}_{fDQ} are diagonal matrices consisting of the stator and rotor winding resistances.

2.3.2 Park Transformation

The total armature reaction mmf produced by the combined currents in all armature windings is, when in steady state, a vector constant in amplitude and rotating with the same speed as the rotor [15]. Therefore, it makes sense to express the armature currents in a frame of reference rotating synchronously with the rotor. The reference frame transformation, of armature current, from stator to rotor is performed using the well known park transformation (2.19),

$$\mathbf{x}_{0dq} = \mathbf{T}\mathbf{x}_{ABC} \quad (2.19a)$$

$$\mathbf{x}_{ABC} = \mathbf{T}^{-1}\mathbf{x}_{0dq} \quad (2.19b)$$

where \mathbf{T} is the park transformation matrix given as (2.20).

$$\mathbf{T} = k_{dq} \begin{bmatrix} k_0 & k_0 & k_0 \\ \cos(\gamma) & \cos\left(\gamma - \frac{2}{3}\pi\right) & \cos\left(\gamma + \frac{2}{3}\pi\right) \\ \cos(\gamma) & \cos\left(\gamma - \frac{2}{3}\pi\right) & \cos\left(\gamma + \frac{2}{3}\pi\right) \end{bmatrix} \quad (2.20)$$

The choice of transformation matrix coefficients is actually a topic commonly discussed in literature [15][13][21]. Using $k_0 = 1/\sqrt{2}$ and $k_{dq} = \sqrt{2/3}$ (like in [15]) makes the transformation matrix (2.20) orthogonal and the park transformation becomes power invariant in SI notation. However, it also results in different number of turns between the actual ABC and the equivalent DQ armature windings. Consequently, an inconvenient scaling factor is needed in the mutual inductance between rotor and stator d and q axis windings. Another option is shown in [13], where the constants are chosen such that the maximum value of the DQ-frame current equals the peak armature current before transformation, yielding $k_0 = 1/2$ and $k_{dq} = 2/3$. This results in a non-orthogonal matrix T but avoids the stator-rotor mutual inductance scaling factor. Furthermore, the argument of power invariance is actually not very important since the per-unit expression for power is the same with either set of transformation factors.

Rotor oriented Reference Frame

The flux linkage equation and voltage equation in DQ-frame takes the form of (2.21) and (2.23) respectively.

$$\begin{bmatrix} \Psi_{0dq} \\ \Psi_{fDQ} \end{bmatrix} = \begin{bmatrix} \mathbf{T} & \mathbf{0} \\ \mathbf{0} & \mathbf{1} \end{bmatrix} \begin{bmatrix} \mathbf{L}_S & \mathbf{L}_{SR} \\ \mathbf{L}_{SR}^T & \mathbf{L}_R \end{bmatrix} \begin{bmatrix} \mathbf{T}^{-1} & \mathbf{0} \\ \mathbf{0} & \mathbf{1} \end{bmatrix} \begin{bmatrix} \mathbf{i}_{0dq} \\ \mathbf{i}_{fDQ} \end{bmatrix} \quad (2.21)$$

With the assumption that all stator winding resistances are equal, (2.22) holds.

$$\mathbf{T}\mathbf{R}_{ABC}\mathbf{T}^{-1} = \mathbf{R}_{ABC} \quad (2.22)$$

In the process of park transforming the flux linkage derivative in equation (2.18), the time derivative of the (rotor angle dependent) transformation matrix is introduced through the product rule. Consequently, the rightmost expression in (2.23) includes the synchronous machine frequency, which forms the coupling to the swing equation (2.27).

$$\begin{bmatrix} \mathbf{v}_{0dq} \\ \mathbf{v}_{fDQ} \end{bmatrix} = \begin{bmatrix} \mathbf{R}_{ABC} & 0 \\ 0 & \mathbf{R}_{fDQ} \end{bmatrix} \begin{bmatrix} \mathbf{i}_{0dq} \\ \mathbf{i}_{fDQ} \end{bmatrix} - \begin{bmatrix} \dot{\Psi}_{0dq} \\ \dot{\Psi}_{fDQ} \end{bmatrix} + \begin{bmatrix} \dot{\mathbf{T}}\mathbf{T}^{-1} & \mathbf{0} \\ \mathbf{0} & \mathbf{0} \end{bmatrix} \begin{bmatrix} \Psi_{0dq} \\ \Psi_{fDQ} \end{bmatrix} \quad (2.23)$$

In the rotor oriented reference frame, the self and mutual inductances between stator and rotor becomes constant and time invariant. Furthermore, there is no mutual inductance between the direct and quadrature axes due to the 90-degree angle between them. These two properties of the park transformation enables the direct and quadrature axes electrical dynamics to be represented by separate equivalent circuits as shown in figures 2.2 and 2.3 [13].

2.3.3 Equivalent Circuits

Five windings are represented in the rotor reference frame equivalent circuit model. Namely, the direct and quadrature axis stator windings (subscript d and q), the rotor field winding (subscript f) and the d and q axis damper windings (subscript D and Q). The stator current direction is defined to be flowing out of the machine in accordance with the generator convention.

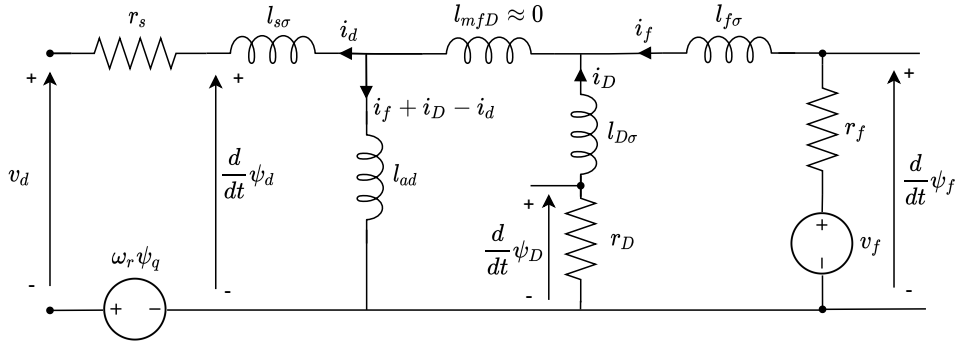


Figure 2.2: D-axis synchronous machine equivalent circuit.

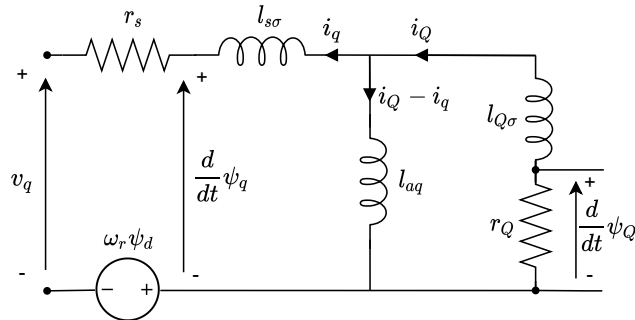


Figure 2.3: Q-axis synchronous machine equivalent circuit.

From the armature voltage equations (2.24) and the flux linkage equations (2.25, 2.25), explicit dynamic expressions for the synchronous machine currents can be

derived, with the voltages as inputs to the system.

$$v_d = -r_a i_d + \frac{1}{\omega_b} \frac{d\psi_d}{dt} - \omega_r \psi_q \quad (2.24a)$$

$$v_q = -r_a i_q + \frac{1}{\omega_b} \frac{d\psi_q}{dt} + \omega_r \psi_d \quad (2.24b)$$

$$v_f = r_f i_f + \frac{1}{\omega_b} \frac{d\psi_f}{dt} \quad (2.24c)$$

$$0 = r_D i_D + \frac{1}{\omega_b} \frac{d\psi_D}{dt} \quad (2.24d)$$

$$0 = r_Q i_Q + \frac{1}{\omega_b} \frac{d\psi_Q}{dt} \quad (2.24e)$$

Flux Linkage Equations

$$\psi_d = -x_d i_d + x_{ad} i_f + x_{ad} i_D \quad (2.25a)$$

$$\psi_q = -x_q i_q + x_{ad} i_Q \quad (2.25b)$$

$$\psi_f = -x_{ad} i_d + x_f i_f + (x_{ad} + x_{mfD}) i_D \quad (2.25c)$$

$$\psi_D = -x_{ad} i_d + (x_{ad} + i_{mfD}) i_f + x_D i_D \quad (2.25d)$$

$$\psi_Q = -x_{ad} i_q + x_Q i_Q \quad (2.25e)$$

$$x_d = x_{\sigma s} + x_{ad} \quad (2.26a)$$

$$x_q = x_{\sigma s} + x_{aq} \quad (2.26b)$$

$$x_f = x_{\sigma f} + x_{mfD} + x_{ad} \quad (2.26c)$$

$$x_D = x_{\sigma D} + x_{mfD} + x_{ad} \quad (2.26d)$$

$$x_Q = x_{\sigma Q} + x_{aq} \quad (2.26e)$$

2.3.4 Swing Equation

The synchronous machine speed is modelled using the swing equation with torque or power input.

$$\frac{d\omega}{dt} = \frac{p_m - p_e}{2H} - D\omega \quad (2.27)$$

The constant H describes the amount of kinetic energy in the rotor when it is rotating at synchronous speed. It can conveniently be defined in relation to the mechanical time constant $2H = T_a$ in a practical sense. T_a is the time it would take to accelerate the rotor from standstill to synchronous speed if the rated mechanical torque $\tau_b = S_b/\omega_b$ was applied [15]. The damping coefficient D represents the mechanical friction. The mechanical power applied to the shaft and the electrical power, also called the airgap power, is defined in per unit as (2.28).

$$p_m = \tau_m \omega \quad (2.28a)$$

$$p_e = v_d \cdot i_d + v_q \cdot i_q \quad (2.28b)$$

2.3.5 Synchronous Machine Parameters

The fundamental parameters found in the d-and q-axis equivalent circuits are convenient for modelling purposes. However, they are not easily measured or determined in a physical machine. In fact, the design characteristics as provided from a manufacturer are attained through physical tests and relates to measurements done at the armature terminals [13]. The measured parameters are known as operational or standard parameters. One set of parameters are given for each of the different states of operation the machine attains during acceleration. Namely, the subtransient, transient and synchronous state. In each state of operation, the corresponding set of parameters are "seen" from the terminals point of view. The parameters used in this project are given in table 2.1.

Table 2.1: Synchronous generator standard parameters

Symbol	Value	Description
T'_{d0}	2.205	d-axis open circuit transient time constant [s]
T''_{d0}	0.0267	d-axis open circuit subtransient time constant [s]
T''_{q0}	0.051176	q-axis open circuit subtransient time constant [s]
x_d	2.45	d-axis reactance [pu]
x'_d	0.2	d-axis transient reactance [pu]
x''_d	0.15	d-axis subtransient reactance [pu]
x_q	1.45	q-axis reactance [pu]
x''_q	0.17	q-axis sub-transient reactance [pu]
x_σ	0.0545	Leakage reactance [pu]
r_a	0.013184	Armature resistance [pu]

A conversion from standard to fundamental parameters is needed to fit the equivalent circuit model. Expressions for conversion can be found in appendix A.4. The converted fundamental parameters is presented in table 2.2.

Table 2.2: Synchronous generator fundamental parameters

Symbol	Value	Description
x_f	2.5364	Field winding reactance [pu]
x_D	2.7336	d-axis damper winding reactance [pu]
x_Q	1.5214	q-axis damper winding reactance [pu]
r_f	0.0033	Field winding resistance [pu]
r_D	0.0433	d-axis damper winding resistance [pu]
r_Q	0.0789	q-axis damper winding resistance [pu]
x_{ad}	2.3955	d-axis mutual reactance [pu]
x_{aq}	1.3955	q-axis mutual reactance [pu]

2.3.6 Excitation Controller

Now moving on to consider the typical method of control for a diesel-generator.

To control the generator voltage a PI controller can be used on the field excitation like shown in the block diagram in figure 2.4. The exciter delay is approximated by a low pass filter with a time constant of $0.2s$. This is a little longer than usual for static exciters where a delay of $0.05s$ to $0.1s$ is normal, but when considering older types of exciters, it can be considered as a good representation.

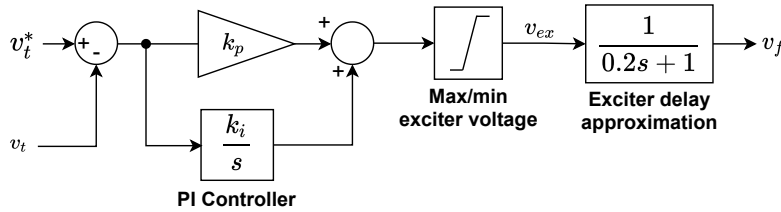


Figure 2.4: The exciter PI controller.

There is a saturation on the control signal because of physical limitations in the excitation system, which is set to be $0 < v_{ex} < 6$. The per-unit system used in the exciter control system is not the same as in the synchronous machine model. In the excitation per-unit system, a field voltage of 1 pu gives a field current of 1pu. This will be further discussed in section 2.7.

2.3.7 Speed Controller and Diesel Engine

The variable speed generator, considered in this thesis, is not operated in parallel with any other generation units. The speed droop functionality usually included for generators operating in parallel is therefore not relevant here, but will be included

in the VSM control system. The speed controller is a PI controller with integral windup limit. The windup limit can be a useful feature when the reference signal is to change during run time, which is the case here. A power reference is added as a feed forward term so that the fuel command starts at an appropriate level. In the case of variable speed reference control, the feed forward can alternatively be replaced by the load power so that the torque command will respond faster to load change.

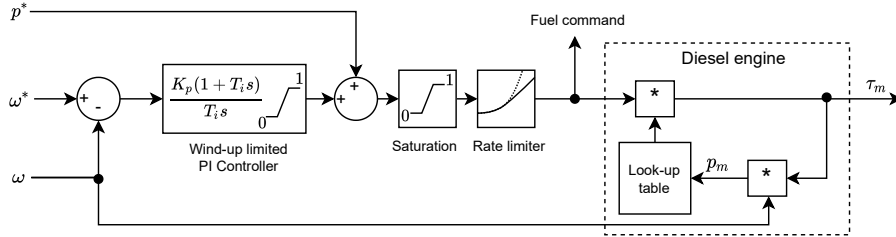


Figure 2.5: Speed control and diesel engine model.

As shown in figure 2.5, the diesel engine’s nonlinear speed-torque characteristic can be included in the simulation using a look-up table made from manufacturer data. In this project, however, emphasis has not been placed on accurate modelling of diesel engine characteristics. The assumption of a linear relation is therefore made so that the torque is proportional to the fuel command. Furthermore, higher frequency power oscillations due to cylinder firings are neglected. A low pass filter is commonly used to approximate fuel injection mechanism time delay. This delay is assumed to be very small compared to the diesel generator inertia and can be neglected for the purpose of this project.

2.4 Per unit system

The modelling in this thesis is performed using per unit normalized quantities. Using a per unit representation offers many advantages especially in large and complex systems. The readability of simulation results is much better in per unit. Model trouble shooting is made simpler as any variable not attaining the expected value is easily detected. A per unit quantity is general defined as (2.29).

$$\text{pu value} = \frac{\text{actual value}}{\text{base value}} \tag{2.29}$$

Conversion steps or transformers may, however, lead to some confusion because the base values changes with the conversion.

There are three per unit "zones" in the power system considered in this thesis. Namely, the AC zone, the DC low-voltage zone and the DC high-voltage zone. The

apparent power is kept the same between zones, but the base voltage, current and impedance changes. The base values are the same on both sides of the AC-DC-AC conversion, meaning that the VSDG and the AC grid has identical per unit base values. The DC low voltage side base values are defined using the ideal diode rectifier voltage formula, while the DC high voltage side base values are defined from the required DC voltage in order to avoid VSM over-modulation. The per unit base values for the three zones are shown in table 2.3.

Table 2.3: Power system base values.

Symbol	Expression	Description
V_{ph}	398.37	Rated phase RMS voltage [V]
I_n	740.54	Rated line current [A]
$V_{s,b}$	$\sqrt{2}V_{ph}$	Base Voltage [V]
$I_{s,b}$	$\sqrt{2}I_n$	Base current [A]
S_b	$3V_{b,ph}I_b$	Base apparent power [VA]
f_b	60	Base frequency [Hz]
ω_b	$2\pi f_b$	Base angular frequency [rad/s]
Z_b	$\frac{V_{b,ph}}{I_b}$	Base impedance [Ω]
L_b	$\frac{Z_b}{\omega_b}$	Base inductance [H]
C_b	$\frac{1}{\omega_b Z_b}$	Base capacitance [F]
$V_{b,dc1}$	$\frac{V_{b,ll}3\sqrt{2}}{\pi}$	Base dc voltage, low voltage side [V]
$I_{b,dc1}$	$\frac{S_b}{V_{b,dc1}}$	Base dc current, low voltage side [A]
$Z_{b,dc1}$	$\frac{v_{b,dc1}}{I_{b,dc1}}$	Base impedance, low voltage side [Ω]
$V_{b,dc2}$	$V_{ph}2\sqrt{2}$	Base dc voltage, high voltage side [V]
$I_{b,dc2}$	$\frac{S_b}{V_{b,dc2}}$	Base dc current, high voltage side [A]
$Z_{b,dc2}$	$\frac{v_{b,dc2}}{I_{b,dc2}}$	Base impedance, low voltage side [Ω]

2.5 Rectifier

A short discussion on two ways of representing the six-pulse diode bridge rectifier follows. Firstly, an average model representation, and secondly, the Simulink library circuit simulation. In both cases, the diode rectifier per unit definition of voltage is in accordance with the ideal voltage relation (2.30) for a three-phase diode rectifier [20].

$$V_{dc,b1} = \frac{V_{b,ll}3\sqrt{2}}{\pi} \quad (2.30)$$

In the simplified model, the commutation voltage drop (2.31) is the only component included to represent the rectifier, in addition to the per unit conversion.

$$\Delta v_d = \frac{3}{2\pi}\omega l_s i_s \quad (2.31)$$

The commutation interval in a diode bridge rectifier occurs during a short period before and after the line voltage changes polarity. A current source at the dc side retains the dc current while the ac side current cannot change direction instantaneously due to the line inductance (or in this case the inductance of the generator armature windings) [20]. In this interval two pairs of diodes are conducting at the same time, creating a short circuit which decreases the average dc voltage.

Moving now on to consider the detailed Simulink rectifier model. Figure 2.6 shows an example of the voltage and current waveforms at the generator terminals with an ideal current source on the rectifier dc side. As seen in the figure, the waveforms contain higher order harmonics. Specifically, the fifth, seventh, eleventh, thirteenth, etc., in decreasing magnitude. In order to gain some insight into the rectifier power

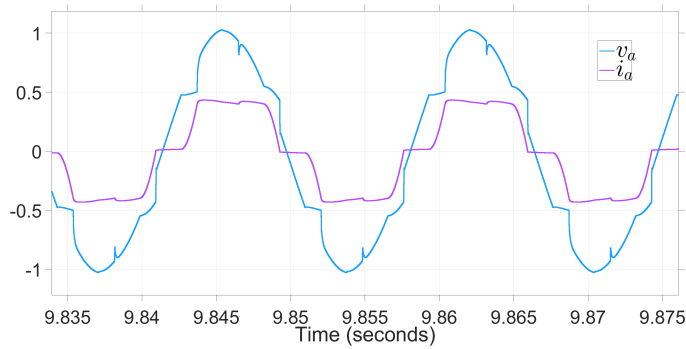


Figure 2.6: Terminal voltage and current showing displacement due to commutation.

factor the Simulink FFT analysis tool was used to determine the displacement angle between the first harmonic current and voltage. One test was performed at full speed

and a second test at half speed. The definition of power factor as stated in [20] reads as (2.32) where the rms value of the first harmonic current component over the total rms current is multiplied by the displacement power factor (DPF).

$$PF = \frac{I_1}{I_{tot}} DPF, \quad DPF = \cos \Phi_1 \quad (2.32)$$

Where the Φ_1 is the displacement between first harmonic current and voltage. The Simulink library RMS tool was used to attain the real power factor for various loads in steady state. The power factor was found to be close to unity in the range of operation.

Assuming unity power factor is in fact quite reasonable especially when considering a power factor correcting boost converter as described in chapter 18 of [20] or [22]. The boost converter with cascaded control can be used to perform power factor correction simply by modifying the inductor current reference to the shape of the ideal rectified voltage. The current is then reduced around the commutation intervals and increased in between. The average current over one cycle remains the same.

A snubber circuit is included only for numerical purposes and has been tuned in relation to the simulation time step ($t_s = 7.5e - 5$). A small R_{snub} and large C_{snub} results in reduced voltage ripple and is favorable for numerical reasons, while it also has the side-effect of a power loss in the snubber circuit. With respect to the project context, an ideal rectifier without any power loss would be most suitable. The parameters in table 2.4 results from a compromise between simulation speed, numeric stability and minimal snubber power loss.

Table 2.4: Diode bridge rectifier setup

Symbol	Value	Description
R_{snub}	8	Snubber resistance [Ω]
C_{snub}	$250e - 8$	Snubber capacitance [F]
R_{on}	0.001	On resistance [Ω]
V_{on}	1.7	Forward voltage [V]

2.6 Boost Converter

The boost converter increases the dc voltage at the input to a higher level at the output. The switch operates at a constant switching frequency and the switch on/off time for each switching cycle is controlled by the duty cycle d such that, $t_{on} = dT_s$ and $t_{off} = (1 - d)T_s$. The circuit diagram of a boost converter is shown in figure 2.7.

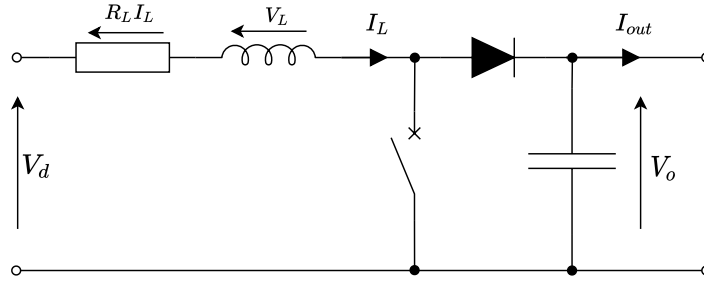


Figure 2.7: Boost converter circuit diagram.

During the switch on period an increased current is drawn from the source — transporting energy to the inductor. Meanwhile, the capacitor maintains the output voltage, supplying energy to the load as the diode is reverse-biased. Then, at the switch off period, the diode becomes forward biased and energy is transported from both the source and inductor to the capacitor and load [20]. The increase in inductor current during the switch on period causes the average inductor current to be higher than the average load current. As such, the energy stored in the inductor periodically ramps up the output voltage. All modelling done in this project assumes that the boost converter operates in continuous conduction mode (CCM) where the inductor current flows continuously at a level above zero. This greatly simplifies the average modelling because the input and output voltages and currents are simply related by the switch duty cycle d . The average model (2.33) is found by averaging over one switching period T_s ,

$$L \frac{dI_L}{dt} = V_d - R_L I_L - (1 - d)V_o \quad (2.33a)$$

$$C \frac{dV_o}{dt} = (1 - d)I_L - I_o \quad (2.33b)$$

where $t_{on} = dT_s$ and $t_{off} = (1 - d)T_s$.

2.6.1 Per unit conversion

The per unit conversion of reactive components in a DC system may seem somewhat ambiguous as the base impedance is a function of base frequency. Nonetheless, the conversion still works with the base frequency chosen arbitrarily. For convenience the AC side base frequency is used also when dealing with DC-voltage. The basic

base value relations are given in equation (2.34).

$$Z_b = \omega_b L_b = \frac{1}{\omega_b C_b} \quad (2.34a)$$

$$V_b = Z_b I_b = \omega_b L_b I_b \quad (2.34b)$$

$$I_b = \frac{V_b}{Z_b} = \omega_b C_b V_b \quad (2.34c)$$

The dynamic equations (2.33) are converted as shown in (2.35),

$$\frac{L \frac{dI_L}{dt}}{\omega_b L_b I_b} = \frac{V_d}{V_b} - \frac{R_l I_L}{Z_b I_b} - \frac{(1-d)V_o}{V_b} \quad (2.35a)$$

$$\frac{C \frac{dV_o}{dt}}{\omega_b C_b V_b} = (1-d)I_L - I_o \quad (2.35b)$$

which in per unit reads as (2.36).

$$\frac{di_l}{dt} = \frac{\omega_b}{l} (v_d - r_l i_l - (1-d)v_o) \quad (2.36a)$$

$$\frac{dv_o}{dt} = \frac{\omega_b}{c} ((1-d)i_l - i_o) \quad (2.36b)$$

The circuit equations are written on state-space form in (2.37).

$$\begin{bmatrix} \dot{i}_l \\ \dot{v}_o \end{bmatrix} = \begin{bmatrix} -\frac{\omega_b r_l}{l} & -\frac{\omega_b (1-d)}{l} \\ \frac{\omega_b (1-d)}{c} & 0 \end{bmatrix} \begin{bmatrix} i_l \\ v_o \end{bmatrix} + \begin{bmatrix} \frac{\omega_b}{l} & 0 \\ 0 & -\frac{\omega_b}{c} \end{bmatrix} \begin{bmatrix} v_d \\ i_o \end{bmatrix} \quad (2.37)$$

A block diagram of the average model boost converter is shown in figure 2.8. The conventional cascaded control loops implemented in 2.6.3 is also included in the diagram.

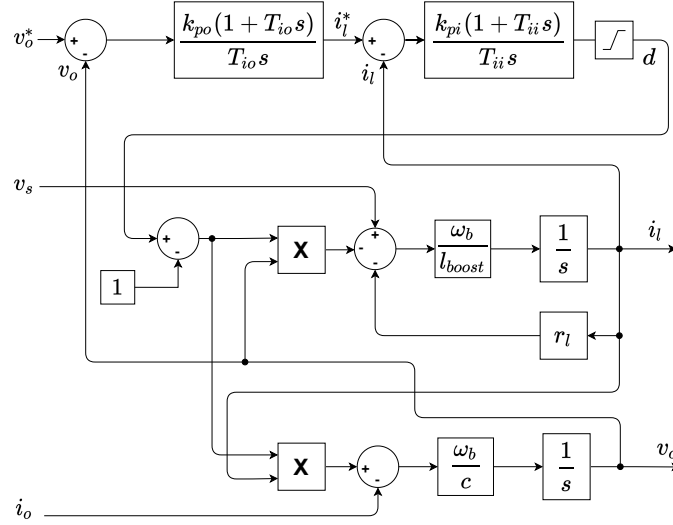


Figure 2.8: Block diagram of the boost converter.

2.6.2 Linearization

The system is linearized around an operating point like described in section 2.1.1. Defining $d = D + \hat{d}$, $i_l = I_l + \hat{i}_l$, $v_o = V_o + \hat{v}_o$, where the capital letter indicates operating point and the hat-symbol indicates a small deviation from the operating point. The operating point for capacitor voltage V_o and input voltage V_s are set to $1pu$, while the output current operating point I_o is set according to the load situation. Equations (2.38) for duty cycle D and inductor current I_l operating points are found by assuming the system (2.37) in steady state, and solving for i_l and d with the derivative states set to zero.

$$I_l = \frac{V_s - \sqrt{V_s^2 - 4I_o r_l V_o}}{2r_l} \quad (2.38a)$$

$$D = \frac{2V_o - V_s - \sqrt{V_s^2 - 4I_o r_l V_o}}{2V_o} \quad (2.38b)$$

The linearized open loop system (2.39) is found by calculating the jacobian matrices at the equilibrium.

$$\begin{bmatrix} \hat{\dot{i}}_l \\ \hat{\dot{v}}_o \end{bmatrix} = \begin{bmatrix} -\frac{\omega_b r_l}{l} & -\frac{\omega_b(1-D)}{l} \\ \frac{\omega_b(1-D)}{c} & 0 \end{bmatrix} \begin{bmatrix} \hat{i}_l \\ \hat{v}_o \end{bmatrix} + \begin{bmatrix} \frac{\omega_b}{l} & 0 & \frac{\omega_b V_o}{l} \\ 0 & -\frac{\omega_b}{c} & -\frac{\omega_b I_l}{c} \end{bmatrix} \begin{bmatrix} \hat{v}_s \\ \hat{i}_o \\ \hat{d} \end{bmatrix} \quad (2.39)$$

2.6.3 Linear system State Feedback

A conventional method for state feedback modelling is to include two cascaded PI controllers in the linearized system, one for the inner current loop, and a second for

the outer voltage loop. The outer loop provides reference for the inner loop.

The boost converter could in fact be controlled by a single PI or PID controller on the voltage, acting directly on the duty cycle. The inductor current would in that case be an uncontrolled state floating to a value satisfying the voltage regulation. However, the cascaded controller is often used because it provides superior settling time and lower overshoot by imposing tight control on the inductor current.

The general state feedback equation reads as (2.40).

$$\mathbf{u} = \mathbf{F}r - \mathbf{K}\mathbf{x} \quad (2.40)$$

The \mathbf{F} and \mathbf{K} gain matrices are formed such that the duty cycle perturbation input \hat{d} is given by the cascaded controller equations (2.41).

$$\hat{i}_l^* = k_{pi}(\hat{v}_o^* - \hat{v}_o) + k_{io}\gamma \quad (2.41a)$$

$$\frac{d\gamma}{dt} = \hat{v}_o^* - \hat{v}_o \quad (2.41b)$$

$$\hat{d} = k_{pi}(\hat{i}_l^* - \hat{i}_l) + k_{ii}\zeta \quad (2.41c)$$

$$\frac{d\zeta}{dt} = \hat{i}_l^* - \hat{i}_l \quad (2.41d)$$

The state-space is expanded to include the controllers such that $u = [\hat{v}_s, \hat{i}_o, \hat{d}, \hat{i}_l^*, \hat{v}_o^*]'$, $r = [\hat{v}_s, \hat{i}_o, \hat{v}_o^*]'$ and $x = [\hat{i}_l, \hat{v}_o, \zeta, \gamma]'$. The state feedback equation (2.40) on matrix form becomes (2.42).

$$\begin{bmatrix} \hat{v}_s \\ \hat{i}_o \\ \hat{d} \\ \hat{i}_l^* \\ \hat{v}_o^* \end{bmatrix} = \begin{bmatrix} 1 & 0 & 0 \\ 0 & 1 & 0 \\ 0 & 0 & k_{po}k_{pi} \\ 0 & 0 & k_{po} \\ 0 & 0 & 1 \end{bmatrix} \begin{bmatrix} \hat{v}_s \\ \hat{i}_o \\ \hat{v}_o^* \end{bmatrix} - \begin{bmatrix} 0 & 0 & 0 & 0 \\ 0 & 0 & 0 & 0 \\ k_{pi} & k_{pi}k_{po} & -k_{ii} & -k_{pi}k_{io} \\ 0 & k_{po} & 0 & -k_{io} \\ 0 & 0 & 0 & 0 \end{bmatrix} \begin{bmatrix} \hat{i}_l \\ \hat{v}_o \\ \zeta \\ \gamma \end{bmatrix} \quad (2.42)$$

The closed loop system A and B matrices are found using equation (2.43).

$$\dot{\mathbf{x}} = \mathbf{A}\mathbf{x} + \mathbf{B}\mathbf{u} = \mathbf{A}\mathbf{x} + \mathbf{B}(\mathbf{F}r - \mathbf{K}\mathbf{x}) = (\mathbf{A} - \mathbf{B}\mathbf{K})\mathbf{x} + \mathbf{B}\mathbf{F}r \quad (2.43)$$

The final closed loop state-space system (2.44) has the system matrix $(\mathbf{A} - \mathbf{B}\mathbf{K})$ and

the input matrix (\mathbf{BF}).

$$(\mathbf{A} - \mathbf{BK}) = \begin{bmatrix} \frac{\omega_b(r_l + k_{pi}V_o)}{l} & -\frac{\omega_b(1-D) + k_{pi}k_{po}\omega_bV_o}{l} & \frac{k_{ii}\omega_bV_o}{l} & \frac{k_{io}k_{pi}\omega_bV_o}{l} \\ \frac{k_{pi}\omega_bI_l + \omega_b(1-D)}{c} & \frac{k_{pi}k_{po}\omega_bI_l}{c} & -\frac{k_{ii}\omega_bI_l}{c} & -\frac{k_{io}k_{pi}\omega_bI_l}{c} \\ -1 & -k_{po} & 0 & k_{io} \\ 0 & -1 & 0 & 0 \end{bmatrix} \quad (2.44a)$$

$$\mathbf{BF} = \begin{bmatrix} \frac{\omega_b}{l} & 0 & \frac{k_{pi}k_{po}\omega_bV_c}{l} \\ 0 & -\frac{\omega_b}{c} & \frac{k_{pi}k_{po}\omega_bI_l}{c} \\ 0 & 0 & k_{po} \\ 0 & 0 & 1 \end{bmatrix} \quad (2.44b)$$

2.6.4 Simplified Boost Converter Model

A simplified model where the inner loop dynamics are neglected is now considered. The simplification is done by assuming the inductor current to perfectly follow the current reference from the outer loop controller. The dynamic equation for current and the inner loop controller is then replaced by algebraic relations. Considering the average case over one switch cycle, the power (after the inductor resistor) is conserved and the inductor voltage is equal to zero (see figure 2.9).

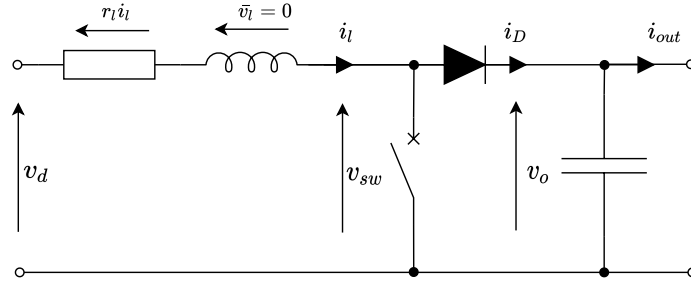


Figure 2.9: Boost converter circuit diagram.

The power conservation reads as (2.45).

$$v_{sw} i_l = v_o i_{diode} \quad (2.45)$$

Introducing the duty cycle and using Kirchoffs voltage law yields the voltage relation (2.46).

$$v_{sw} = v_d - r_l i_l = (1 - d)v_o \quad (2.46)$$

Equation (2.46) substituted into (2.45) gives the average diode current expressed in terms of the average inductor current in equation (2.47).

$$i_{diode} = \frac{(1 - d) \gamma_o i_l}{\gamma_o} \quad (2.47)$$

By rewriting (2.46) the duty cycle can be expressed as (2.48).

$$d = 1 - \frac{v_d - r_l i_l}{v_o} \quad (2.48)$$

The inductor current is given by the outer loop controller (2.49).

$$i_l = i_l^* = k_{po}(v_o^* - v_o) + k_{io}\gamma \quad (2.49a)$$

$$\frac{d\gamma}{dt} = v_o^* - v_o \quad (2.49b)$$

The capacitor equation reads as (2.50).

$$\frac{dv_o}{dt} = \frac{\omega_b}{c}(i_{diode} - i_o) = \frac{\omega_b}{c}((1-d)i_l - i_o) \quad (2.50)$$

The simplified model is fully described by combining equations (2.48),(2.49) and (2.50).

2.6.5 Model Matching

The two boost converter average models described in section 2.6, namely the cascaded controlled model and the simplified inner loop model, are here verified against the detailed switching model. A linearized version of the cascaded control model is also included in the comparison. The switching model and the cascaded control model has identical control loops while in the simplified model only the outer loop remains. The test was performed with an ideal voltage source as input voltage and an ideal current source as load. The comparison can be seen in figure 2.10 where a step is done in the voltage reference v_o^* from 1pu to 0.9pu and back to 1pu.

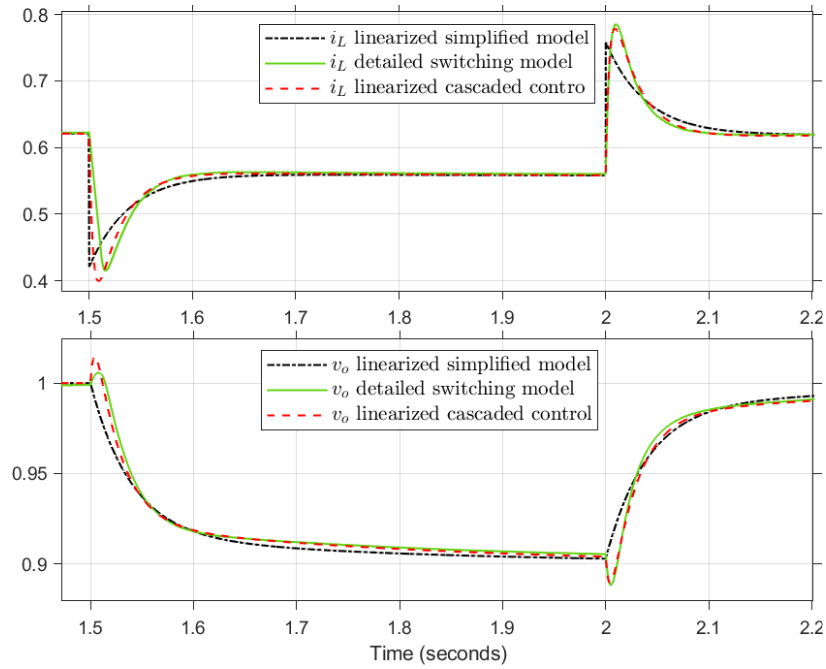


Figure 2.10: Comparison of average model and simplified model against switching model.

It can be seen in the figure that the overall response is, to some extent, similar between all three models. One key observation is that the voltage initially moves in the wrong direction when the reference step occurs. This "non-minimal-phase" characteristic is preserved by the non-simplified average model but not by the simplified-inner-loop model. The non-minimal-phase characteristic comes as a result of the inductor energy storage as exemplified in the following. If the duty cycle changes to a lower value, the inductor will initially have a current corresponding to the past duty cycle. As the switch now will be in the off-position for a longer time period, the large inductor current will initially be conducted to the load and capacitor, increasing the output voltage. After some short period of time, the inductor energy level once again matches the duty cycle, and the output voltage is decreased in line with the decreased duty cycle. As it goes for the simplified-inner-loop model, which does not include the inductor dynamics, the inductor current simply changes instantaneously.

2.7 Combining system Models

This chapter has until now described individual modelling of the synchronous machine, rectifier and boost converter. This section will go one step further and propose a simplified model combining these three components. The following simplifying as-

stator and field windings becomes (2.52).

$$v_d = -r_s i_d - \frac{x_d}{\omega_b} \frac{di_d}{dt} + \frac{x_{ad}}{\omega_b} \frac{di_f}{dt} + \omega_r x_q i_q \quad (2.52a)$$

$$v_q = -r_s i_q - \frac{x_q}{\omega_b} \frac{di_q}{dt} + \omega_r (-x_d i_d + x_{ad} i_f) \quad (2.52b)$$

$$v_f = r_f i_f - \frac{x_{ad}}{\omega_b} \frac{di_d}{dt} + \frac{x_f}{\omega_b} \frac{di_f}{dt} \quad (2.52c)$$

$$(2.52d)$$

Equation (2.52) can be solved for the current derivatives and written explicitly as (2.53).

$$\frac{di_d}{dt} = \frac{\omega_b(x_f v_d - x_{ad} v_f + x_{ad} r_f i_f + x_f r_s i_d - x_f x_q i_q \cdot \omega)}{(x_{ad}^2 - x_d x_f)} \quad (2.53a)$$

$$\frac{di_q}{dt} = -\frac{\omega_b(v_q + r_s i_q + (x_d i_d - x_{ad} i_f) \cdot \omega)}{x_q} \quad (2.53b)$$

$$\frac{di_f}{dt} = \frac{\omega_b(x_{ad} v_d - x_d v_f + x_d r_f i_f + x_{ad} r_s i_d - x_{ad} x_q i_q \cdot \omega)}{(x_{ad}^2 - x_d x_f)} \quad (2.53c)$$

The classical swing equation (2.54) provides the generator speed².

$$\frac{d\omega}{dt} = \frac{\tau_m \omega - p_e}{H} \quad (2.54)$$

The diesel engine torque output and generator excitation signal is controlled by the PI controllers (2.55) and (2.56), respectively.

$$\tau_m = k_{p,\omega}(\omega^* - \omega) + k_{i,\omega} \rho \quad (2.55a)$$

$$\frac{d\rho}{dt} = (\omega^* - \omega) \quad (2.55b)$$

$$v_{ex} = k_{p,ex}(v_t^* - v_t) + k_{i,ex} \xi \quad (2.56a)$$

$$\frac{d\xi}{dt} = (v_t^* - v_t) \quad (2.56b)$$

The exciter is approximated by a low pass filter (2.57),

$$\frac{dv_f}{dt} = \frac{r_f}{x_{ad}} \frac{v_{ex}}{T_{ex}} - \frac{v_f}{T_{ex}} \quad (2.57)$$

²Originally, a factor of 1/2 was included in the swing equation, but in order to be consistent with the Matlab library function, this factor was removed.

where the factor of r_f/x_{ad} is used to convert the exciter voltage to the machine per unit system referred to stator voltage at no-load. To clarify, the excitation system per unit definition is such that unity field voltage gives unity field current. Opposed to the per unit system for the machine, which is defined such that a unity current in the common air-gap reactance x_{ad} results in unity terminal voltage when no load is applied at the terminals. The conversion between per unit systems is discussed in [25]. In the no-load case, equation (2.52) becomes (2.58).

$$v_d = 0 \quad (2.58a)$$

$$v_q = \omega_r x_{ad} i_f \quad (2.58b)$$

$$v_f = r_f i_f \quad (2.58c)$$

Assuming $\omega_r = 1$ and $v_q = 1$ yields (2.59).

$$i_f = \frac{1}{x_{ad}} \quad (2.59a)$$

$$v_f = r_f \cdot i_f = \frac{r_f}{x_{ad}} \quad (2.59b)$$

Boost Converter

The boost converter model includes the inner loop dynamics and cascaded control (2.60).

$$i_l^* = k_{pi}(v_o^* - v_o) + k_{io}\gamma \quad (2.60a)$$

$$\frac{d\gamma}{dt} = v_o^* - v_o \quad (2.60b)$$

$$d = k_{pi}(i_l^* - i_l) + k_{ii}\zeta \quad (2.60c)$$

$$\frac{d\zeta}{dt} = i_l^* - i_l \quad (2.60d)$$

$$\frac{di_l}{dt} = \frac{\omega_b}{l}(v_d - r_l i_l - (1-d)v_o) \quad (2.60e)$$

$$\frac{dv_o}{dt} = \frac{\omega_b}{c}((1-d)i_l - \frac{v_o}{z_o}) \quad (2.60f)$$

Algebraic Relations

The algebraic coupling of voltage to the generator dynamical equations is attained through the assumption of a zero phase angle between current and voltage at the generator terminals. The d and q axis voltages (2.61) is then simply found from figure 2.12.

$$v_d = V \frac{i_d}{I} \quad (2.61a)$$

$$v_q = V \frac{i_q}{I} \quad (2.61b)$$

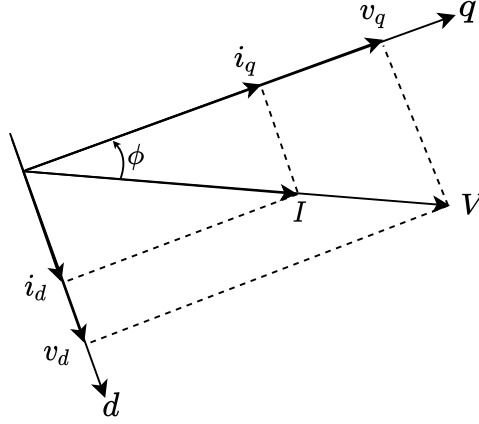


Figure 2.12: Current and voltage in phase due to diode rectifier unity power factor.

Since the voltage before and after rectification is similar in per unit (except for the commutation drop) the dc quantities are converted to the low voltage side per-unit system by (2.62).

$$i_{l,pu1} = \frac{I_{dc,b2}}{I_{dc,b1}} i_{l,pu2} \quad (2.62a)$$

$$v_{o,pu1} = \frac{V_{dc,b2}}{V_{dc,b1}} v_{o,pu2} \quad (2.62b)$$

The algebraic relation from boost converter to generator is (2.63).

$$I = i_{l,pu1} \quad (2.63a)$$

$$V = (1 - d)v_{o,pu1} + \Delta v_s \quad (2.63b)$$

$$p_e = IV \quad (2.63c)$$

where Δv_s is the commutation voltage drop (2.64a). The boost inductance (2.64b) is assumed to be a combination of the d and q axis generator sub-transient inductances due to the switching of the boost circuit.

$$\Delta v_s = \frac{3l_{boost}}{2\pi} \omega I \quad (2.64a)$$

$$l_{boost} = \sqrt{l_d''^2 + l_q''^2} \quad (2.64b)$$

The algebraic relations from generator to boost converter is (2.65).

$$v_t = \sqrt{v_d^2 + v_q^2} \quad (2.65a)$$

$$v_s = \frac{V_{dc,b1}}{V_{dc,b2}} (v_t - \Delta v_s) \quad (2.65b)$$

Explicit State Equations

The explicit state equations (2.67) are simplified using the two algebraic expressions (2.66).

$$d = k_{pi} (i_l^* - i_l) + \zeta \quad (2.66a)$$

$$V = (1 - d) v_o + \frac{3i_l \omega l_{boost}}{2\pi} \quad (2.66b)$$

The per unit conversions between dc low and high voltage side is not included, meaning that all quantities in (2.67) are in the low voltage per unit system.

$$\frac{di_d}{dt} = \frac{\omega_b (l_f V i_d - l_{ad} i_l v_f + l_{ad} i_f i_l r_f + l_f i_d i_l r_s - l_f l_q i_l i_q \omega)}{i_l (l_{ad}^2 - l_d l_f)} \quad (2.67a)$$

$$\frac{di_q}{dt} = \frac{\omega_b (l_{ad} i_f i_l \omega - V i_q - i_l i_q r_s - l_{ad} i_d i_l \omega)}{l_q i_l} \quad (2.67b)$$

$$\frac{di_f}{dt} = \frac{\omega_b (l_{ad} V i_d - l_d i_l v_f + l_{ad} i_f i_l r_f + l_{ad} i_d i_l r_s - l_{ad} l_q i_l i_q \omega)}{i_l (l_{ad}^2 - l_d l_f)} \quad (2.67c)$$

$$\frac{dv_f}{dt} = \frac{1}{T_{ex}} \left(\frac{r_f k_{p,ex}}{l_{ad}} \left(\sqrt{\left(\frac{V i_d}{i_l}\right)^2 + \left(\frac{V i_q}{i_l}\right)^2} - v_t^* \right) - \frac{r_f \xi}{l_{ad}} - v_f \right) \quad (2.67d)$$

$$\frac{d\omega}{dt} = \frac{\omega (\rho - k_{p,\omega} (\omega - \omega^*)) - V i_l}{H} \quad (2.67e)$$

$$\frac{di_l}{dt} = \frac{\omega_b}{l_{boost}} \left(\sqrt{\left(\frac{V i_d}{i_l}\right)^2 + \left(\frac{V i_q}{i_l}\right)^2} - i_l r_l + v_o (d - 1) \right) - \frac{3\omega_b i_l \omega}{2\pi} \quad (2.67f)$$

$$\frac{dv_o}{dt} = \frac{\omega_b}{c} \left(i_l (1 - d) - \frac{v_o}{z_o} \right) \quad (2.67g)$$

$$\frac{d\zeta}{dt} = -k_{i,i} (i_l - \gamma + k_{p,o} (v_o - v_o^*)) \quad (2.67h)$$

$$\frac{d\gamma}{dt} = -k_{i,o} (v_o - v_o^*) \quad (2.67i)$$

$$\frac{d\xi}{dt} = k_{i,ex} \left(v_t^* - \sqrt{\left(\frac{V i_d}{i_l}\right)^2 + \left(\frac{V i_q}{i_l}\right)^2} \right) \quad (2.67j)$$

$$\frac{d\rho}{dt} = -k_{i,\omega} (\omega - \omega^*) \quad (2.67k)$$

2.8 Model Verification

The project model(b) for generator, rectifier and boost converter, presented in section 2.7, is in the following compared to a detailed model(a) made using Matlab library

functions. The Simscape Specialized Power Systems library is used when modelling the detailed electrical circuits for generator, rectifier and boost converter. The boost converter model used in the detailed simulation does not include boost switching events because it is made by using an ideal voltage and current source in place of the switch and diode, respectively. These ideal sources are controlled by the algebraic relations (2.46, 2.47), which are repeated here for convenience. The output voltage v_o and inductor current i_l are attained using Simulink measurement blocks.

$$\begin{aligned} v_{sw} &= (1 - d)v_o \\ i_{diode} &= (1 - d)i_l \end{aligned}$$

In the detailed model(a), the rectifier is set up according to table 2.4 and the generator model is parameterized using the fundamental parameters in table 2.2. The classical control system is used including a PI regulator for speed control, a PI regulator for excitation control and cascaded boost converter controller.

The response after an increase in resistive load, on the DC high voltage side, is used in the following comparison. The speed reference is increased with the load as will be described later in 3.1.1. In figure 2.13 the boost converter input v_s and output voltage v_o is shown. The subscript (a) denotes detailed model, while (b) denotes project model. The ripple seen in some of the figures is from the detailed model rectifier.

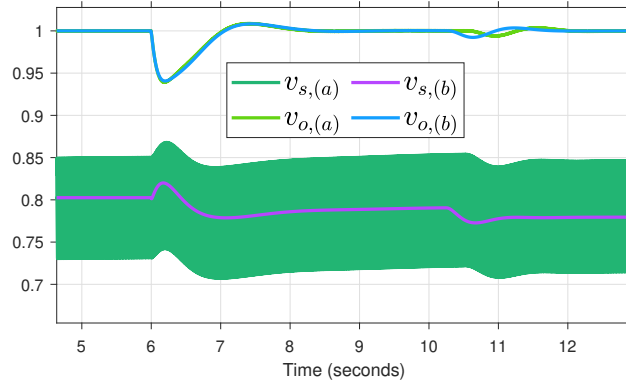


Figure 2.13: Detailed model vs project model. DC voltage — low-voltage (v_s) and high-voltage (v_o) side.

The field voltage in figure 2.14 is the variable with the largest deviance between the models. Some deviance is expected in the control inputs due to modelling error, while the controlled variables should be more similar in both models.

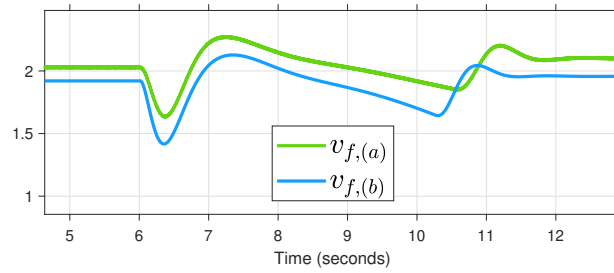


Figure 2.14: Detailed model vs project model. Field voltage.

The inductor current, shown in figure 2.15, is in the high voltage side per unit system.

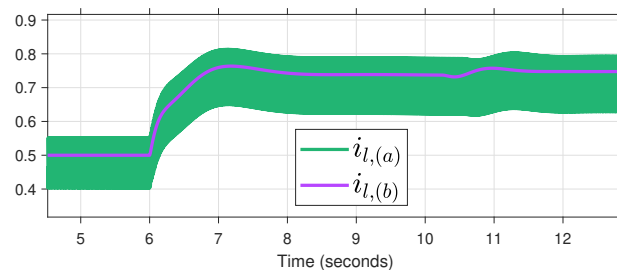


Figure 2.15: Detailed model vs project model. Boost inductor current.

The speed response after the load step, as a result of the increased speed reference, is shown in figure 2.16.

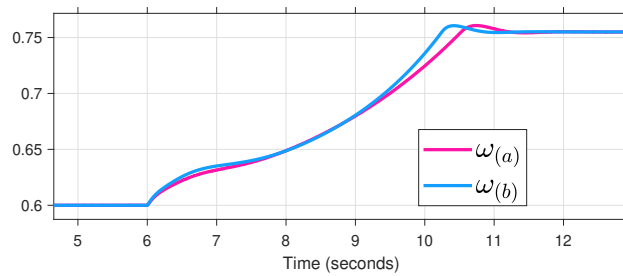


Figure 2.16: Detailed model vs project model. Generator speed.

All in all, the project model matches reasonably well with the detailed Simulink model.

2.9 Virtual Synchronous Machine

The power conversion step from dc-link to grid is the topic of this next section, which is based on work done in the specialization project, [9] and [19]. A simple first order electrical model is used together with the swing equation to emulate the synchronous machine dynamics. Figure 2.17 shows an overview of the VSM control system.

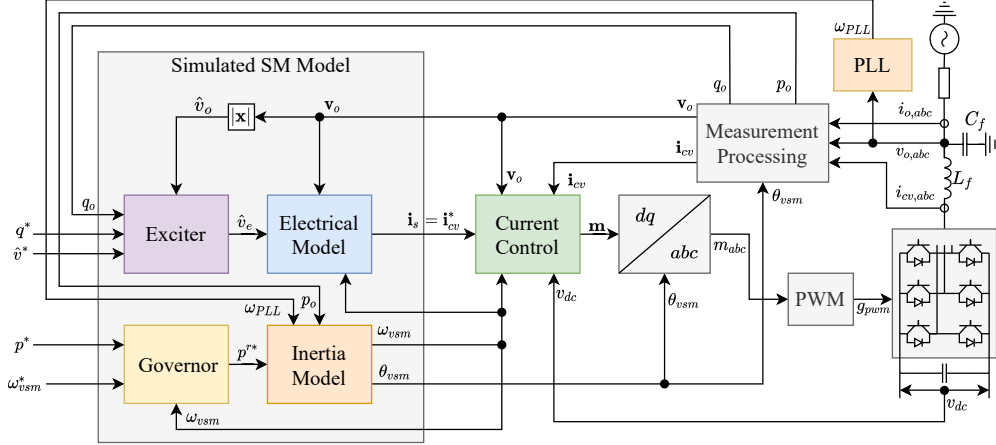


Figure 2.17: An overview of the VSM control system, inspired by [19].

Some key elements of the VSM control design is listed the following.

- All measurements are converted to the rotating frame of reference through Park transformation.
- Simple electrical model for synchronous machine stator current emulation.
- A current controller shapes the inverter current to follow the synchronous machine emulation.
- Frequency is controlled using a droop functionality in combination with the swing equation for machine emulation.
- The machine emulation is controlled by a speed controller (governor) and an voltage controller (exciter) similarly to the controllers for a physical generator.
- A phase locked loop provides the grid frequency which is included as a damping term in the swing equation. Thus, the VSM provides inertia to the grid.

2.9.1 Current controller

Figure 2.18 shows the filter model used to derive the inner loop current controller. Kirchhoffs voltage law and the inductor equation is used to derive the inductance fil-

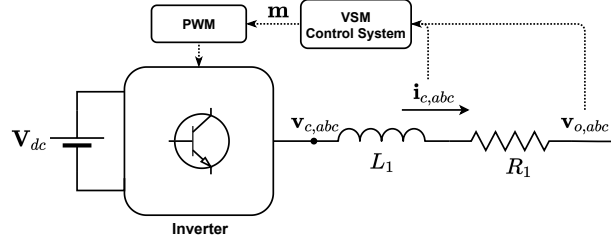


Figure 2.18: Simplified overview of inverter, VSM control system and filter inductance. Inspired by [1].

ter dynamics (2.69). The imaginary term is a result of the conversion from stationary to rotating reference frame.

$$\mathbf{v}_c = r_1 \mathbf{i}_c + \frac{l_1}{\omega_b} \frac{d}{dt} \mathbf{i}_c + j\omega_{vsm} l_1 \mathbf{i}_c + \mathbf{v}_o \quad (2.69)$$

The converter voltage \mathbf{v}_c^* is used as a system input for controlling the converter current \mathbf{i}_c . The input \mathbf{v}_c^* consists of a real part and an imaginary part as seen in (2.69). By assuming that the real part is controlled by the PI controller, we get the approximation (2.70). The imaginary part is the axis decoupling term. This yields equation (2.71) for the controlled input \mathbf{v}_c^* .

$$\mathbf{v}_{PI} \approx r_1 \mathbf{i}_c + \frac{l_1}{\omega_b} \frac{d}{dt} \mathbf{i}_c \quad (2.70)$$

$$\mathbf{v}_c^* = \mathbf{v}_{PI} + j\omega_{vsm} l_1 \mathbf{i}_c + \mathbf{v}_o \quad (2.71)$$

The output voltage \mathbf{v}_o remains as a feed forward term. Furthermore, we have the standard PI controller (2.72),

$$\mathbf{v}_{PI} = k_{pc} (\mathbf{i}_c^* - \mathbf{i}_c) + k_{ic} \gamma \quad (2.72a)$$

$$\frac{d\gamma}{dt} = \mathbf{i}_c^* - \mathbf{i}_c \quad (2.72b)$$

which implemented in (2.71) along with the feed forward gain k_{ff} yields the dynamic equation for the current controller (2.73).

$$\mathbf{v}_c^* = k_{pc} (\mathbf{i}_c^* - \mathbf{i}_c) + k_{ic} \gamma + j\omega_{vsm} l_1 \mathbf{i}_c + k_{ff} \mathbf{v}_o \quad (2.73a)$$

$$\frac{d\gamma}{dt} = \mathbf{i}_c^* - \mathbf{i}_c \quad (2.73b)$$

Tuning by Modulus Optimum

A typical tuning method for the current controller is considered here. The filter time constant T_1 and a time constant T_{sum} , for representing the PWM switching delay and any other small delays in the system, is introduced as (2.74).

$$T_1 = \frac{L}{R} = \frac{l_1}{r_1 \cdot \omega_b} \quad (2.74a)$$

$$T_{sum} = \frac{T_{sw}}{2} + T_{misc.} \quad (2.74b)$$

The transfer function from v_{PI} to filter current i_c can be defined as (2.75).

$$\frac{v_{PI}(s)}{i_c(s)} = \frac{1}{1 + T_{sum}s} \cdot \frac{1}{r_1} \cdot \frac{1}{1 + T_1s} \quad (2.75)$$

The PI controller is added to the "plant" transfer function (2.75) yielding the open loop transfer function (2.76).

$$H_{ol}(s) = k_p \frac{1 + T_i s}{T_i s} \cdot \frac{1}{1 + T_{sum}s} \cdot \frac{1}{r_1} \cdot \frac{1}{1 + T_1s} \quad (2.76)$$

The open loop transfer function has one large time constant T_1 and one small time constant T_{sum} . Therefore, the modulus optimum tuning criteria should give a reasonably well tuned controller. The modulus optimum criteria, as it is described in [3], involves setting the gain and integral time according to (2.77).

$$T_{i,c} = T_1 \quad (2.77a)$$

$$K_{p,c} = \frac{T_1 \cdot r_1}{2 \cdot T_{sum}} \quad (2.77b)$$

2.9.2 Inertia Model

The inertia model builds on the swing equation presented in section 2.3 and further includes frequency droop functionality. In (2.78a), the first two terms includes a proportional speed controller with gain k_ω and a power reference feed forward p^* . Together these terms can be interpreted as the virtual mechanical input power p_m . If ω_{vsm} is below reference, the virtual mechanical power is increased similarly to a speed governor with frequency droop. The third term is the electrical active power, calculated by (2.28b). The last term is the damping power. The damping in a synchronous machine is close to proportional to the frequency difference between machine frequency and grid [15]. With the PLL measured grid frequency ω_{PLL} included in such a manner, the damping power will act to synchronize the machine

to the grid frequency.

$$\frac{d\delta\omega_{vsm}}{dt} = \underbrace{\frac{k_\omega(\omega^* - \omega_{vsm})}{T_a} + \frac{p^*}{T_a}}_{p_m/T_a} - \frac{p}{T_a} - \frac{k_d(\omega_{vsm} - \omega_{PLL})}{T_a} \quad (2.78a)$$

$$\frac{d\delta\theta_{vsm}}{dt} = \delta\omega_{vsm} \cdot \omega_b \quad (2.78b)$$

2.9.3 Phase Locked Loop

A block diagram of the phase locked loop is shown in figure 2.19. The PLL estimates

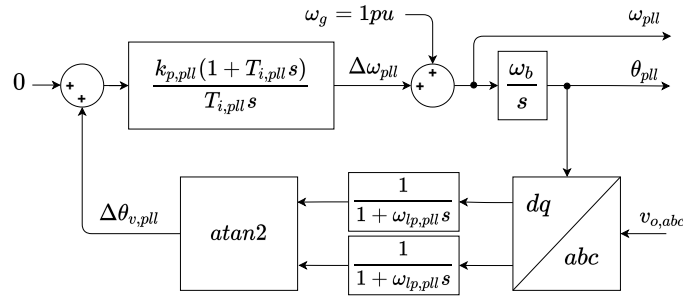


Figure 2.19: PLL block diagram. Inspired by [9].

the grid frequency and phase angle by continuously correcting the phase angle θ_{PLL} to produce a zero q-axis voltage component in the measured voltage (in the PLL rotating reference frame). As seen in the figure, θ_{PLL} is included in the feedback loop through the Park transformation of voltage measurements. The Park transform matrices are given in appendix (A.3) and (2.20). The continuously increasing voltage phase angle (stationary reference frame) is tracked by the PLL.

The phasor diagram in figure 2.20 shows the grid voltage \mathbf{v}_g , output voltage \mathbf{v}_o and the virtual internal emf \mathbf{v}_e in the VSM rotating reference frame. The $\delta\theta$ indicates an angle between two rotating phasors while θ is an angle referred to the stationary reference frame. The VSM frame of reference is used in all components of the VSM control system except for in the PLL, which operates with respect to the the PLL estimated phase angle θ_{PLL} . Therefore, the PLL can be considered to have its own rotating reference frame. The conversion between PLL and VSM reference frames can be read out of the phasor diagram. In the case of the output voltage \mathbf{v}_o the conversion becomes (2.79) [9].

$$\mathbf{v}_o^{\text{PLL}} = \mathbf{v}_o^{\text{VSM}} e^{-j(\theta_{PLL} - \theta_{VSM})} \quad (2.79)$$

Again referring to figure 2.19, the PLL output voltage $\mathbf{v}_o^{\text{PLL}}$ is low pass filtered to

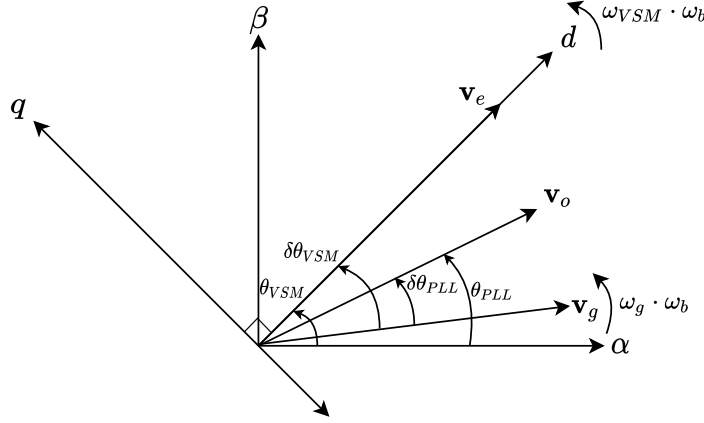


Figure 2.20: VSM phasor diagram [9].

remove noise (2.80).

$$\frac{d\mathbf{v}_{PLL}}{dt} = \omega_{lp,pll} (\mathbf{v}_o^{PLL} - \mathbf{v}_{PLL}) \quad (2.80)$$

The q-axis voltage component could in theory be used as feedback, but the arctan is included to avoid disturbance in the PLL when the voltage magnitude varies. Given that the magnitude variations are equal in all abc phases the arctan should keep the feedback steady. Equation (2.81) is the PI controller and integrator for angle estimation.

$$\omega_{PLL} = \omega_g + k_{p,pll} \arctan\left(\frac{v_{pll,q}}{v_{pll,d}}\right) + k_{i,pll} \eta_{PLL} \quad (2.81a)$$

$$\frac{d\eta_{PLL}}{dt} = \arctan\left(\frac{v_{pll,q}}{v_{pll,d}}\right) \quad (2.81b)$$

$$\frac{d\theta_{PLL}}{dt} = \omega_b \cdot \omega_{PLL} \quad (2.81c)$$

In the VSM implementation, the PLL has the sole purpose of providing the synchronizing term in (2.78). A separate measurement function performs Park transformation on circuit measurements using the VSM phase angle θ_{VSM} so that all quantities are in the dq reference frame seen in figure 2.20.

2.9.4 Voltage and Reactive Power Controller

A PI controller (2.82) is used to control the reactive power and voltage magnitude through the "control input" to the electrical model, which is the virtual internal emf

\mathbf{v}_e .

$$\hat{v}_e = k_p(k_q(q^* - q_m) + \hat{v}_o^* - \hat{v}_o) + k_i\kappa \quad (2.82a)$$

$$\frac{d\kappa}{dt} = k_q(q^* - q_m) + \hat{v}_o^* - \hat{v}_o \quad (2.82b)$$

$$\frac{dq_m}{dt} = \frac{q - p_m}{T_f} \quad (2.82c)$$

2.9.5 Electrical Model

The dynamic electrical model is used to emulate the synchronous machine electrical behavior and provides the current controller with current references. A simple model of a synchronous machine consisting of the internal emf behind the armature winding inductance and resistance is shown in figure 2.21. The corresponding dynamic equation in dq-frame is given as (2.83) [19]. Notice that this dynamic model has a

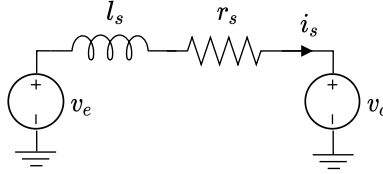


Figure 2.21: Equivalent armature winding circuit. Inspired by [24].

similar structure as the filter inductance model in equation (2.69).

$$\frac{d\mathbf{i}_s^{DEM}}{dt} = \frac{\omega_b}{l_s} (\mathbf{v}_e - \mathbf{v}_o) - \left(\frac{r_s\omega_b}{l_s} + j \cdot \omega_{vsm}\omega_b \right) \mathbf{i}_s \quad (2.83)$$

The internal emf (2.84) is directed along the d-axis.

$$\mathbf{v}_e = \begin{bmatrix} \hat{v}_e \\ 0 \end{bmatrix} \quad (2.84)$$

Assuming the armature current derivative to be zero, equation (2.83) can be rewritten to the quasi-stationary equation (2.85). A low pass filter is added to the measured output voltage \mathbf{v}_o to dampen any LC filter oscillations ($\omega_{cf} \approx 1000rad/s$ [19]).

$$\mathbf{i}_s^{QS} = \frac{\mathbf{v}_e - \mathbf{v}_m}{r_s + j \cdot \omega_{vsm}l_s} \quad (2.85a)$$

$$\frac{d\mathbf{v}_m}{dt} = \omega_{cf} \cdot \mathbf{v}_o - \omega_{cf} \cdot \mathbf{v}_m \quad (2.85b)$$

The current controller reference \mathbf{i}_c^* from section 2.9.1 is set equal to the virtual stator current such that $\mathbf{i}_c^* = \mathbf{i}_s^{QS}$ or $\mathbf{i}_c^* = \mathbf{i}_s^{DEM}$ depending on the choice of model. The inverter current is in this manner controlled in accordance with the first order electrical machine dynamic.

Chapter 3

Control

This chapter deals with the control system for the variable speed generator and boost converter like presented in section 2.7. Two control systems have been implemented for this purpose, firstly, the conventional control system consisting only of single-input-single-output (SISO) PI regulators connected in parallel and in cascade, and secondly, an adaptive linear MPC. The control systems presented here are designed separately from the VSM control system, which has already been demonstrated in the specialization project. Later, in chapter 4, the VSM will be connected to the system presented in this chapter so that a full back-to-back converter can be simulated.

3.1 Classical SISO control

The classical control system hierarchy is shown in figure 3.1.

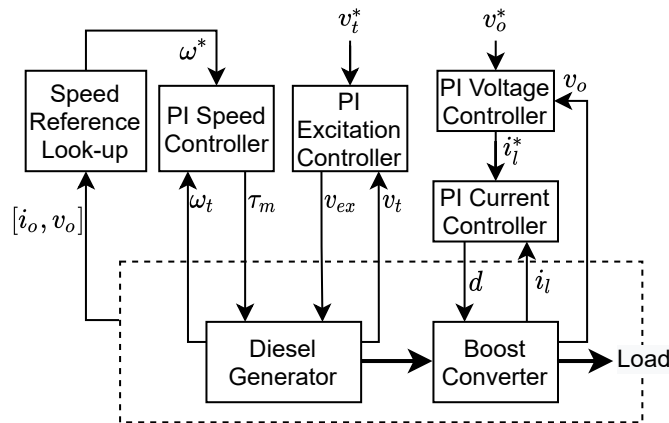


Figure 3.1: The classical SISO control system hierarchy.

3.1.1 Speed look-up

In order to increase fuel consumption, the generator speed should be reduced according to the load situation. [8] proposes that the speed reference is attained through feedback of load power-demand and a look-up table of optimal speed based on specific fuel consumption for each load level. For simplicity, the speed look-up is made linear in the simulations presented in this thesis.

An additional feedback loop of plant measurements comes with a risk of instability or oscillatory behavior. To avoid oscillations or voltage drop disturbances, the load impedance is chosen as the input to the look-up table. The load impedance is continuously calculated from the voltage and current measurements, and is less affected by voltage variations than, for example, the load power measurement. As a further measure to avoid oscillatory behavior, the speed reference is filtered through a backlash¹ and a low pass filter with time constant 0.2 sec. This method is used for both the SISO control system and the MPC presented later. A block diagram of the method is shown in figure 3.2.

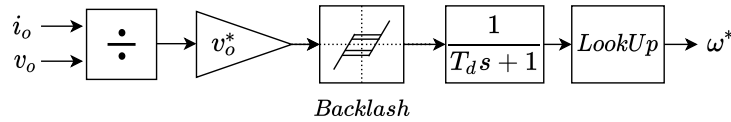


Figure 3.2: Speed reference look-up table.

3.1.2 Eigenvalues

As a tool for tuning and for ensuring steady state stability of the SISO control system, the systems eigenvalues have been considered. The VSM is not included in the model and the load impedance, therefore, becomes an input to the model. For this reason, the feedback loop resulting from the speed reference look-up is not part of the model used here. Because the actual system is highly non-linear the eigenvalue study should be considered as supplementary to the numeric simulations, providing some guidance for tuning variable setup. The eigenvalues in a state space system corresponds to the poles in the systems transfer function. An eigenvalue (or mode) takes the form (3.1).

$$\lambda = \sigma \pm j\omega \quad (3.1)$$

Complex conjugate modes represent an oscillating time response with the damped angular frequency ω in time domain. The damping of this frequency increases along the negative real axis. Intuitively, a high frequency mode should need more damping

¹The backlash acts on a signal changing direction, filtering out small ripples. I.e. a signal continuously incrementing or decrementing is unaffected by the backlash.

than a low frequency mode. Therefore, the damping ratio ζ (3.2) is a good measure of system stability.

$$\zeta = \frac{-\sigma}{\sqrt{\sigma^2 + \omega^2}} \quad (3.2)$$

A mode laying on the real axis is critically damped with $\zeta = 1$ and has zero overshoot in the time response. A critically damped mode with a small negative real part yields a slow decaying non-oscillatory time response. Since the system has numerous interconnected modes, a compromise between damping of oscillating modes and slowly decaying non-oscillatory modes may often be necessary. A damping ratio around $\zeta = 0.6$ should be suitable for oscillatory modes in most cases.

As an example, a zoomed pole-plot is shown in figure 3.3. The damping ratio for the considered mode is $\zeta = 0.63$ like indicated in the figure.

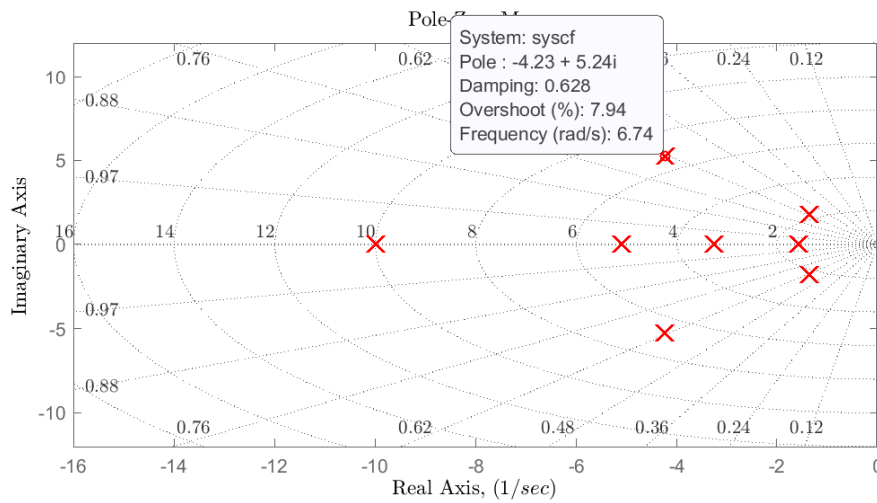


Figure 3.3: Zoomed pole plot with $k_{i,o} = 10$.

The corresponding time response in figure 3.4 is the output voltage after a small voltage reference pulse of 0.02 pu with a duration of 0.1 seconds.

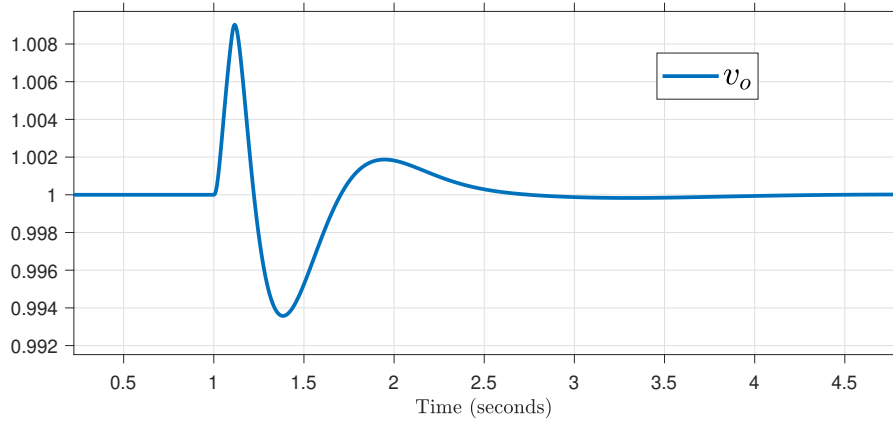


Figure 3.4: Time response v_o with $k_{i,o} = 10$.

In figure 3.5 a $k_{i,o}$ sweep is done, and it can be seen what modes are most sensitive to this parameter. $k_{i,o}$ is the outer loop voltage controller integral gain. More pole sweeps can be found in appendix A.6.

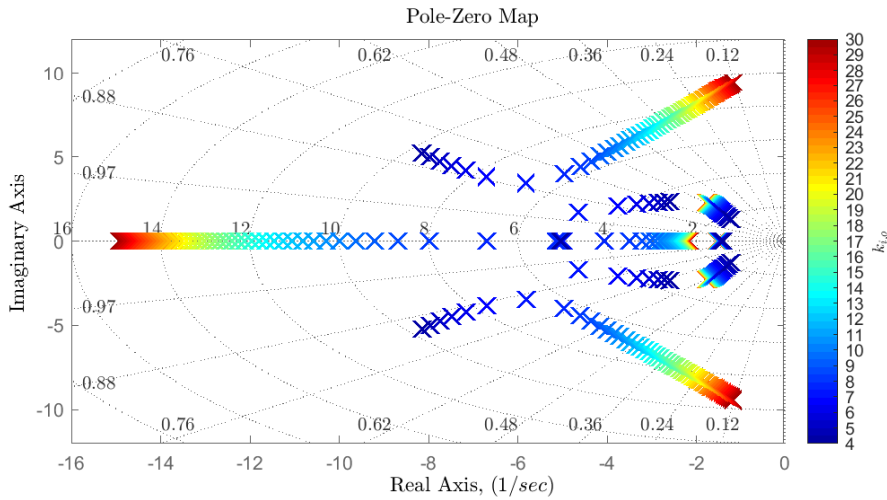


Figure 3.5: Zoomed pole plot with outer loop voltage controller integral gain $k_{i,o}$ sweep.

In figure 3.6, $k_{i,o}$ is increased from 10 to 30 in order to provoke an increased oscillation in the output voltage. In figure 3.6, the modes have shifted so that the damping and stability margin is reduced.

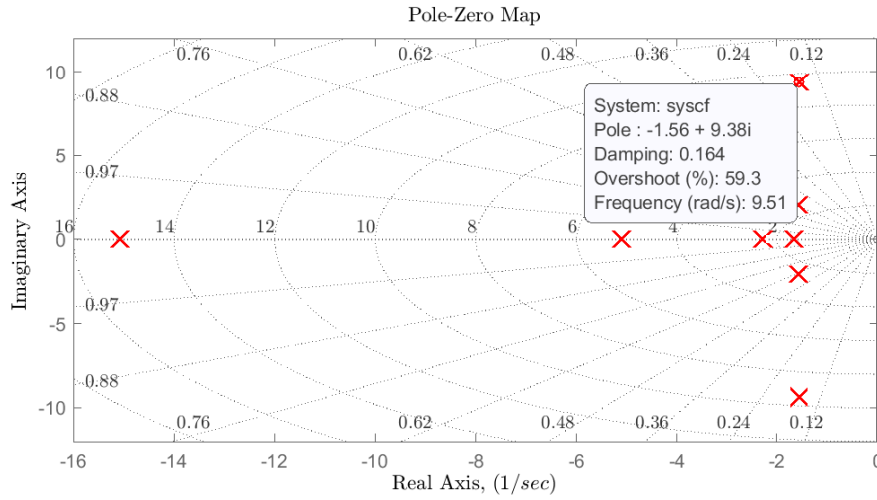


Figure 3.6: Zoomed pole plot with $k_{i,o} = 30$.

The corresponding time response, with $k_{i,o} = 30$, is shown in figure 3.7. The oscillation is here clearly less damped, not in favor of stability of the implementation. The frequency can be determined more easily from the time response in this less damped case, and compared to the pole placement for verification.

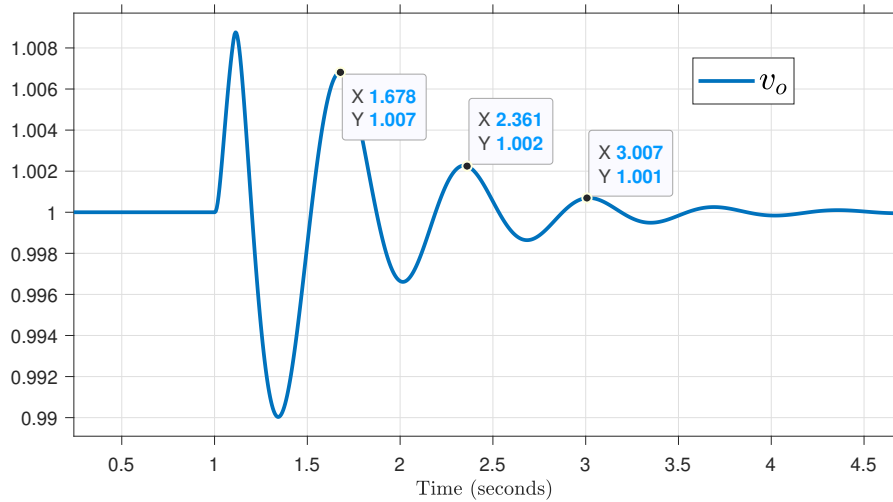


Figure 3.7: Time response v_o with $k_{i,o} = 30$.

The pole $(-1.56 \pm 9.38i)$ has the damped angular oscillation frequency $\omega = 9.38 \text{ rad/s}$.

Comparing this to figure 3.7, we have a time period $T \approx 0.66$ and $\omega = 2\pi/T \approx 9.52$. The oscillation of a specific mode is damped such that the amplitude decays 37% during a time period of $1/|\sigma| = 0.57s$, i.e. time constant of decay [13]. The rule of thumb is that steady state is reached after about $5/|\sigma| = 2.86s$, which approximately matches the observation in the time response.

As seen in figure 3.5, the pole sweeps are effective in determining the influence of a tuning variable on a mode. Another method, which may be useful in case it is difficult to find a stable tuning, is the participation factors, describing the participation of a specific state on a specific mode (and vice versa). A matrix of participation factors for all states and modes can be made using the right v and left u eigen vectors as shown in appendix A.7. As an example, consider the participation matrix (A.11). Large participation factors for the state v_o can be found in the rows corresponding to the 5th, 6th and 10th mode in table 3.2. Referring to the eigenvalue plot 3.3 and the sweep in figure 3.5, it can be seen that these modes are highly dependant on the outer loop voltage controller integral gain $k_{i,o}$.

The participation factors have not been used actively in the tuning of this system because system stability was not difficult to achieve by other means. Instead, the pole sweeps shown in appendix A.6 was used as guidance, along with experimental tuning using the numeric simulation. The tuning parameters in table 3.1 was found to give a reasonably good behavior.

Table 3.1: Tuning Parameter Setup

Symbol	Value	Description
$k_{p,i}$	0.8	Boost current controller proportional gain
$k_{i,i}$	2.0	Boost current controller integral gain
$k_{p,o}$	1.7	Boost voltage controller proportional gain
$k_{i,o}$	10	Boost voltage controller integral gain
$k_{p,\omega}$	25	Speed controller proportional gain
$k_{i,\omega}$	100	Speed controller integral gain
$k_{p,ex}$	9.0	Excitation controller proportional gain
$k_{i,ex}$	9.0	Excitation controller integral gain

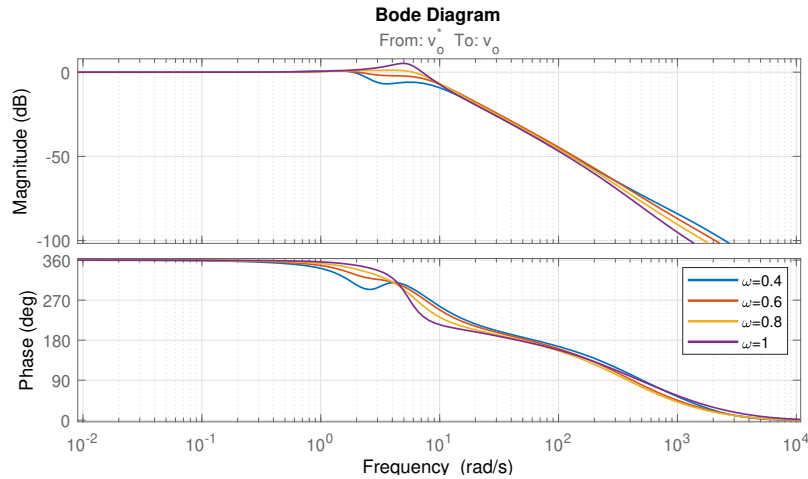
All 12 modes corresponding to the tuning setup in table 3.1 is shown in table 3.2. These modes corresponds to figure 3.3.

Table 3.2: Generator and boost converter closed loop system modes.

nr.	$1.0e + 03 \times$
1	$-4.0706 + 0.0000i$
2	$-1.9424 + 0.0000i$
3	$-0.2872 + 0.0000i$
4	$-0.0292 + 0.0000i$
5	$-0.0042 + 0.0052i$
6	$-0.0042 - 0.0052i$
7	$-0.0014 + 0.0018i$
8	$-0.0014 - 0.0018i$
9	$-0.0016 + 0.0000i$
10	$-0.0033 + 0.0000i$
11	$-0.0051 + 0.0000i$
12	$-0.0100 + 0.0000i$

3.1.3 Frequency Response

To attain further insight in the steady state system behavior, frequency response plots are made for various operating points. The operating points are chosen such that the load is set 0.2pu below the speed. E.g. $\omega^* = 0.6\text{pu} \rightarrow I_o = 0.4\text{pu}$, $\omega^* = 0.8\text{pu} \rightarrow I_o = 0.6\text{pu}$, and so on. Figure 3.8 shows the frequency response from output voltage reference v_o^* to output voltage v_o . Although the considered operating points yields quite similar frequency responses in general, it appears as the bandwidth is somewhat lower at low speed (and low load), considering the -3db point.

Figure 3.8: Bode plot from output voltage reference v_o^* to output voltage v_o .

The frequency response from load to output voltage in figure 3.9 shows that the control system is able to dampen load disturbances at various operating points.

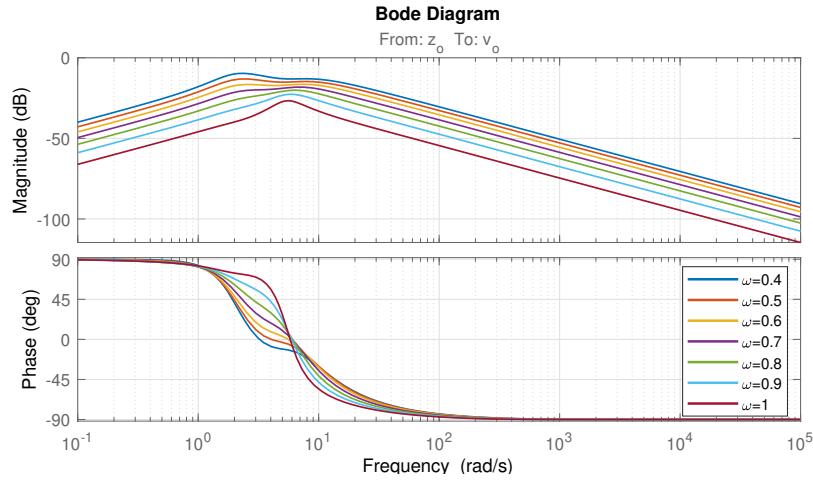


Figure 3.9: Bode plot form load z_o to output voltage v_o .

A similar plot for v_t^* to v_t is shown in figure 3.10.

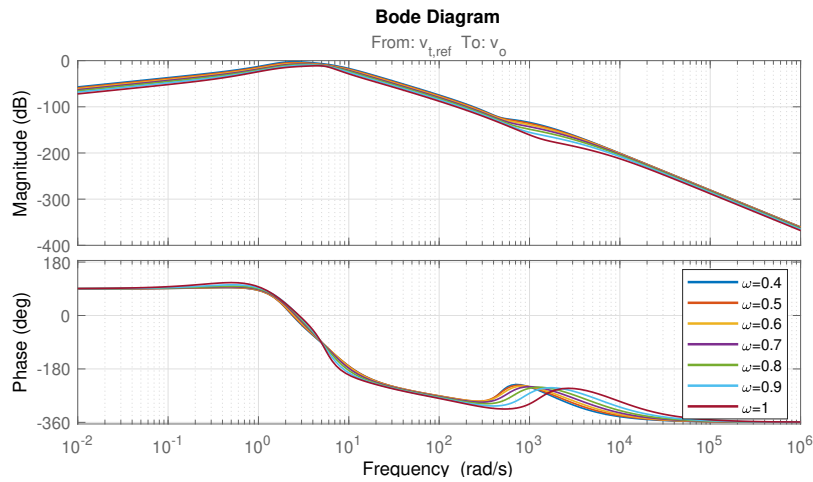


Figure 3.10: Bode plot form load v_t^* to output voltage v_o .

All in all, the frequency responses are relatively similar for the various operating points and the system has sufficient damping of disturbances, which is a good indication of robustness.

3.1.4 Cascaded Control

Now moving on to consider the cascaded control loops for the boost converter. For the inner and outer loop to be considered as decoupled, the rule of thumb is to have the inner closed loop bandwidth about 10 times larger than that of the outer loop. This rule is good to have in mind, however, it may be a better idea to allow for some coupling between the loops, and thus allow for a higher bandwidth in the outer loop.

Frequency response comparisons between inner and outer loops are presented in figures 3.11 and 3.12. Various inner and outer loop proportional gain settings are compared both by using bode plots and non-linear simulation. The inner loop input and output is i_l^* and i_l , respectively, while the outer loop is from v_o^* to v_o . The operating point used when making the bode plots is characterized by a load current of $i_o = 0.6pu$ and a generator speed of $\omega = 0.8pu$. The tuning setup for each case is added as a figure-text, where the first subscript indicates proportional or integral gain, and the second subscript indicates inner or outer loop.

In figure 3.11 the inner controller gain is set lower than the outer controller gain and the magnitude plots are somewhat closer than in a case with higher inner controller gain. It should, however, be noted that the loop gains are different in the inner and outer loops. The controller gain only contributes to the total loop gain.

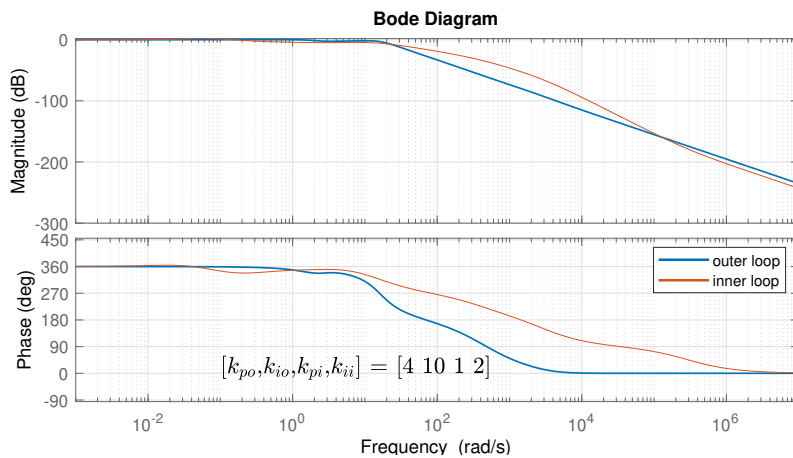


Figure 3.11: Inner and outer loop closed loop frequency response for boost converter, case 1.

In figure 3.12 the inner controller gain set to a higher value ($k_{p,i} = 8$). The magnitude plots still has similar bandwidths.

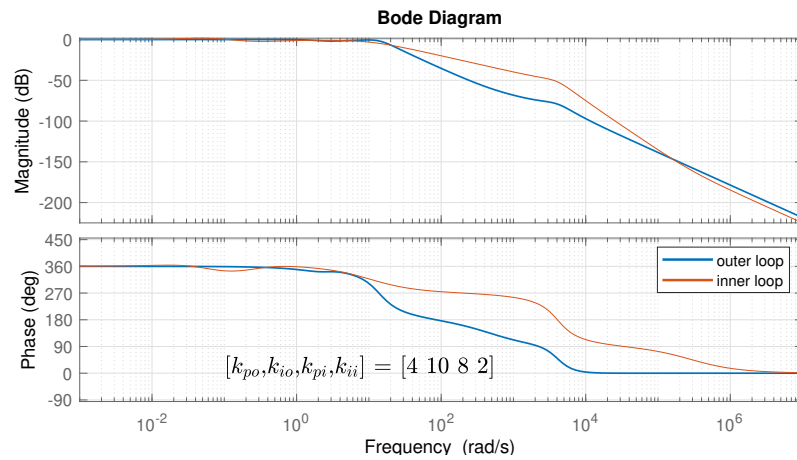


Figure 3.12: Inner and outer loop closed loop frequency response for boost converter, case 2.

The non-linear system simulation shown in figure 3.13 has the same tuning as the bode plot in figure 3.12. The simulation includes a resistive load step at $t = 4$ seconds, accompanied by a speed reference increase. The disturbance between $t = 5$ and $t = 6$ is simply caused by a drop in mechanical torque as the speed reaches its new reference after the load step.

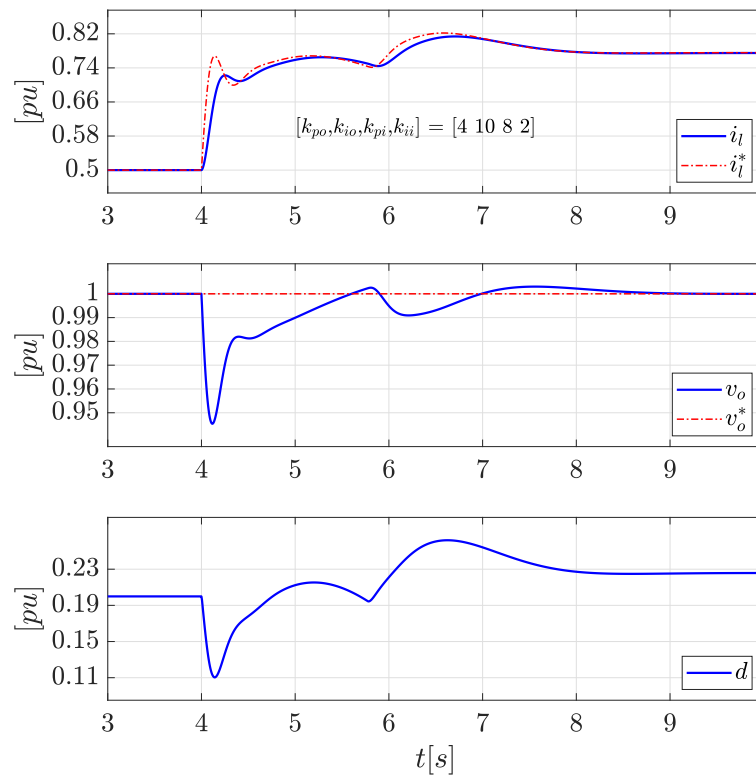


Figure 3.13: Simulation of non-linear system inner and outer loop response to load step, case 2.

It can be seen that a large inner controller gain improves inner loop reference tracking. Meanwhile, it also increases the drop in duty cycle, and thus increases the voltage drop compared to the low inner loop gain case in figure 3.14.

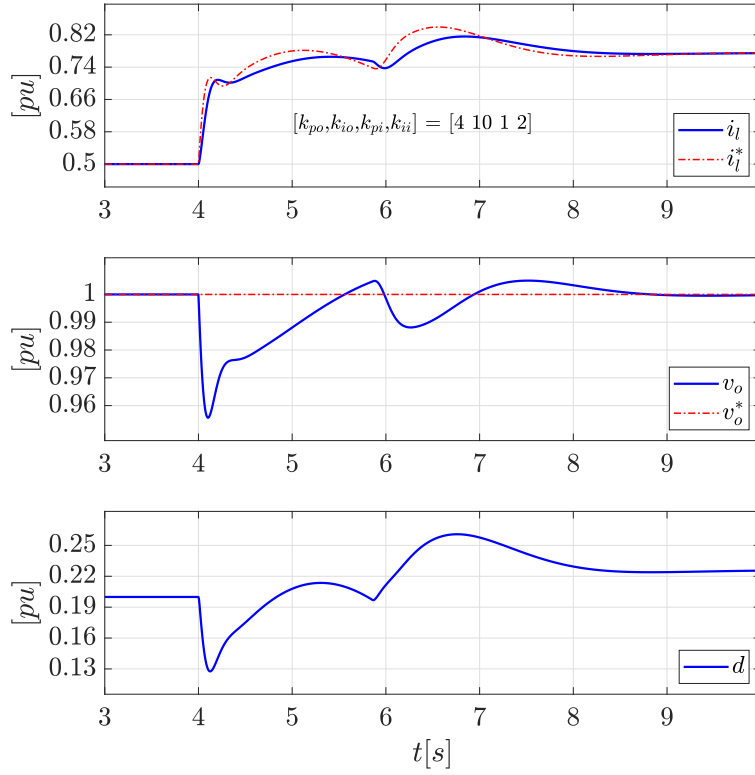


Figure 3.14: Simulation of non-linear system inner and outer loop response to load step, case 1.

In figure 3.14 the inner loop reference tracking is somewhat less accurate, but the instant voltage droop is smaller. Therefore, the low inner loop gain may be argued to be preferable.

The instant voltage drop caused by the load step should be seen in connection with the boost converter non-minimal-phase characteristic. This effect was demonstrated by simulation in figure 2.10 in section 2.6. More formally, a non-minimal-phase system does not satisfy the condition for a minimal-phase system which is that all poles and zeros are in the left half plane and that there are no time-delays [4]. The inverse of a non-minimal-phase system is unstable. A zero in the right half plane amounts to a positive magnitude contribution and a negative phase contribution. Consider the simple transfer function (3.3) with a zero in RHP.

$$H(s) = \frac{1 - T_1 s}{T_2 s} = \frac{z(s)}{p(s)} \quad (3.3)$$

The zero contributes to a magnitude (3.4) and a phase (3.5) for low, middle(3dB) and high frequencies.

$$|z(j\omega)| = \sqrt{1 + (T_1\omega)^2} = 20 \log_{10} \sqrt{1 + (T_1\omega)^2} \text{ dB}$$

$$\begin{cases} \approx 0 \text{ dB} & \omega \ll 1/T_1 \\ = 20 \log \sqrt{2} \text{ dB} \approx 3 \text{ dB} & \omega = 1/T_1 \\ \approx (20 \log_{10} \omega - 20 \log_{10} T_1) \text{ dB} = 20 \text{ dB/dec} & \omega \gg 1/T_1 \end{cases} \quad (3.4)$$

$$\angle z(j\omega) = -\arctan(T_1\omega) \begin{cases} \approx 0 & \omega \ll 1/T_1 \\ = -\pi/4 = -45^\circ & \omega = 1/T_1 \\ \approx -\pi/2 = -90^\circ & \omega \gg 1/T_1 \end{cases} \quad (3.5)$$

The zeros of the outer loop transfer function, from v_o^* to v_o , corresponding to figure 3.12 are listed in table 3.3. There is one zero in the right half plane making the system non-minimal-phase by definition.

Table 3.3: Zeros in the outer loop boost converter transfer function.

nr.	$1.0e + 03 \times$
1	$-4.3335 + 0.0000i$
2	$-1.3279 + 0.0000i$
3	$0.4838 + 0.0000i$
4	$-0.0270 + 0.0000i$
5	$-0.0049 + 0.0000i$
6	$-0.0015 + 0.0023i$
7	$-0.0015 - 0.0023i$
8	$-0.0025 + 0.0000i$
9	$-0.0019 + 0.0000i$
10	$-0.0002 + 0.0000i$

A zoomed version of the outer loop bode plot in figure 3.12, including asymptotes, is shown in figure 3.15.

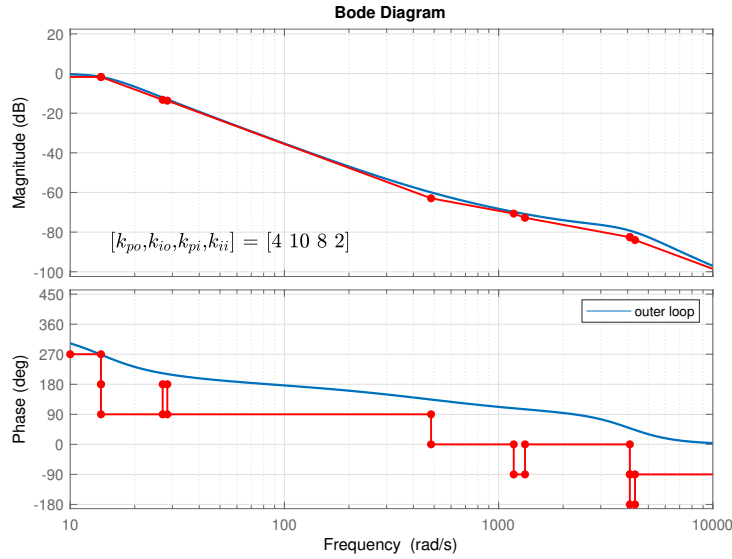


Figure 3.15: Outer (closed) loop boost converter frequency response.

All positive magnitude contributions of $20dB/dec$ can be seen to be consistent with the zeros in table 3.3. The phase contribution corresponding to the zeros are all positive except for the RHP zero at the frequency $\omega = 483.8rad/s$, where the phase has a negative -90° contribution and the magnitude has a positive $20dB/dec$ contribution. As can be seen in the bode plot, the frequency range subjected to the non-minimal-phase characteristic is well damped.

3.1.5 SISO control limitation

In the SISO control system there is no inherent mechanism that can prevent the generator air-gap power to exceed the diesel engine power capability when the speed is too low. When doing simulations it was discovered that the classical control approach, using multiple SISO controllers, had difficulties during load surges when the initial speed was limited. The generator takes some time to accelerate. Meanwhile, the load increase causes a voltage drop and, as a result, the excitation controller increases its control input. The air-gap power, increasing with excitation and load current, can cause the engine to stall if speed is too low initially.

In order to achieve a faster speed controller response, it is normal to implement derivative action. This does, however, not compensate for the lacking initial speed reserve. Attempts were also made using various cross-couplings between the speed and excitation controllers in order to hold back excitation during a drop in speed.

Some improvements could be made on specific tests, but no clear-cut solution was found that could ensure a stable trajectory in all cases. The SISO control system does function given that the speed reserve is always large enough, which would be the case in a practice system where the machinery must be dimensioned for and operated at a speed retaining necessary reserve power capability. The speed can only be reduced to a certain level, determined by knowledge about present and future load situations.

A model predictive control system can, contrary to the SISO control system, ensure acceleration to take place by limiting the air-gap power if necessary. That means, if the load surge is too large, a stable trajectory can only be attained through a momentary decrease in output voltage.

3.2 Model Predictive Controller

The model predictive controller (MPC) attains an optimal control input by solving a finite horizon weighted quadratic programming (QP) problem at each controller sampling instant [10]. The QP problem consists of a cost function with weights for every state error, control input, rates, etc., along with bounds and a plant model — constraining the solution of the QP problem. At each controller iteration a solver minimizes the QP problem, attaining an optimal trajectory for the states and control inputs. The first time step in the state trajectory is set equal to a state estimate attained through plant measurements. The calculated control input corresponding to the first time step in the horizon is selected as the control signal to be imposed on the plant during the next controller iteration. An MPC offers many favorable traits, for example:

- The MPC enables the plant to be controlled closer to its physical limit, because the state trajectory is predicted in advance.
- Enables constraints to be set on both control inputs and states in the system, enabling for optimal control within predefined limitations.
- The inherent MIMO design is highly beneficial in a plant with strong dependencies between controlled variables because the tuning is set relatively between all control objectives.

Model predictive controllers are used for various purposes in industrial applications. They are typically used in a higher control-level providing references for lower-level controllers[10]. Low-level controllers often control local processes without respect to the large-scale plant behavior. Meanwhile, the MPC which is typically running at a lower sampling rate ($t_s > 1sec$), updates the local control references for the entire plant based on the QP problem solution. An MPC can also be used with a higher sampling rate ($t_s < 1sec$), in faster control loops, to impose a more accurate control

than what can be achieved by classical controllers. The latter is the case here as will be seen in the rest of this section.

3.2.1 Control Hierarchy

The control hierarchy used for the diesel generator and boost converter is shown in figure 3.16. The basic control layer consists of the inner loop boost converter current controller.

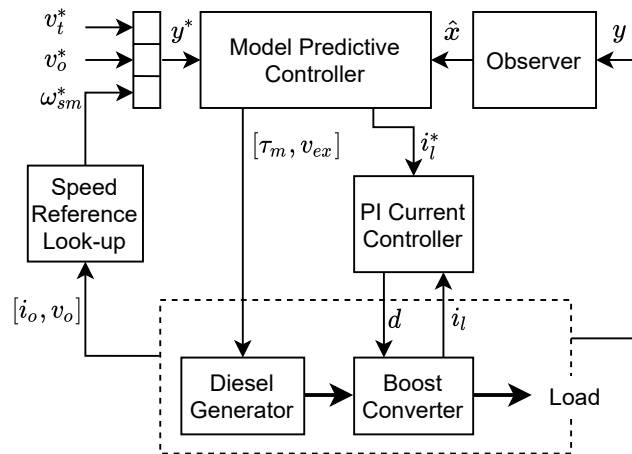


Figure 3.16: The MPC control hierarchy used in the project.

There are multiple possibilities for a control structure, and it is not obvious which one is the best. An important factor to take into consideration when deciding on a control system structure is the step response of the open loop prediction model. The model step response must be finite within the prediction horizon ($p \cdot t_s$) [16]. Basic control layer loops can be included so that the plant is stable in itself. When doing so, the sampling time and prediction horizon can be increased. The inner loop boost current controller is included in the plant for this exact reason. More about an expanded basic control layer can be found in appendix A.9.

A simpler configuration where the basic control layer was completely removed was also tested. Without the current controller, the maximal prediction horizon length ($p \cdot t_s$) is significantly limited because the open loop step response of the prediction model is only finite for a short period of time. With such a short horizon (in the range of 1-2 sek), the MPC was not able to calculate a usable optimal trajectory because of the slow generator-inertia dynamics.

3.2.2 Prediction Horizon and Sample Time

The prediction horizon must be long enough to account for the slow dynamics. Therefore, the generator inertia time constant T_m (defined in section 2.3) should be taken into account when choosing horizon length. As an example, consider a sudden load increase. The calculated optimal trajectory, using a short horizon, could increase excitation too much in order to sustain the output voltage, while not detecting an unstable speed trajectory. In this context, it is worth noting that the cost function weight Q is set higher on voltage than on speed. In other words, the MPC will tend to reduce voltage deviance in the calculated trajectory at the expense of speed deviance. Furthermore, the MPC has a prediction error due to linearization which does not act in favor of detecting an unstable speed trajectory over a short prediction horizon. With a $T_m = 2.4s$, the horizon is set even longer to account for the case in which load power is just above the engine capability. A prediction horizon in the area of 6-12 seconds has successfully been used with the structure shown in figure 3.16. The implementation demonstrated in chapter 4 has a prediction horizon length corresponding to 12 seconds. Such a long horizon may not be necessary but is used to ensure greatest possible performance.

With a fixed prediction length in seconds, the number of steps in the horizon depends on the MPC step time. A long step time reduces computational cost, while a smaller step time tends to improve disturbance rejection [16]. The combination of both slow and fast dynamics in the prediction model is somewhat challenging as it requires both a small step time and a long horizon time to include the slow dynamics. A step time up to 0.1 seconds has been used for the system in figure 3.16. However 0.06 seconds seemed to give a more robust controller and was used in the final version. The number of steps in the horizon becomes $p \cdot t_s = 12/0.06 = 200$, which is a relatively long horizon compared to normal practice. According to [16] a horizon length of more than 50 steps is rarely necessary. For a real-time implementation the horizon length may have to be shorter to limit the computational effort. The real-time implementation topic is not within the scope of this thesis.

3.2.3 Objective Function

From the Matlab documentation [17] we have the objective function (3.6), (3.10). The notation is simplified by dropping the hat for perturbed values and the bold vector notation.

$$J(z_k) = \sum_{i=0}^{p-1} \left([e_y^T(k+i)Qe_y(k+i)] + [e_u^T(k+i)R_ue_u(k+i)] \right. \\ \left. + [\Delta u^T(k+1)R_{\Delta u}\Delta u(k+i)] \right) + \rho\epsilon^2 \quad (3.6)$$

Q (3.7) is the weighing matrix for plant output errors, R_u (3.8) is the weighing matrix for control inputs and $R_{\Delta u}$ (3.9) is the weighing matrix for control inputs step change. The slack variable weight ρ_ϵ is typically set to a large value to penalize constraint violation. Furthermore, p is the prediction horizon, k is the current time step index and i is the time step index along the k -th prediction horizon.

$$Q = \begin{bmatrix} 0 & 0 & \dots & 0 & 0 & 0 & 0 & 0 \\ 0 & \ddots & \ddots & & & & & 0 \\ \vdots & \ddots & 30 & \ddots & & & & \vdots \\ 0 & & \ddots & 20 & \ddots & & & 0 \\ 0 & & & \ddots & 60 & \ddots & & 0 \\ 0 & & & & \ddots & 30 & \ddots & 0 \\ 0 & & & & & \ddots & 20 & 0 \\ 0 & 0 & \dots & 0 & 0 & 0 & 0 & 120 \end{bmatrix} \succeq 0 \quad (3.7)$$

Q , R_u and $R_{\Delta u}$ must be positive (semi)definite for the QP problem to be convex.

$$R_u = \begin{bmatrix} 0 & 0 & 0 \\ 0 & 0 & 0 \\ 0 & 0 & 0 \end{bmatrix} \succeq 0 \quad (3.8)$$

$$R_{\Delta u} = \begin{bmatrix} 400 & 0 & 0 \\ 0 & 200 & 0 \\ 0 & 0 & 400 \end{bmatrix} \succeq 0 \quad (3.9)$$

$$e_y(k+i) = r(k+i+1) - y(k+i+1) \quad (3.10a)$$

$$e_u(k+i) = u_{target}(k+i) - u(k+i) \quad (3.10b)$$

$$\Delta u(k+i) = u(k+i) - u(k+i-1) \quad (3.10c)$$

e_y is the error on the plant outputs y and e_u is the control input deviation from target input u_{target} . u_{target} is the point from which the control inputs are penalized.

$$r = [0, \dots, 0, \omega^*, 0]^T \quad (3.11a)$$

$$y = [0, \dots, v_t, \omega, v_o]^T \quad (3.11b)$$

$$u = [v_{ex}, \tau_m, i_l^*]^T \quad (3.11c)$$

$$u_{target} = [0 \ 0 \ 0]^T \quad (3.11d)$$

3.2.4 Tuning

Because the point of operation varies, there are no obvious choices for control input targets u_{target} . Therefore, it makes more sense to penalize control input rates $R_{\Delta u}$ instead of the deviance from a specific target, i.e the R_u diagonal elements are set to zero while tuning is performed on $R_{\Delta u}$. The rate penalty adds to the cost function value $J(z_k)$ by an amount depending on the control input step change size. The rate penalty setting $R_{\Delta u}$ is found experimentally by increasing the values until any oscillatory behavior after a disturbance is at an acceptable level. As an example, figure 3.17 shows a case where the rate penalty for the control input $i_{l,dc}^*$ is set low.

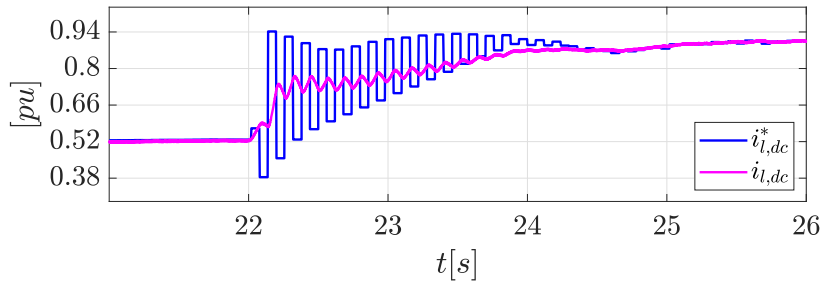


Figure 3.17: DC current control in a case with low control input rate penalty.

In some sense, a low rate penalty setting can be compared to a high gain setting on a conventional feedback controller, as both may result in oscillatory behavior. However, the limited MPC sampling rate may lead to oscillations which are not relevant to consider in a conventional controller.

The Q matrix entries corresponding to v_t , ω and v_o should be tuned by considering the relative importance of the reference tracking. For example, the weight on output voltage v_o is larger than on the speed ω , so that some deviance in speed is allowed if needed to enable voltage tracking. The same reasoning can be made for setting a relatively low weight on the terminal voltage v_t .

Moving now on to consider the slack variable penalty. Some constraint violation is often expected because of prediction error. Therefore, tuning the slack variable penalty ρ_ϵ so that the violations does not reduce control system performance might be a good idea. According to the Matlab documentation [18] a slack variable penalty reduction can be considered if a constraint violation more than doubles the cost function value.

3.2.5 Terminal Step Weights

Another important tuning parameter is the terminal step weight setting (i.e. the Q matrix for the final time step in the horizon). Intuitively, it makes sense to "force" the optimal state trajectory to the reference at the final prediction horizon step. In order to gain some insight into the MPC decision making, the calculated optimal state and input trajectories (predictions) are plotted for two separate cases after a disturbance event. The first case is with no increase in weight setting (Q) for the terminal step, and the second case with a much larger weight setting (Q) for the terminal step.

As an indication of where, in the actual time response, the investigated predictions occurs, the investigated time period is marked in figure 3.18, which is a plot of the output voltage and speed response after a load increase at $t = 1.87s$.

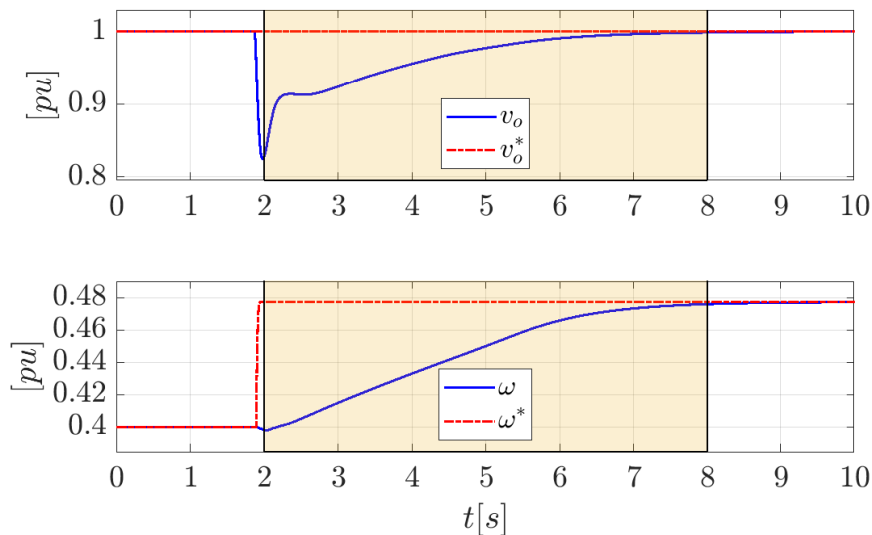


Figure 3.18: Indication of investigated time period.

Without increased terminal step weights, the optimal trajectory provided by the MPC does not end at the reference, as shown in figure 3.19.

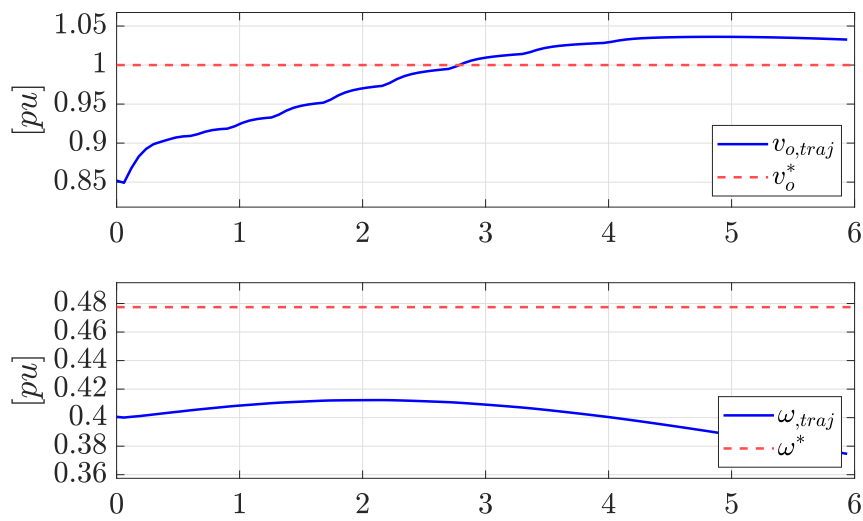


Figure 3.19: Predicted state trajectory with small terminal step weights.

On the other hand, with a large terminal step weight ($1e6$), on speed and output voltage, the state trajectory calculated at the same time step as in figure 3.19, can be seen to attain reference value at the final step, as shown in figure 3.20.

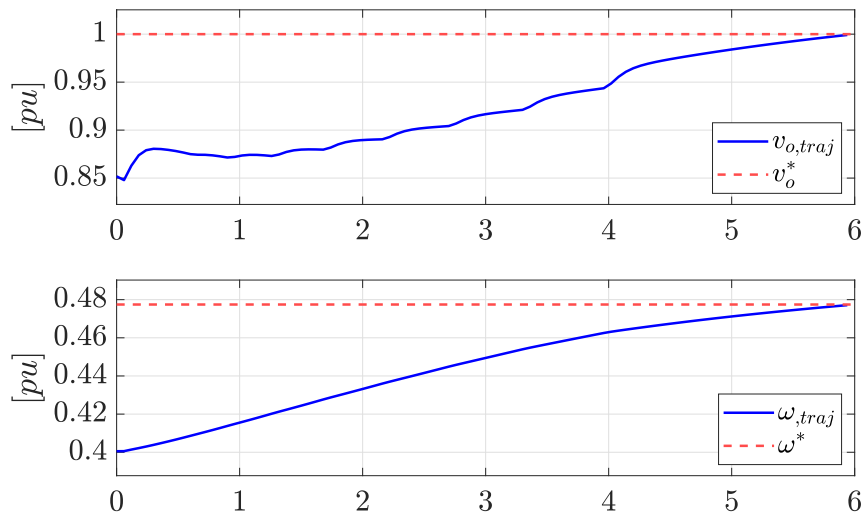


Figure 3.20: Predicted state trajectory with large terminal step weights.

As seen in the above, the calculated trajectory with increased terminal step weight ends up at the reference, contrary to in the case without increased terminal step weight. However, the actual system response was quite similar in both cases because the calculated trajectories became more similar in the steps following the shown examples. The difference was mainly observed in the short period following the disturbance, like was shown in figures 3.19 and 3.20. With increased terminal weights the MPC was a few iterations faster to change the speed direction towards the reference. All in all the weight setting did not seem to significantly improve performance but was included as a good practice.

3.2.6 Integral Action

Just like integral action is used in the SISO control system it is also an effective tool to improve reference tracking by the MPC [10]. Integral action is implemented as usual by expanding the state space. The MPC prediction model is in this case augmented by the three integral states (3.12), for terminal voltage, speed and output voltage.

$$\frac{d\xi}{dt} = (v_t^* - v_t) \quad (3.12a)$$

$$\frac{d\rho}{dt} = (\omega^* - \omega) \quad (3.12b)$$

$$\frac{d\gamma}{dt} = v_o^* - v_o \quad (3.12c)$$

Accordingly, the weighing matrix Q (3.7) is augmented by three elements along the diagonal. The weights [30, 20, 120] was found to be suitable for the integral states ξ , ρ and γ , respectively. The integral states results in a singular A matrix with three eigenvalues in origo. Nevertheless, the open loop step response is still well within bounds in terms of time step and prediction horizon length.

To demonstrate the effect, figure 3.21 shows an example of system behavior without integral action and figure 3.22 is with integral action.

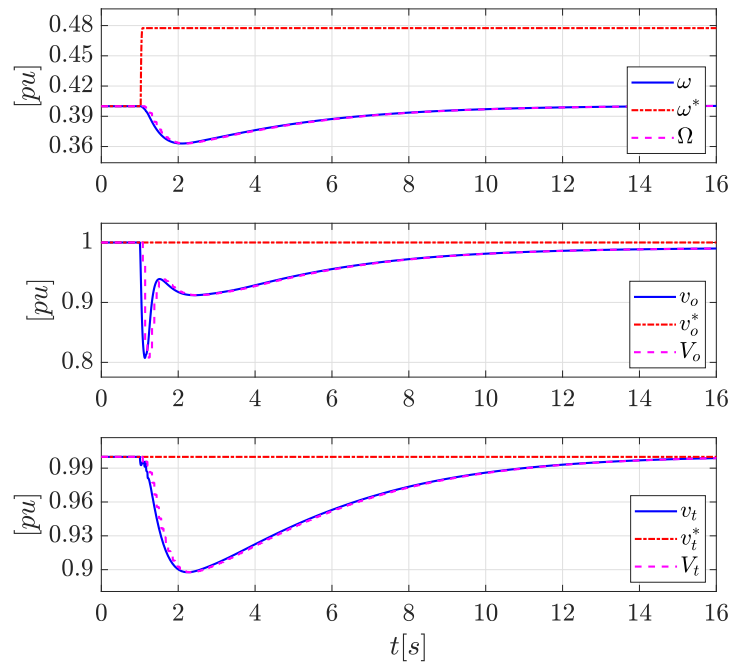


Figure 3.21: Adaptive MPC without integral action, response to load step.

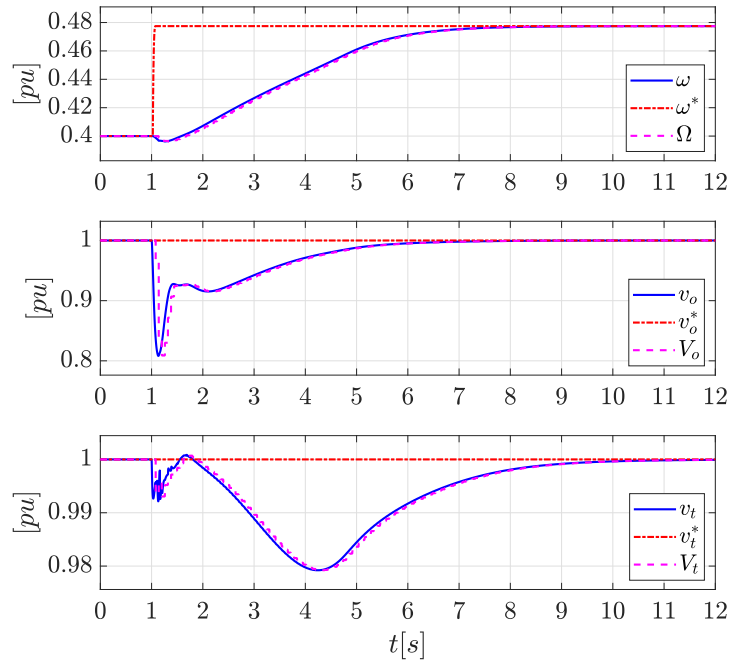


Figure 3.22: Adaptive MPC with integral action, response to load step.

3.2.7 Move Blocking

Locking control inputs over a pre-defined number of sampling time steps in the calculated trajectory is often a good idea for mainly two reasons. Firstly, it reduces the order of the QP problem. The potential for computational cost savings increases with the number of control inputs. Secondly, it tends to increase controller robustness [17]. In literature, there are numerous proposals for blocking schemes with varying complexity. The simplest approach is to define all blocking intervals equal in length. However, it is sensible to assume that the largest control input changes should occur at the beginning of the horizon rather than at the end. Therefore, an increasing block length scheme [10] might be a better idea, like shown in figure 3.23.

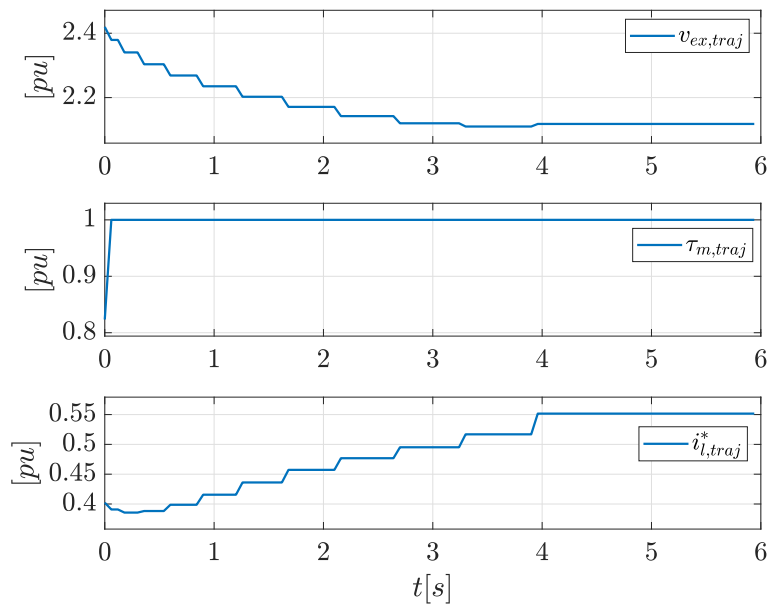


Figure 3.23: Calculated optimal control input trajectory using increasing blocking intervals.

The blocking intervals are made by incrementing the blocking length by one time step until the overall length is above some pre-defined portion of the prediction horizon length. Although there has not been performed a strictly controlled test of different blocking schemes in this project, the scheme presented here did seem to give a good control behavior.

3.2.8 Bounds

The solution of the QP problem (3.6) is restricted by hard bounds on the control inputs, while the duty cycle, generator voltage, output voltage and generator speed are restricted by soft bounds. Hard bounds on measured variables do not make sense (and is not allowed by the Matlab toolbox) because the measured variable can be moved outside this hard bound by external disturbances — making the initial condition infeasible.

Hard bounds (along with the equality constraint) define the feasible area, where the solver is allowed to return a solution. It is, therefore, important to ensure that the hard bounds are not conflicting. On the other hand, a solution may exist outside a soft bound [17]. In that case the cost of the solution would be quite high due to an increased slack variable, which typically has a large penalty. The slack variable

penalty ρ_ϵ can be considered as a measure of "hardness" of the soft bound.

The inner loop PI current controller has a duty cycle saturation limit $0 < d < 1$. The MPC prediction model does not behave well close to these limits. In the average model ideal case, where $v_s/v_o = 1 - d$, a unity duty cycle gives infinite gain. The prediction model includes parasitic elements and avoids the infinite gain, but the solution would still explode if crossing outside the limits. Therefore, a soft bound with a high penalty is set on this measured variable. In case the any stability issues occurs in the prediction model, the PI controller saturation can be shrunken so that a duty cycle of 0 or 1 is not fed back to the MPC. The soft and hard bounds defined in the MPC are shown in tables 3.4 and 3.5, respectively.

Table 3.4: MPC soft bounds

Measured variable	Lower	Upper
d	0.1	1
v_t	0	1.3
v_o	0	inf
ω	0	1

Table 3.5: MPC hard bounds

control input	Lower	Upper
v_{ex}	0	6
τ_m	0	1
i_l^*	0	3

No bounds are set on the control input rates.

3.2.9 Linear Prediction

As the plant model is highly nonlinear the linear mpc can easily have unpredictable behavior when the system is far away from the linearization point. In particular, the non-minimal-phase characteristic, caused by the boost circuit dynamics and cascaded control system is here considered in connection with the linear prediction model.

To gain some insight, the nonlinear explicit equation for output voltage (3.13) used in the prediction model is considered. The full prediction model on nonlinear form is given in appendix A.1.

$$\frac{dv_o}{dt} = \frac{\omega_b(i_l(k_{pi}(i_l - i_{l,2}^*) - \zeta + 1) - v_o/z_o)}{c} \quad (3.13)$$

The current reference $i_{l,2}^*$ is low pass filtered simply to avoid direct feedthrough from inputs to outputs in the prediction model². Furthermore, ζ is the inner loop current controller state. The controller (2.41c) is repeated here for convenience.

$$\begin{aligned} i_{l,2}^* &= \frac{i_l^* - i_{l,2}^*}{Tt} \\ \frac{d\zeta}{dt} &= k_{ii}(i_{l,2}^* - i_l) \\ \hat{d} &= k_{pi}(i_{l,2}^* - \hat{i}_l) + k_{ii}\zeta \end{aligned}$$

The prediction model state vector is (3.15).

$$\begin{bmatrix} i_d & i_q & i_f & v_f & \omega & i_l & v_o & \zeta & i_{l,2}^* \\ \xi & \rho & \gamma & & & & & & \end{bmatrix}^T \quad (3.15)$$

The 7th row in the jacobian A matrix (3.16) corresponds to the output voltage.

$$\begin{bmatrix} 0, & 0, & 0, & 0, & 0, \dots \\ \frac{\omega_b(I_l k_{pi} - \bar{\zeta} + k_{pi}(I_l - I_{l,2}^*) + 1)}{c}, & -\frac{\omega_b}{c} Z_o, & -\frac{\omega_b}{c} I_l, & -\frac{\omega_b}{c} I_l k_{pi}, & 0, \dots \\ 0, & 0, & & & \end{bmatrix} \quad (3.16)$$

Furthermore, the plant input vector including control inputs and disturbances is (3.17).

$$[v_{ex}, \tau_m, i_l^*, z_o, v_t^*, \omega^*, v_o^*]^T \quad (3.17)$$

The 7th row, corresponding to the output voltage, in the jacobian B matrix is (3.18).

$$\begin{bmatrix} 0 & 0 & 0 & \frac{\omega_b}{c} \frac{V_o}{Z_o^2} & 0 & 0 & 0 \end{bmatrix} \quad (3.18)$$

The linearized equation resulting from (3.15), (3.16), (3.17) and (3.18) simplifies to (3.19).

$$\frac{dv_o}{dt} = \frac{\omega_b (I_l k_{pi} - \bar{\zeta} + 1)}{c} \cdot i_l - \frac{\omega_b}{c} Z_o \cdot v_o - \frac{\omega_b}{c} I_l \cdot \zeta - \frac{\omega_b}{c} I_l k_{pi} \cdot i_{l,2}^* + \frac{\omega_b}{c} \frac{V_o}{Z_o^2} \cdot z_o \quad (3.19)$$

Surely, a large current i_l would increase the output voltage. However, as seen from (3.19) in isolation, both the MPC controlled current reference $i_{l,2}^*$ and ζ contributes to a voltage decrease. It is possible that this non-minimal-phase effect, in combination with an unsuitable linearization point, could result in a less than ideal current reference $i_{l,2}^*$ calculation.

²Such a direct feedthrough is not a valid configuration in the Matlab MPC toolbox.

3.2.10 Adaptive MPC

In order to improve accuracy and performance of the linear MPC the control system was modified to continuously update the linearization point based on plant measurements. The Simulink "Adaptive MPC" library function was used for this purpose. Naturally, the linear model must be discretized using the same time step as the MPC. The discretization was performed by calling the the "c2d" Matlab function every time step. Functions for the linear state space matrices was built using the Matlab symbolic toolbox. Figure 3.24 shows a principal sketch of the adaptive MPC operating point update.

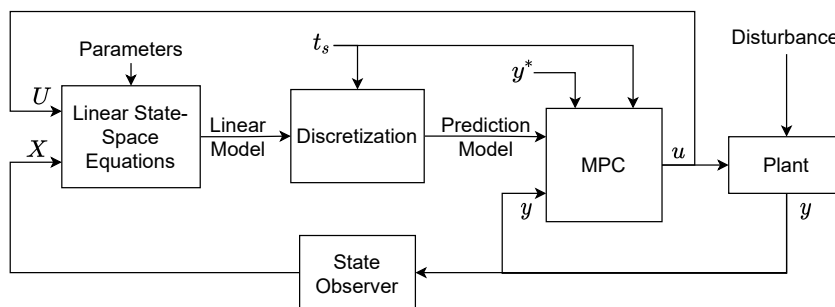


Figure 3.24: Adaptive linear MPC principal.

For every control move, the MPC will solve the quadratic problem using a linear plant model which is linearized around the current state measurement. In this manner the plant model will always be valid at the first prediction step. This offers a great improvement in accuracy over the conventional linear MPC. However, the calculated trajectory will in most cases be somewhat inaccurate especially during disturbances such as a change in load power.

A state observer is included in figures 3.16 and 3.24. However, a custom state observer has not been implemented in the actual simulation models. Instead, all states are simply measured in the plant and no observer is needed. In a real life implementation the state observer would be a crucial part of the design. The MPC, as opposed to the classical control system, is dependant on a good state estimate to be used in the initial time step of the optimal move calculation, and for linearization point update in the adaptive MPC case. A standard Luenberger observer block diagram can be found in appendix A.5.

In the following a few remarks is made on the numeric simulation stability in connection with the limited sampling rate of the MPC and model-linearizer ($t_s = 0.06s$). In the detailed Simulink model, including Simscape electrical circuit-simulation, the limited sampling rate may result in numerical issues because the model contains

diode rectifier ripple at a higher frequency than the MPC sampling rate. To clarify, only the MPC system runs at a limited sampling rate and not the electrical simulation. As mentioned in section 2.8, the boost converter switching dynamics is not included in the MPC model.

The numeric stability issues were solved by, firstly, reducing the rectifier snubber resistance as described in section 2.8, and secondly, by low pass filtering the plant measurements. It should be noted that the low pass filtering may easily compromise controller performance because of the increased phase delay. A filter time constant $0.02s$ was found to be suitable.

Figure 3.25 shows a plot of the (low pass filtered) duty cycle d with ripple from rectifier, and the resampled duty cycle D used for MPC feedback and model linearization. The resampling is done at a much lower sampling frequency than the rectifier ripple and will therefore contain aliasing ($t_s = 0.06$ sec).

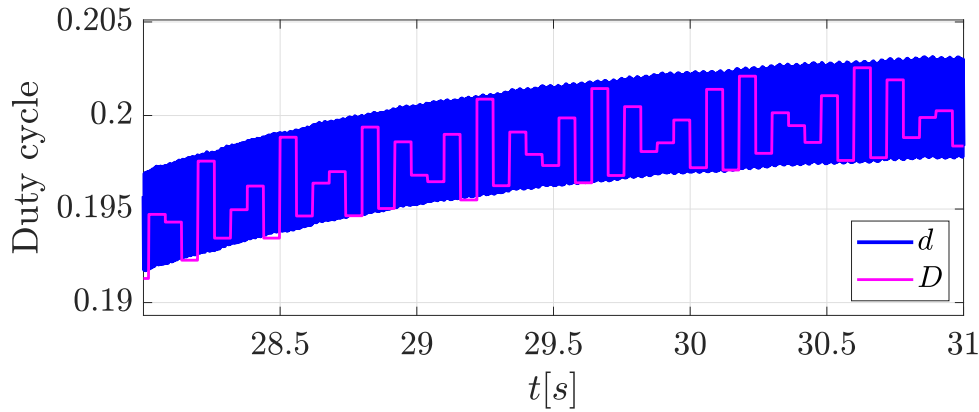


Figure 3.25: Plot of the filtered duty cycle d and the discretized (resampled) duty cycle D .

Naturally, the original high frequency rectifier noise is lost in the resampled signal. Therefore, the resampled signal will attain a lower frequency waveform depending on the sampling frequency and the noise frequency.

The example in figure 3.25 is from a stable and well-functioning simulation. The system was more easily affected by numeric instability when not including low pass filtering. All measurements were low pass filtered by the same time constant so that the added phase delay is similar between states in the MPC feedback.

To round of this chapter, an key aspect concerning the DC-link voltage control is given here. The MPC has two means of controlling the DC-link voltage $v_{o,dc}$. Firstly, by controlling the generator voltage v_t using the excitation voltage input

v_{ex} . Secondly, by controlling the DC-link voltage directly using the boost converter current reference i_l^* . A reduction in either v_{ex} or i_l^* will cause a reduction in the DC-link voltage.

Having completed the MPC implementation considerations, the remaining part of this chapter addresses the connection from the DC-link to the VSM.

3.2.11 Connecting VSM

With the AC peak voltage reference set to unity ($\hat{v}_{o,vsm}^* = 1$), the VSM would go into overmodulation if the DC-link voltage drops below unity. The modulation index is (3.20).

$$m = \frac{\hat{v}_{o,vsm}}{v_{dc}} \quad (3.20)$$

In the linear modulation area ($0 \leq m \leq 1$) the first harmonic AC voltage amplitude varies linearly with the modulation index m [20]. In the non-linear area the harmonic content increases with the amount of overmodulation. The linear range could be expanded to include some overmodulation through using third harmonic injection [2]. Operating the VSM in the overmodulation area is, however, not useful here because the DC voltage is fully controlled by the boost converter and MPC.

The VSM can be connected to the DC-link without any modifications. There is, however, a risk of VSM overmodulation if the VSM operates with a constant local voltage reference $\hat{v}_{o,vsm}^*$ while the MPC (or SISO control system) controls the DC-link voltage as a separate system without regard to the VSM. In that case, any reduction in DC-link voltage will result in overmodulation.

The MPC will act to track the speed reference, and reduce the DC-link voltage if a decrease in generator air-gap power is necessary in order to accelerate the generator. In that case, a VSM overmodulation would act against the MPC, resulting in an unstable system. The solution to this problem is simply to set the VSM voltage reference $\hat{v}_{o,vsm}^*$ equal to the DC-link voltage $v_{o,dc}$, and thus avoid overmodulation altogether.

In summary, the VSM voltage quality is synonymous with the DC-link voltage quality. Furthermore, the DC-link voltage quality is mainly depending on the spinning reserve present at any time — assuming the energy storage capability of the generator inertia is much larger than in the capacitor. If a high quality voltage supply is needed, then the speed reference must be controlled such that there is a large reserve present for each load situation, and the speed reference look-up table must be adjusted accordingly (see section 3.1.1). However, as implied earlier, a large speed reserve does not necessarily play well for the overall fuel consumption.

Having concluded the control chapter, the text chapter will put the SISO and

MPC control systems to the test in numeric simulations and compare their performances.

Chapter 4

Control Method Comparison

In this chapter, various simulation setups will be used to present the findings. The two main methods of control, namely the SISO control system and the MPC system, will be compared. Results from two separate simulation models for a diesel generator and boost converter is presented. Firstly, the model presented in section 2.7 has been used during troubleshooting, testing, and experimental tuning. This model will still be referred to as the project model, like previously in section 2.8. The project model was a natural intermediate step during testing because a linearized version of the same model is used as the MPC prediction model. Secondly, the MPC is implemented in a detailed Simulink circuit simulation model. This detailed model is coupled with the VSM model to form a full AC-DC-AC system. The latter is probably a better measure of MPC performance and robustness because it includes dynamics not included in the MPC prediction model.

4.1 Project Model Simulation

In this first section, the first of the aforementioned models is used to directly compare the SISO control system, the linear MPC and the adaptive MPC. The main purpose of this test is to show that the adaptive model predictive controller can both sustain stability and achieve reference tracking in a case where the SISO control system has limitations. A disturbance in the form of a load step from 0.1pu to 0.4pu is used to demonstrate each systems performance. The calculated load admittance Y_o is shown to demonstrate the load power demand. The speed reference ω^* is directly related to Y_o as it is (in all cases) controlled in line with the load impedance z_o , calculated from the DC-link voltage and current. In some of the figures the linearization point is plotted and is denoted by a capital symbol. This signal is constant in the linear MPC case, and varying with each corresponding signal in the adaptive MPC case.

4.1.1 SISO Control

In figure 4.1 the SISO control system is used. The SISO controllers all operate as completely separate systems with constant local references. Consequently, as the output voltage is corrected, the electrical power surpasses the mechanical power capability. The speed corresponding to 0.1pu load ($\omega^* = 0.4pu$) is too low for the SISO control system to sustain stability during the load increase. The electrical power increases to a little bit above 0.4pu while the maximum generator power capability, given by the current speed at the step instant, is 0.4pu. The power keeps flowing and the voltage is sustained in several seconds because of the generator inertia.

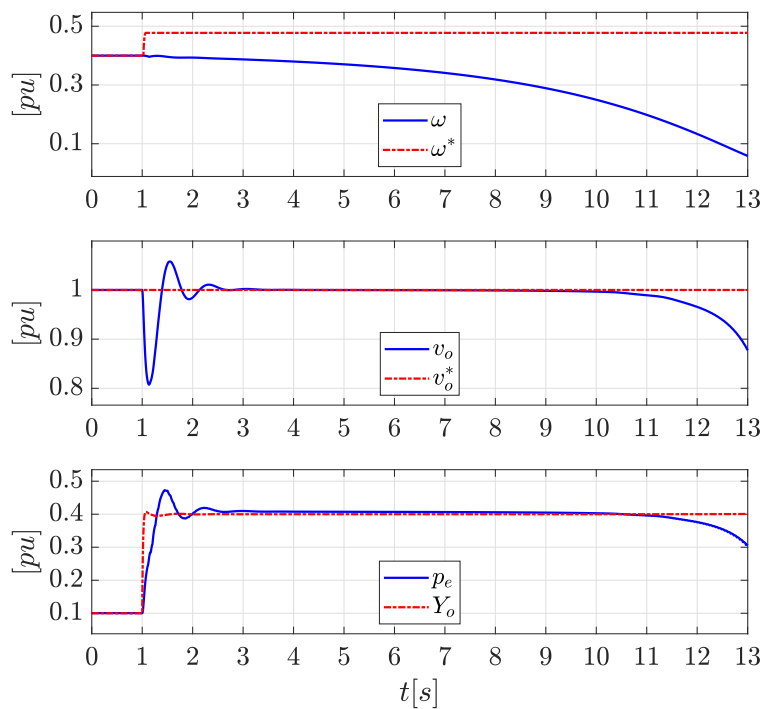


Figure 4.1: SISO control response during load step.

4.1.2 Linear MPC

The same test is performed using the linear MPC (with integral action) in figure 4.2. The linear MPC is stable in this case, but it does not behave well away from the linearization point and is not able to track the reference. Note that the linear MPC has the exact same tuning as the adaptive MPC. The linear MPC might behave

somewhat better with another tuning, and a linearization point better suited for this specific test. It would, however, not be functioning in all operating ranges, as seen here.

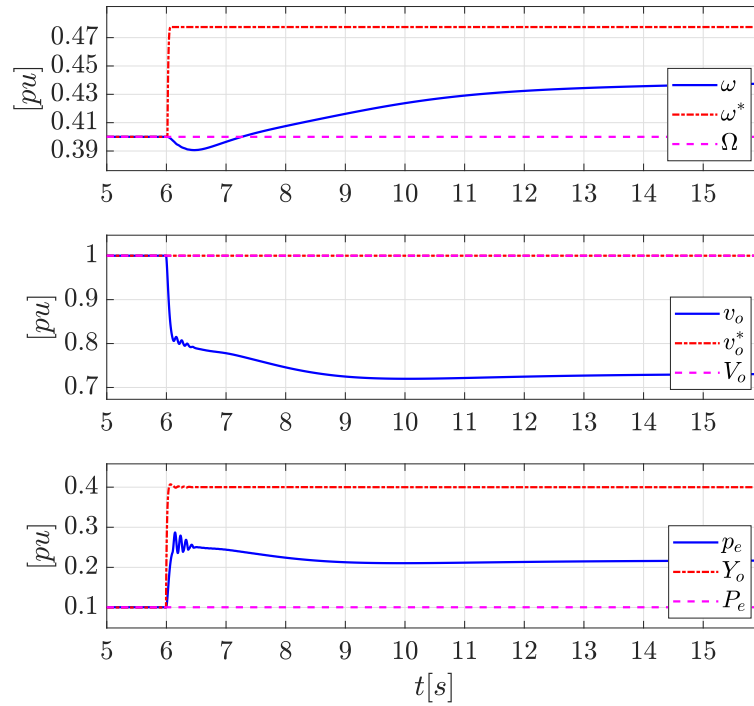


Figure 4.2: Linear MPC response during load step away from operating point.

4.1.3 Adaptive MPC

As shown in figure 4.3, the adaptive MPC is able to control the system and track the reference.

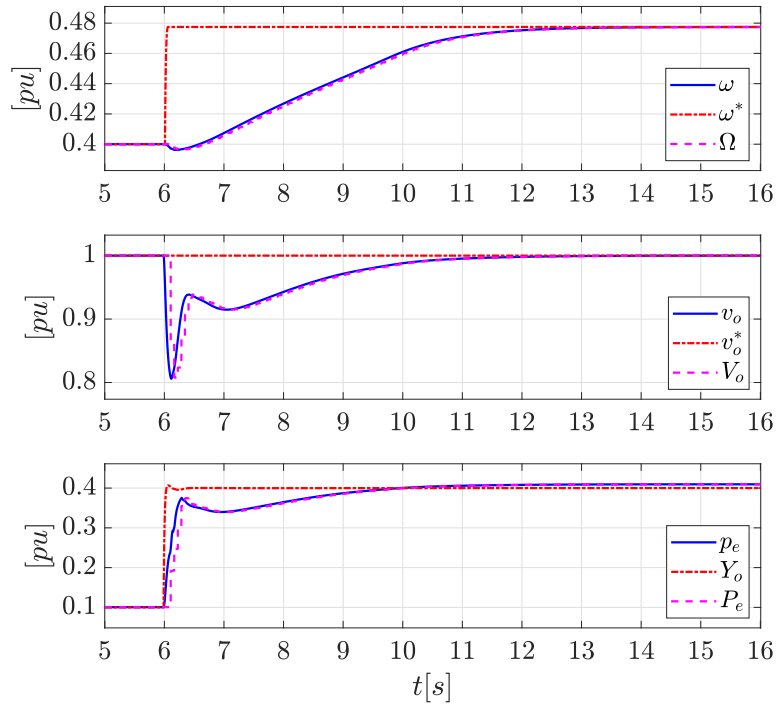


Figure 4.3: Adaptive MPC response during load step.

With the linearization-point being updated every controller instant, the prediction becomes much more accurate, thus resulting in a better controller performance.

4.2 AC-DC-AC Detailed Model Simulation

Moving now on to the detailed circuit simulation where the complete electrical model is made using the Simscape Specialized Power Systems library. The simulation consists of a constant speed diesel generator (CSDG), two resistive loads and a variable speed diesel generator (VSDG) grid-connected using the AC-DC-AC converter with VSM, like illustrated in figure 4.4 for the MPC case (See figure 3.1 in chapter 3 for the SISO control system hierarchy).

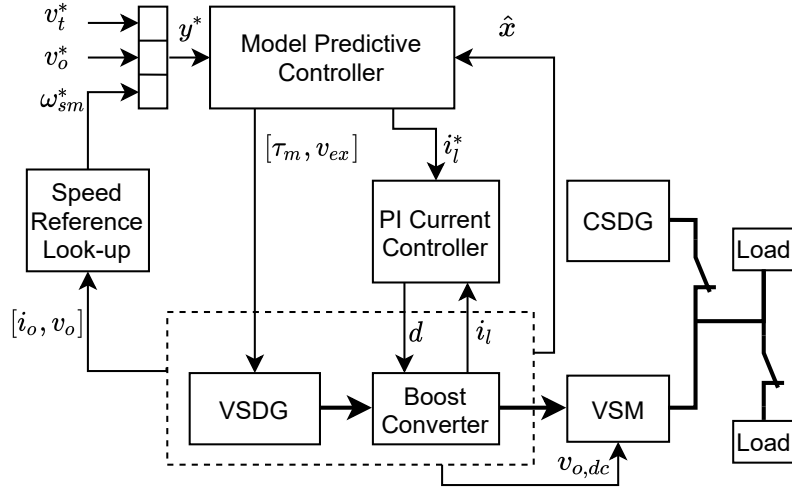


Figure 4.4: Simulation setup principle diagram when using MPC.

The only modification done to the VSM control system, beyond how it was presented in the specialization project, is the voltage magnitude reference $\hat{v}_{o,vsm}^*$, which is set to follow the DC-link voltage $v_{o,dc}$ to avoid VSM overmodulation during a DC-link voltage drop, as discussed in section 3.2.11.

Some parameters used in the power system simulation is provided in table 4.1 and 4.2. The same base and rated values are used for the VSDG, CSDG and VSM.

Table 4.1: Power system rated values for VSDG, CSDG and VSM .

Symbol	Expression	Description
V_{ph}	398.37	Rated phase RMS voltage [V]
I_n	740.54	Rated line current for[A]
S_b	885.0	Rated apparent power [kVA]
f_b	60	Rated frequency [Hz]

Table 4.2: Active power references used in the simulation.

Symbol	Expression	Description
p_{vsm}^*	0.4	Active power reference VSM [pu]
p_{vsdg}^*	0.2(case 1), 0.28(case 2)	Active power reference VSDG [pu]

Any model constants or parameters not provided here can be found in appendix

A.8.

To demonstrate the AC-DC-AC converter functionality a sequence of three disturbance events (a,b,c) occurs in the simulation. The load power is first equally divided between the VSDG and the CSDG. Then, (a) the load is decreased before, (b) the CSDG goes off-line. The VSDG then operates islanded while, (c) the load is again increased to the same level as in the beginning.

The SISO control system is used to control the VSDG and boost converter during the simulation in figure 4.5. The AC-DC-AC converter is subjected to a 0.4pu load constantly connected, a load variation of 0.2pu and an islanding event. The active power reference on the VSM and CSDG is decisive for how the load is distributed. The CSDG active power reference is in all cases set equal to the load variation while the VSM active power reference is set equal to the load constantly connected.

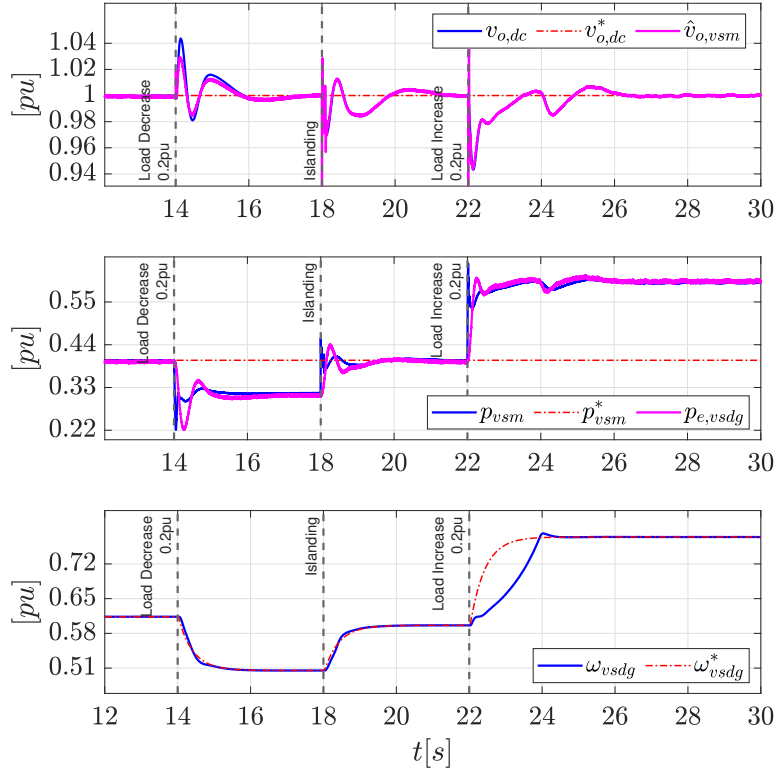


Figure 4.5: AC-DC-AC model simulation using SISO control system. Islanding event and 0.2pu load variation.

Since the load increase occurs during islanded operation this amounts to the largest disturbance. As discussed earlier, the SISO control system can retain control when the load increase is not too large. An additional voltage drop can be seen at the point where the speed reaches its reference, and the mechanical torque is decreased.

Figure 4.6 shows the same simulation setup using the adaptive MPC controller.

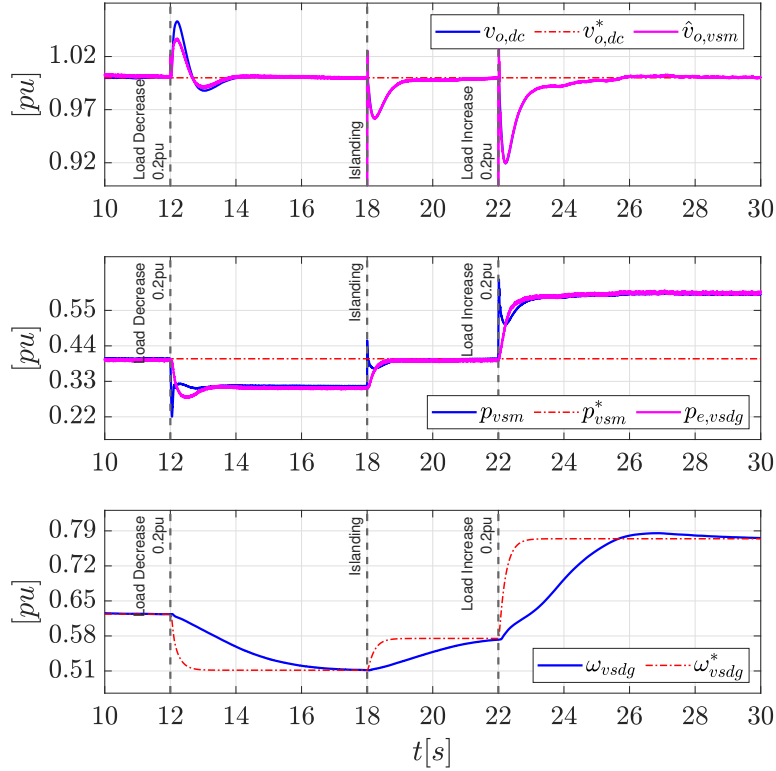


Figure 4.6: AC-DC-AC model simulation using adaptive MPC. Islanding event and 0.2pu load variation.

In comparison to the SISO control system speed control, the MPC speed control might seem slow. Because the speed control is only a secondary objective, necessary to maintain voltage, the penalty setting for speed deviance in the MPC cost function is lower compared to the voltage deviance penalty. As for the SISO control system, having a fast speed controller (and slow electrical controllers) might contribute to a better outcome during the large load increase since maximal torque is applied immediately before the electrical power reaches its maximal value, see figure 4.5.

There is also a notable difference in the size of the voltage drop preceding the load increase. This may be seen in connection with the response time of the two control systems. While the SISO controller responds immediately, the MPC is limited by the sampling time of 0.06 seconds. Although 0.06 seconds might not sound as much, the voltage drop will increase with the response time because the inner loop current controller acts to limit the current until its reference is updated by the MPC. The phenomena can be compared to the cascaded PI controller case discussed in section 3.1.4. Moreover, some MPC prediction error is expected because of the linear prediction. Any prediction error may degrade the MPCs ability to operate at the plants physical limit.

When considering the 0.2 pu load increase case, the advantage of the MPC is not obvious. The SISO system will maintain stability given that the system operates well within the physical limits of the plant. A larger load step will bring the system closer to this limit, and the advantage of the MPC can be demonstrated more clearly. The SISO control system response in a case with a larger load increase is shown in figure 4.7. In this case the system behavior is normal until it becomes unstable after the load is increased (during islanded operation).

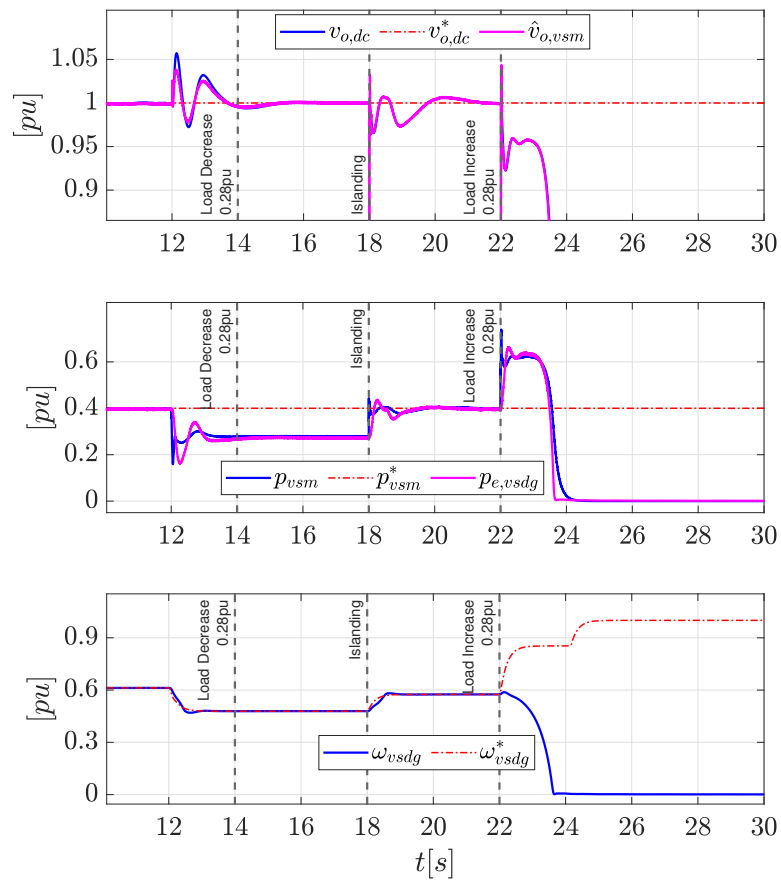


Figure 4.7: AC-DC-AC model simulation using SISO control system. Islanding event and 0.28pu load variation.

The control inputs corresponding to figure 4.7 is shown in figure 4.8.

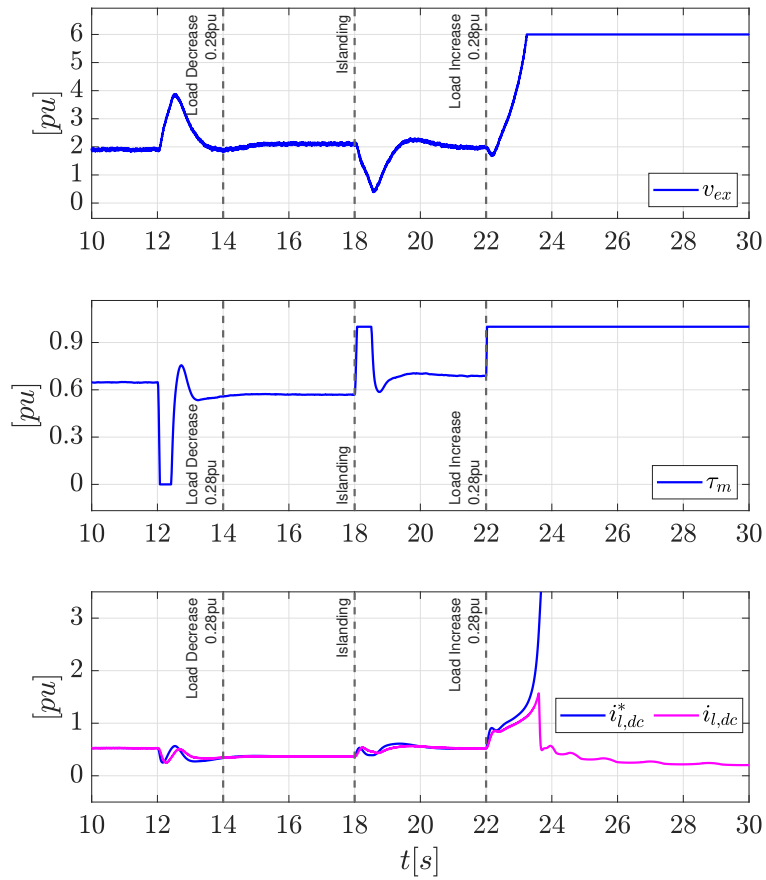


Figure 4.8: AC-DC-AC model using SISO control system, control inputs. Islanding event and 0.28pu load variation.

While the SISO control system has issues, the adaptive MPC in figure 4.9 behaves as usual — limiting the output voltage to allow for a speed increase. In any case, the MPC will avoid stalling the engine. If the speed reference for some reason should end up at a too low value, the output voltage will, correspondingly, be decreased below reference while the generator speed will exceed the reference, all depending on the MPC cost function tuning.

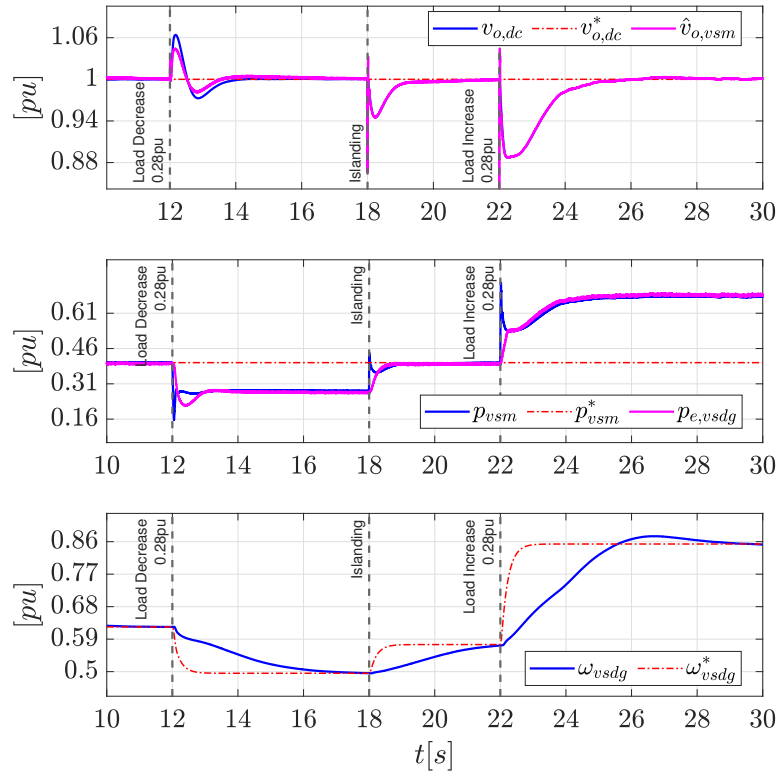


Figure 4.9: AC-DC-AC model simulation using adaptive MPC. Islanding event and 0.28pu load variation.

The voltage drop is substantial in this case because the initial speed reference is relatively low. For systems with voltage sensitive equipment such a voltage drop may not be within the grid side tolerances. In that case, the speed reference lookup must be adjusted to include a larger spinning reserve. The control inputs corresponding to figure 4.9 is shown in figure 4.10.

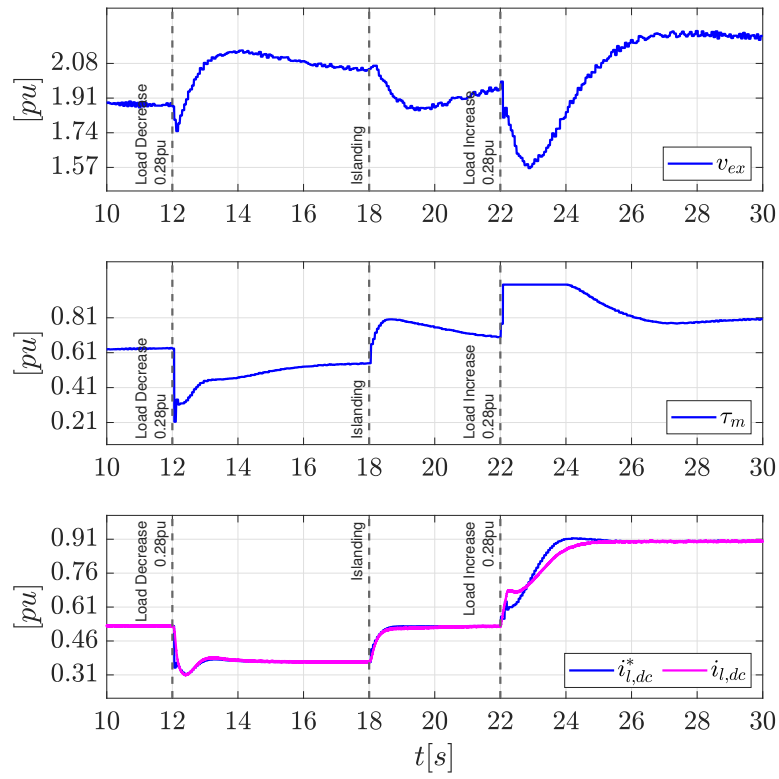


Figure 4.10: AC-DC-AC model using adaptive MPC, control inputs. Islanding event and 0.28pu load variation.

The cost function value for every controller time step, for the 0.2pu load case, is shown in figure 4.11.

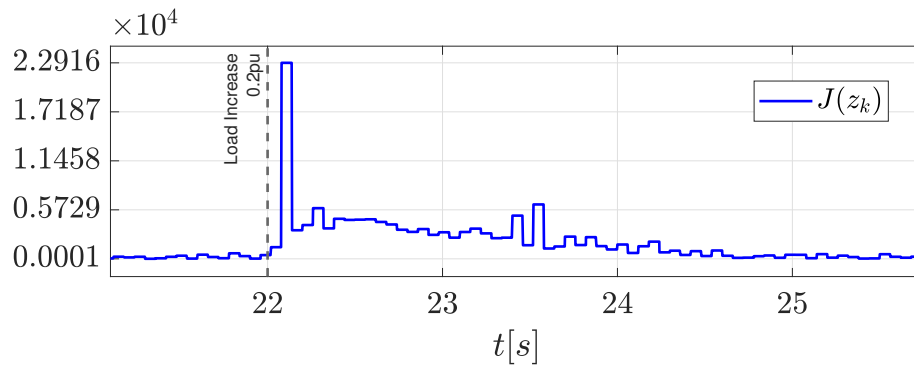


Figure 4.11: MPC cost function value for the 0.2pu load increase case.

The cost function value $J(z_k)$ spikes after the disturbance event because of the large step change in control inputs, penalized by $R_{\Delta u}$. In the preceding iteration, the control input step change is lower, and the cost value is therefore decreased. The cost value decreases as the measurements get closer to their respective references. The delay in controller response by one time step $t_s = 0.06$ can be seen clearly.

In summary, this chapter has demonstrated the functionality of both control systems, as well as the advantages of the adaptive MPC over the SISO control system. The next chapter will give some closing remarks on the project.

Chapter 5

Conclusion and Further Work

This final chapter will give a brief summary of the work presented in this thesis and give a few closing remarks. Some thoughts around the possibilities for future work is given in the end.

5.1 Conclusion

Based on synchronous machine and power electronics modelling theory, a model is made for this project, consisting of a synchronous generator, rectifier and a DC/DC boost converter. The model is shown to match reasonably well with a more detailed model made using Simulink library blocks. A linearized version of the project model has been used to empower a linear model predictive controller which is made to function better on the nonlinear system by using an adaptive method. The Matlab MPC toolbox has been used in the implementation.

A classical SISO control system for the diesel generator excitation and speed, along with a cascaded control system for the boost converter, has been implemented. The control design has been validated for steady state stability using eigenvalue and frequency response considerations.

A virtual synchronous machine was included in the simulation to form a full back-to-back AC/DC/AC voltage source converter connected to a grid consisting of a constant speed generator. Both the MPC and the classical control design are shown to function in the full system simulation. It is also shown that the MPC can provide a stable operation during larger load surges where the classical control design becomes unstable, when operating at a reduced generator speed.

To enable fuel optimization using variable generator speed, an approach using a look-up table to continuously update the speed reference, in line with a varying load

situation, is proposed. The look-up table should be modified in accordance with each system implementation to respect the systems voltage quality tolerances.

The results indicates that an MPC implementation may allow for a speed control more in line with the real-time load situation, assuming some reduction in voltage during load surges can be allowed. In conclusion, there may be a potential for overall fuel savings, in low load situations, by using an MPC to enable a lower speed operation.

5.2 Further Work

There are multiple areas for improvement in the control design. A few interesting topics not included in the thesis is listed in the following.

- In order to implement the MPC in a physical system, a state observer must be made. Noise modelling might be relevant in this context in order provide a better estimate when the measurements are subjected to switching noise.
- The adaptive method implemented in this project enabled the linear MPC to control the system reasonably well. It would, however, be interesting to compare its performance to a non-linear MPC.
- This project has used a boost converter to actively control the DC voltage. Future work could look into an MPC design using only an uncontrolled diode rectifier in the DC-link, or an active rectifier instead of a boost converter. In that context, it would be interesting to compare an MPC design using an active converter versus an MPC design using only a passive rectifier.
- The prediction model used in this thesis does contain both fast and slow dynamics, which may not be favorable when considering the computational cost in a real-time implementation. Furthermore, the non-minimal-phase characteristic was shown, in section 3.1.4, to have a tendency to amplify the voltage drop during a fast load disturbance — especially if the inner loop controller is tuned for a tight current reference tracking. Based on this, it might be relevant to consider using two cascaded MPC controllers, where the outer loop MPC provides the output voltage reference, while the inner loop MPC controls the active converter. The inner loop MPC could for example use the uncontrolled boost converter circuit model for prediction because it would have a much shorter prediction horizon and sampling time than the outer loop MPC — and thus comply with the finite step response criteria(see section 3.2.1).
- In this project, fuel saving has been assumed to be achieved through speed reduction, and a linear speed reference look-up from load impedance has been used. Further work could go for a more detailed approach with respect to the

speed reference control, so that the speed would be controlled in line with the optimal for fuel consumption. This can be done either based on a detailed engine model or a look-up table made from manufacturer data.

Appendix A

Appendix

A.1 MPC Prediction Model nonlinear form

The prediction model is presented here on nonlinear form. The same algebraic expressions as in section 2.7 are used to simplify the explicit equations A.2. All variables are here in the low voltage side per unit system so that no per unit conversions are included in the equations.

$$d = k_{pi} (i_{l,2}^* - i_l) + \zeta \quad (\text{A.1a})$$

$$V = (1 - d) v_o + \frac{3i_l \omega l_{boost}}{2\pi} \quad (\text{A.1b})$$

$$\frac{di_d}{dt} = \frac{\omega_b(l_f V i_d - l_{ad} i_l v_f + l_{ad} i_f i_l r_f + l_f i_d i_l r_s - l_f l_q i_l i_q \omega)}{i_l(l_{ad}^2 - l_d l_f)} \quad (\text{A.2a})$$

$$\frac{di_q}{dt} = \frac{\omega_b(l_{ad} i_f i_l \omega - V i_q - i_l i_q r_s - l_d i_d i_l \omega)}{l_q i_l} \quad (\text{A.2b})$$

$$\frac{di_f}{dt} = \frac{\omega_b(l_{ad} V i_d - l_d i_l v_f + l_d i_f i_l r_f + l_{ad} i_d i_l r_s - l_{ad} l_q i_l i_q \omega)}{i_l(l_{ad}^2 - l_d l_f)} \quad (\text{A.2c})$$

$$\frac{dv_f}{dt} = \frac{1}{T_{ex}} \left(\frac{r_f v_{ex}}{l_{ad}} - v_f \right) \quad (\text{A.2d})$$

$$\frac{d\omega}{dt} = \frac{\tau_m \omega - V i_l}{H} \quad (\text{A.2e})$$

$$\frac{di_l}{dt} = \frac{\omega_b}{l_{boost}} \left(\sqrt{\left(\frac{V i_d}{i_l} \right)^2 + \left(\frac{V i_q}{i_l} \right)^2} - i_l r_l + v_o(d-1) \right) - \frac{3\omega_b i_l \omega}{2\pi} \quad (\text{A.2f})$$

$$\frac{dv_o}{dt} = \frac{\omega_b}{c} \left(i_l(1-d) - \frac{v_o}{z_o} \right) \quad (\text{A.2g})$$

$$\frac{d\zeta}{dt} = k_{i,i}(i_{l,2}^* - i_l) \quad (\text{A.2h})$$

$$\frac{di_{l,2}^*}{dt} = \frac{i_l^* - i_{l,2}^*}{T_t} \quad (\text{A.2i})$$

$$\frac{d\xi}{dt} = v_t^* - \sqrt{\left(\frac{V i_d}{i_l} \right)^2 + \left(\frac{V i_q}{i_l} \right)^2} \quad (\text{A.2j})$$

$$\frac{d\rho}{dt} = \omega^* - \omega \quad (\text{A.2k})$$

$$\frac{d\gamma}{dt} = v_o^* - v_o \quad (\text{A.2l})$$

A.2 Title and Abstract for Synopsis

Model Predictive Control of a Variable Speed Back-up Diesel Generator Interfaced to a AC Ship Power System as a Virtual Synchronous Machine

Authors — Jon Are Suul, Magnus Jenssen

Abstract — This paper will present an adaptive model predictive controller (MPC) for a variable speed diesel generator operated as a back-up energy source in an AC ship power system. The variable-speed generator system consists of a diesel motor driving a synchronous machine with a diode rectifier and a boost converter as the interface to the dc-link of the grid-side voltage source converter (VSC). The grid-side VSC is operated as a Virtual Synchronous Machine (VSM) for ensuring flexibility in operation and capability for supported islanded operation of the ship power system at low load. The MPC strategy is designed for controlling the diesel generator torque and the excitation system, and for regulating the dc-link voltage by providing a current reference for the boost converter. Adaptive operation of the MPC implementation is introduced by using linearizing corresponding to the conditions at each time-step. Simulation results demonstrate how the proposed implementation can ensure a more robust performance and a larger range of stability in response to large load variations in the ac grid than a conventional approach based on independent PI-controllers.

Index Terms — Diode Rectifier with Boost Converter, Model Predictive Control, Ship Power System, Variable Speed Diesel Generator, Virtual Synchronous Machine

A.3 Park transform

The park transform can be done in two steps, first A.3, then A.4.

$$\begin{bmatrix} x_\alpha \\ x_\beta \\ x_0 \end{bmatrix} = \frac{2}{3} \begin{bmatrix} 1 & -\frac{1}{2} & -\frac{1}{2} \\ 0 & \frac{\sqrt{3}}{2} & -\frac{\sqrt{3}}{2} \\ \frac{1}{2} & \frac{1}{2} & \frac{1}{2} \end{bmatrix} \begin{bmatrix} x_a \\ x_b \\ x_c \end{bmatrix} \quad (\text{A.3})$$

$$\begin{bmatrix} x_d \\ x_q \end{bmatrix} = \begin{bmatrix} \cos(\theta) & \sin(\theta) \\ -\sin(\theta) & \cos(\theta) \end{bmatrix} \begin{bmatrix} x_\alpha \\ x_\beta \end{bmatrix} \quad (\text{A.4})$$

A.4 Synchronous Machine Parameter Conversion

Expressions for parameter conversion from fundamental to standard parameters is given in [13] as,

Table A.1: Standard Parameter Expressions from [13].

Standard Parameter	Classical Expression	Accurate Expression
T'_{d0}	T_1	$T_1 + T_2$
T'_d	T_4	$T_4 + T_5$
T''_{d0}	T_3	$T_3[T_1/(T_1 + T_2)]$
T''_d	T_6	$T_6[T_4/(T_4 + T_5)]$
x'_d	$x_d(T_4/T_1)$	$x_d(T_4 + T_5)/(T_1 + T_2)$
x''_d	$x_d(T_4T_6)/(T_1T_3)$	$x_d(T_4T_6)/(T_1T_3)$

where,

$$\begin{aligned} T_1 &= \frac{x_{ad} + x_f}{r_f} & T_2 &= \frac{x_{ad} + x_D}{r_D} \\ T_3 &= \frac{1}{r_D} \left(x_D + \frac{x_{ad}x_f}{x_{ad} + x_f} \right) & T_4 &= \frac{1}{r_f} \left(x_f + \frac{x_{ad}x_{s\sigma}}{x_{ad} + x_{s\sigma}} \right) \\ T_5 &= \frac{1}{r_D} \left(x_D + \frac{x_{ad}x_{s\sigma}}{x_{ad} + x_{s\sigma}} \right) & T_6 &= \frac{1}{r_D} \left(x_D + \frac{x_{ad}x_{s\sigma}x_f}{x_{ad}x_{s\sigma} + x_{ad}x_f + x_fx_{s\sigma}} \right) \end{aligned}$$

These expressions can be solved for the fundamental parameters so that the parameters given by the manufacturer can be input to the equivalent circuit model. By

looking at the equivalent circuits we can see assume (A.6).

$$x_{ad} = x_d - x_{l\sigma} \quad (\text{A.6a})$$

$$x_{aq} = x_q - x_{l\sigma} \quad (\text{A.6b})$$

Since the exact expressions becomes highly complex only the solution corresponding to the classical expressions are presented here. The symbolic toolbox provided by Matlab is used to derive the expressions A.7.

$$x_D = -\frac{(x_{ad}x_d'' - x_d x_{l\sigma} + x_d'' x_{l\sigma})(x_{ad}x_d' + x_d' x_{l\sigma} - T_{do}' x_{ad} x_d - 2T_{do}' x_d x_{l\sigma})}{x_d(x_{ad} + x_{l\sigma})(T_{do}' x_d - x_d' + T_{do}' x_d'')} \quad (\text{A.7a})$$

$$x_f = -\frac{x_{ad}(x_{ad}x_d' + x_d' x_{l\sigma} - T_{do}' x_{ad} x_d - 2T_{do}' x_d x_{l\sigma})}{(x_d' - 2T_{do}' x_d)(x_{ad} + x_{l\sigma})} \quad (\text{A.7b})$$

$$r_D = -\frac{(x_{ad}x_d' + x_d' x_{l\sigma} - T_{do}' x_{ad} x_d - 2T_{do}' x_d x_{l\sigma})^2}{T_{do}' T_{do}'' x_d (x_{ad} + x_{l\sigma})(T_{do}' x_d - x_d' + T_{do}' x_d'')} \quad (\text{A.7c})$$

$$r_f = -\frac{x_{ad}^2 x_d}{(x_d' - 2T_{do}' x_d)(x_{ad} + x_{l\sigma})} \quad (\text{A.7d})$$

$$x_Q = -\frac{x_{aq}(x_{l\sigma} - x_q'')}{x_{aq} + x_{l\sigma} - x_q''} \quad (\text{A.7e})$$

$$r_Q = \frac{x_{aq}^2}{T_{qo}''(x_{aq} + x_{l\sigma} - x_q'')} \quad (\text{A.7f})$$

A.5 Luenberger Observer

The state observer estimates the full state vector using a plant model and a limited number of measurements. The observer corrects the estimation error to zero through a feedback loop. The necessary output measurements to ensure that all states are observable can be found theoretically by calculating the observability matrix for different measurement vectors — Some trial and error is often necessary to determine the necessary measurements for observability. Figure A.1 shows the block diagram of a Luenberger observer.

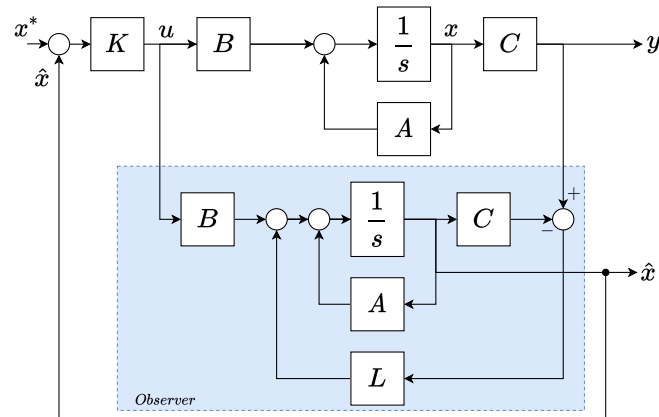


Figure A.1: A Luenberger observer in a closed loop plant.

One of the challenges is to set the observer gain matrix L . It could be set by pole placements for observer. The poles of the total closed loop system is the combined observer poles and closed loop state feedback poles like shown in (A.8) [6].

$$A_c = \begin{bmatrix} A - BK & BK \\ 0 & A - CL \end{bmatrix} \quad (\text{A.8})$$

The observer poles in $A - CL$ must be faster than the fastest closed loop poles in $A - BK$.

Another celebrated state estimation technique is the Kalman filter. This technique is useful for systems with noisy measurements. In Kalman filter design, measurements error and estimator model error is handled statistically, using Gaussian distributions, such that the trustworthiness of measurements and prediction is incorporated in the estimation.

A.6 Tuning-Variable Pole-Sweeps

The speed is at 0.7pu and the load is at 0.5pu for all pole sweeps. The tuning parameter setup during the sweeps is given in table A.2.

Table A.2: Tuning Parameter Setup

Symbol	Value	Description
$k_{p,i}$	0.8	Boost current controller proportional gain
$k_{i,i}$	2.0	Boost current controller integral gain
$k_{p,o}$	1.7	Boost voltage controller proportional gain
$k_{i,o}$	10	Boost voltage controller integral gain
$k_{p,\omega}$	25	Speed controller proportional gain
$k_{i,\omega}$	100	Speed controller integral gain
$k_{p,ex}$	9.0	Excitation controller proportional gain
$k_{i,ex}$	9.0	Excitation controller integral gain

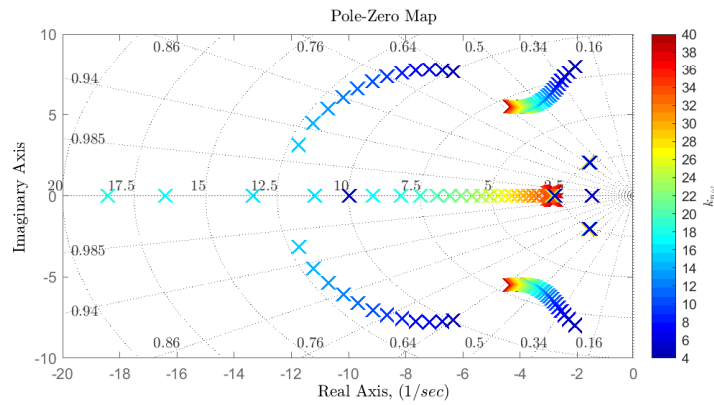


Figure A.2: Zoomed pole plot with speed controller proportional gain $k_{p,\omega}$ sweep.

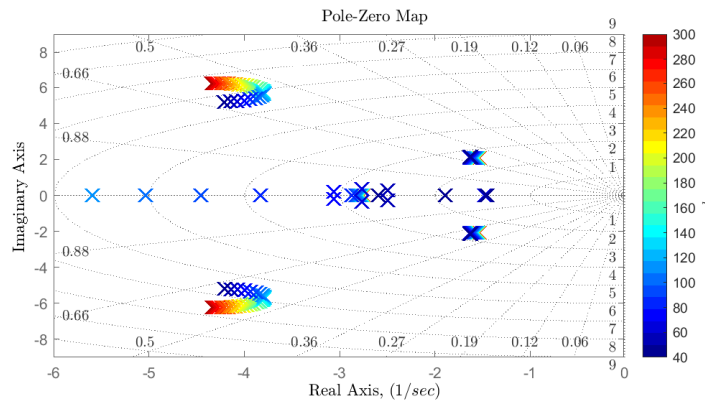


Figure A.3: Zoomed pole plot with speed controller integral gain $k_{i,\omega}$ sweep.

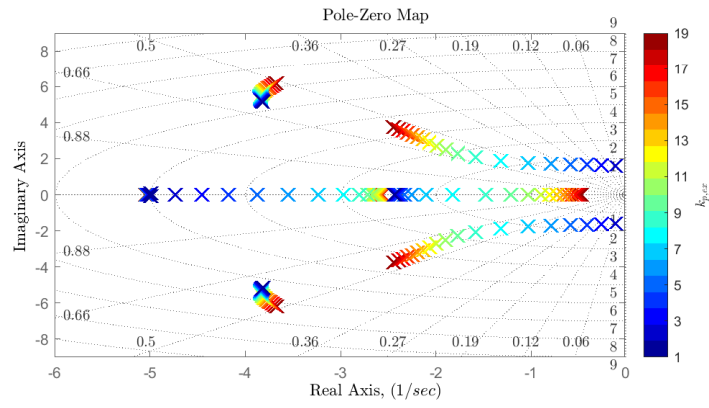


Figure A.4: Zoomed pole plot with excitation controller proportional gain $k_{p,ex}$ sweep.

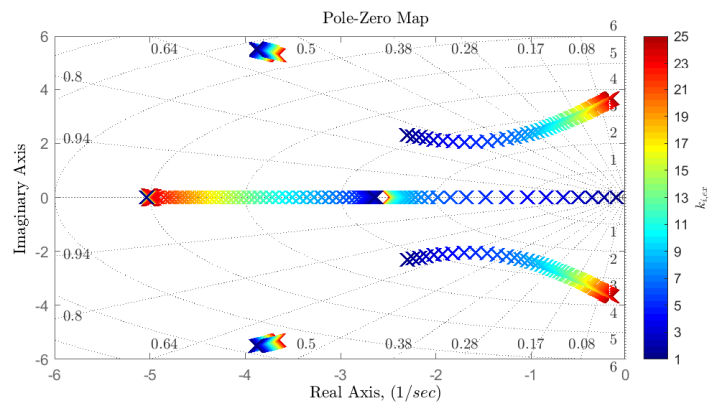


Figure A.5: Zoomed pole plot with excitation controller integral gain $k_{i,ex}$ sweep.

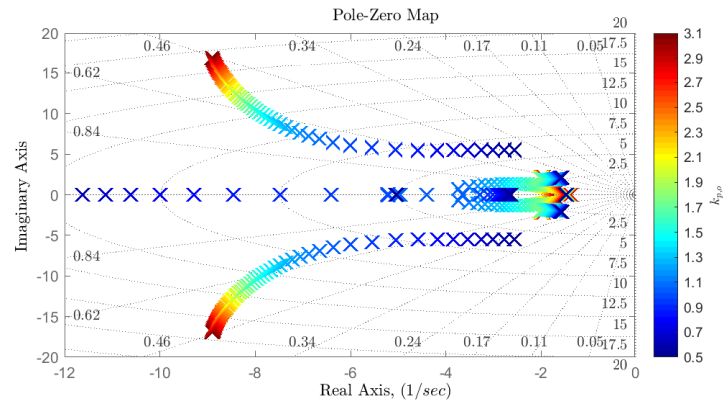


Figure A.6: Zoomed pole plot with outer loop voltage controller proportional gain $k_{p,o}$ sweep.

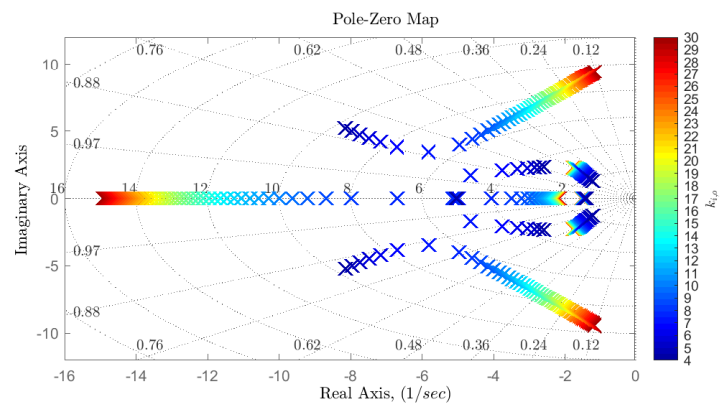


Figure A.7: Zoomed pole plot with outer loop voltage controller integral gain $k_{i,o}$ sweep.

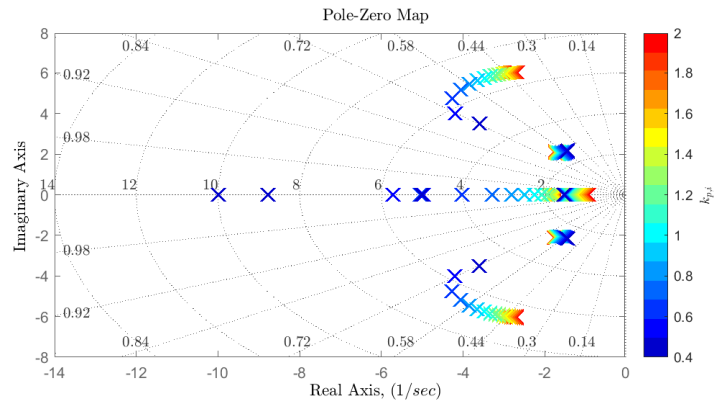


Figure A.8: Zoomed pole plot with inner loop current controller proportional gain $k_{p,i}$ sweep.

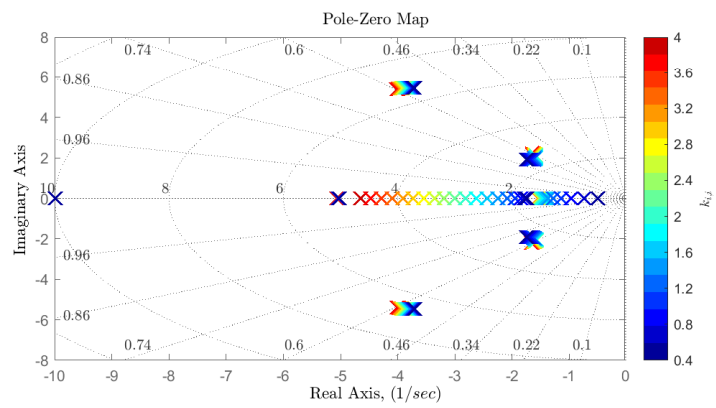


Figure A.9: Zoomed pole plot with inner loop current controller integral gain $k_{i,i}$ sweep.

Table A.3: Generator and boost converter closed loop system modes.

<i>nr.</i>	$1.0e + 03 \times$
1	$-4.0706 + 0.0000i$
2	$-1.9424 + 0.0000i$
3	$-0.2872 + 0.0000i$
4	$-0.0292 + 0.0000i$
5	$-0.0042 + 0.0052i$
6	$-0.0042 - 0.0052i$
7	$-0.0014 + 0.0018i$
8	$-0.0014 - 0.0018i$
9	$-0.0016 + 0.0000i$
10	$-0.0033 + 0.0000i$
11	$-0.0051 + 0.0000i$
12	$-0.0100 + 0.0000i$

A.7 Participation Matrix

Like shown in chapter 12 in [13], the participation matrix P can be found from (A.9,A.9) [13].

$$\mathbf{P} = [\mathbf{P}_1 \quad \mathbf{P}_2 \quad \cdots \quad \mathbf{P}_n] \quad (\text{A.9})$$

$$\mathbf{p}_i = \begin{bmatrix} p_{1i} \\ p_{2i} \\ \vdots \\ p_{ni} \end{bmatrix} = \begin{bmatrix} v_{1i}u_{i1} \\ v_{2i}u_{i2} \\ \vdots \\ v_{ni}u_{in} \end{bmatrix} \quad (\text{A.10})$$

The participation matrix corresponding to the modes A.3 is shown in (A.11).

<i>nr.</i>	i_d	i_q	i_f	v_f	ω	i_l	v_o	ζ	$i_{l,2}^*$	γ	ξ	ρ
1	0.8607	0.0116	0.0419	0.0000	0.0001	0.1087	0.0001	0.0001	0.0000	0.0000	0.0000	0.0000
2	0.0179	0.1462	0.0687	0.0000	0.0000	0.7672	0.0001	0.0000	0.0000	0.0000	0.0000	0.0000
3	1.1176	0.9074	1.1064	0.0002	0.0185	0.1370	0.0270	0.0114	0.0010	0.0000	0.0000	0.0000
4	0.3692	0.0238	0.3678	0.0075	1.1542	0.0074	0.0426	0.0199	0.0318	0.0127	0.0002	0.1577
5	0.9986	0.0147	1.0750	0.0871	0.0612	0.0030	0.4923	0.0335	0.5170	0.8114	0.0111	0.1573
6	0.9986	0.0147	1.0750	0.0871	0.0612	0.0030	0.4923	0.0335	0.5170	0.8114	0.0111	0.1573
7	1.1959	0.0034	0.2606	0.5405	0.0012	0.0011	0.1042	0.1200	0.0532	0.2473	0.5237	0.0278
8	1.1959	0.0034	0.2606	0.5405	0.0012	0.0011	0.1042	0.1200	0.0532	0.2473	0.5237	0.0278
9	0.4752	0.0004	0.1813	0.2760	0.0001	0.0002	0.0402	0.2877	0.0300	0.0634	1.0350	0.0050
10	0.5501	0.0023	0.1835	0.7363	0.0151	0.0013	0.4535	0.4314	0.5735	0.8503	0.1733	0.1651
11	0.0003	0.0000	0.0008	0.0522	0.2722	0.0000	0.0014	0.0001	0.0005	0.0008	0.0003	1.2208
12	0.0000	0.0000	0.0000	0.0000	0.0000	0.0000	0.0000	0.0000	0.2415	0.7585	0.0000	0.0000

(A.11)

A.8 Model constants and parameters

Table A.4: Model constants

Symbol	Value	Description
H	0.6	Inertia constant of generator and diesel engine
ω_{mN}	600	Nominal speed 600 [rpm]
pp	$3000/\omega_{mN}$	Number of pole pairs
c	0.15	DC-link capacitor [F]
l_{boost}	$\sqrt{l_d''^2 + l_q''^2} = 0.23$	Boost inductance given from generator armature windings [pu]

Table A.5: Synchronous generator fundamental parameters

Symbol	Value	Description
x_f	2.5364	Field winding reactance [pu]
x_D	2.7336	d-axis damper winding reactance [pu]
x_Q	1.5214	q-axis damper winding reactance [pu]
r_f	0.0033	Field winding resistance [pu]
r_D	0.0433	d-axis damper winding resistance [pu]
r_Q	0.0789	q-axis damper winding resistance [pu]
x_{ad}	2.3955	d-axis mutual reactance [pu]
x_{aq}	1.3955	q-axis mutual reactance [pu]

Table A.6: Diode bridge rectifier setup

Symbol	Value	Description
R_{snub}	8	Snubber resistance [Ω]
C_{snub}	$250e - 8$	Snubber capacitance [F]
R_{on}	0.001	On resistance [Ω]
V_{on}	1.7	Forward voltage [V]

Table A.8: VSM filter constants

Symbol	Parameter	Value	Unit
l_f	VSI filter inductance	0.08	pu
r_f	VSI filter resistance	0.003	pu
c_f	VSI filter capacitance	0.074	pu

Table A.7: VSM control system parameters

Symbol	Parameter	Value	Unit
a_{PLL}	PLL tuning variable	3.0	-
$\omega_{f,PLL}$	PLL filter cutoff	500	rad/s
$k_{p,PLL}, k_{i,PLL}$	PLL controller gain	0.084, 0.747	-
$k_{p,c}, k_{i,c}$	Current controller gain	1.273, 7.499	-
$k_{p,v}, k_{i,v}$	Voltage controller gain	0.29, 92	-
k_q	Reactive power droop gain	0.1	-
T_a	Inertia time constant	4	s
k_d	Frequency damping coefficient	80	-
k_ω	Frequency droop gain	20	-
l_s	Virtual stator inductance	0.25	pu
$r_{s,QS}$	Virtual stator resistance QSEM	0.01	pu
$\omega_{f,QS}$	Output voltage filter QSEM	200	rad/s

Table A.9: Simulation settings

Setting	Value
Solver	ode23t
Simulation time step	variable
Electrical simulation type	Discrete
Electrical simulation step time	$7.5e - 5$
MPC sampling time	0.06
MPC horizon length	200

A.9 Expanded Basic Control layer

Including additional PI controllers in the "basic control layer" will set a limit on the control system response time because (as usual when cascading) the outer loop must be slower than the inner loop. Experiments with such an expanded basic control layer was done during the project. A slower MPC configuration which included the complete SISO control system as a basic control layer, like shown in figure A.10, was tested. The idea was that the MPC would reduce the output voltage reference by a small amount if necessary to maintain speed stability. The system was functional but did not deliver on this main objective because the MPC response time was too long. In that sense, the same functionality could be achieved using only the classical SISO control system. The expanded basic control layer configuration was therefore discarded.

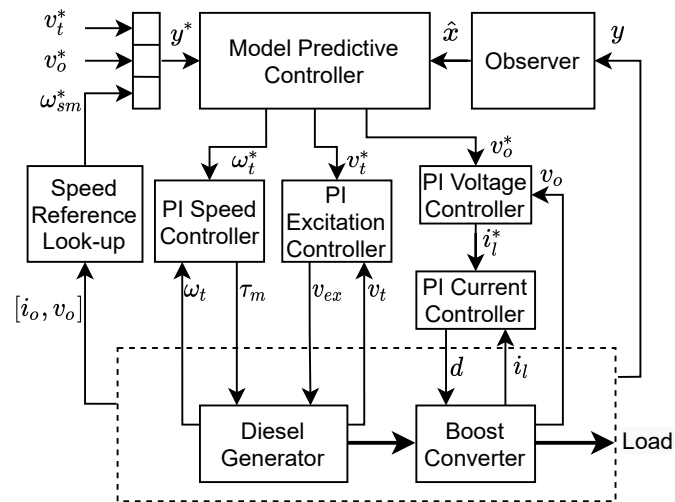


Figure A.10: Control hierarchy with expanded basic control layer. Not used in the project.

Bibliography

- [1] B Bahrani, S Kenzelmann, and A Rufer. “Multivariable-PI-Based dq Current Control of Voltage Source Converters With Superior Axis Decoupling Capability.” eng. In: *IEEE Transactions on Industrial Electronics* 58.7 (2011), pp. 3016–3026.
- [2] D Baimel, R Rabinovici, and S Tapuchi. “Phase shifted PWM with third harmonic injection for over-modulation range operation.” In: *2014 International Symposium on Power Electronics, Electrical Drives, Automation and Motion*. IEEE. 2014, pp. 753–757.
- [3] Chandra Bajracharya et al. “Understanding of tuning techniques of converter controllers for VSC-HVDC.” en. In: Proceedings of the Nordic Workshop on Power and Industrial Electronics (NORPIE/2008). Helsinki University of Technology; Teknillinen korkeakoulu, 2008, p. 8. URL: <http://urn.fi/urn:nbn:fi:tkk-011658>.
- [4] Jens G Balchen. *Reguleringsteknikk*. nob. Trondheim, 2016.
- [5] H. Beck and R. Hesse. “Virtual synchronous machine.” In: *2007 9th International Conference on Electrical Power Quality and Utilisation*. 2007, pp. 1–6.
- [6] Chi-Tsong Chen. *Linear System Theory and Design*. Oxford University Press, Incorporated, 2014.
- [7] Wenjie Chen et al. “Super-capacitors based hybrid converter in marine electric propulsion system.” In: Oct. 2010, pp. 1–6.
- [8] S. Choe, Y. Son, and S. Sul. “Control and Analysis of Engine Governor for Improved Stability of DC Microgrid Against Load Disturbance.” In: *IEEE Journal of Emerging and Selected Topics in Power Electronics* 4.4 (2016), pp. 1247–1258.
- [9] Salvatore D’Arco, Jon Are Wold Suul, and Olav B Fosso. “A Virtual Synchronous Machine implementation for distributed control of power converters in SmartGrids.” eng. In: (2015). URL: <http://hdl.handle.net/11250/2381923>.

- [10] Bjarne Foss and Tor Aksel N Heirung. “Merging optimization and control.” In: *Lecture Notes* (2013).
- [11] J. F. Hansen and F. Wendt. “History and State of the Art in Commercial Electric Ship Propulsion, Integrated Power Systems, and Future Trends.” In: *Proceedings of the IEEE* 103.12 (2015), pp. 2229–2242.
- [12] Edvard Grimsmo Hofstad. “Analysis of small-signal dynamics in a hybrid ship power system with a Virtual Synchronous Machine.” MA thesis. Trondheim, Norway: Department of Engineering Cybernetics NTNU, 2019.
- [13] P Kundur. *Power system stability and control*. eng. New York, 1994.
- [14] J. Lee, S. Lee, and S. Sul. “Variable-Speed Engine Generator With Supercapacitor: Isolated Power Generation System and Fuel Efficiency.” In: *IEEE Transactions on Industry Applications* 45.6 (2009), pp. 2130–2135.
- [15] Jan Machowski et al. *Power System Dynamics: Stability and Control*. eng. New York: John Wiley & Sons, Incorporated, 2008.
- [16] MathWorks. *Choose Sample Time and Horizons*. URL: <https://www.mathworks.com/help/mpc/ug/choosing-sample-time-and-horizons.html> (visited on 05/05/2021).
- [17] MathWorks. *Optimization Problem*. URL: <https://www.mathworks.com/help/mpc/ug/optimization-problem.html> (visited on 04/18/2021).
- [18] MathWorks. *Specifying Constraints*. URL: <https://www.mathworks.com/help/mpc/ug/specifying-constraints.html> (visited on 06/09/2021).
- [19] Olve Mo, Salvatore D’Arco, and Jon Are Suul. “Evaluation of Virtual Synchronous Machines With Dynamic or Quasi-Stationary Machine Models.” eng. In: *IEEE transactions on industrial electronics (1982)* 64.7 (2017), pp. 5952–5962.
- [20] Ned Mohan. *Power electronics : converters, applications, and design*. eng. New York, 1995.
- [21] K. R Padiyar. *Power system dynamics : stability and control*. eng. Singapore, 1996.
- [22] M Ruma and Mohammad Ali Choudhary. “Power Factor Improvement of a Three Phase Rectifier by Boost Regulator.” In: *Journal of Electrical Engineering* 36.2 (2009), pp. 22–27.
- [23] Espen Skjong et al. “The marine vessel’s electrical power system: From its birth to present day.” In: (2015).
- [24] Jon Are Suul. *Overview of Current Control Strategies and Introduction to Control of Power Converters in Islanded Conditions*. University Lecture, Control of Marine Power Conversion Systems. 2020.

- [25] JON ARE WOLD SUUL. "Control of Variable Speed Pumped Storage Hydro Power Plant for Increased Utilization of Wind Energy in an Isolated Grid." MA thesis. Trondheim, Norway: Department of Electrical Power Engineering NTNU, 2006.

